Universität
Potsdam

From changes in the Earth's orbit to African climate variability

WALTER DÜSING

POTSDAM, IM AUGUST 2020

Table of Content

CHAPTER THREE

Cyclicity and variability changes in eastern African paleoclimate during the last ~620 kyrs

CHAPTER FOUR

Recurring types of variability and transitions in the ~620 kyr record of climate change from the Chew Bahir basin, southern Ethiopia

Acknowledgements

Summary

We developed an orbital tuned age model for the composite Chew Bahir sediment core, obtained from the Chew Bahir basin (CHB), southern Ethiopia. To account for the effects of sedimentation rate changes on the spectral expression of the orbital cycles we developed a new method: the Multi-band Wavelet Age modeling technique (MUBAWA). By using a Continuous Wavelet Transformation, we were able to track frequency shifts that resulted from changing sedimentation rates and thus calculated tuned age model encompassing the last 620 kyrs. The results show a good agreement with the directly dated age model that is available from the dating of volcanic ashes.

Then we used the XRF data from CHB and developed a new and robust humid-arid index of east African climate during the last 620 kyrs. To disentangle the relationship of the selected elements we performed a principal component analysis (PCA). In a following step we applied a continuous wavelet transformation on the PC1, using the directly dated age model. The resulting wavelet power spectrum, unlike a normal power spectrum, displays the occurrence of cycles/frequencies in time. The results highlight that the precession cycles are most dominantly expressed under the 400 kyrs eccentricity maximum whereas weakly expressed during eccentricity minimum. This suggests that insolation is a key driver of the climatic variability observed at CHB throughout the last 620 kyrs. In addition, the prevalence of half-precession and obliquity signals was documented. The latter is attributed to the inter-tropical insolation gradient and not interpreted as an imprint of high latitudes forcing on climatic changes in the tropics. In addition, a windowed analysis of variability was used to detect changes in variance over time and showed that strong climate variability occurred especially along the transition from a dominant insolation-controlled humid climate background state towards a predominantly dry and less-insolation controlled climate.

The last chapter dealt with non-linear aspects of climate changes represented by the sediments of the CHB. We use recurrence quantification analysis to detect non-linear changes within the potassium concentration of Chew Bahir sediment cores during the last 620 kyrs. The concentration of potassium in the sediments of the lake is subject to geochemical processes related to the evaporation rate of the lake water at the time of deposition.

Based on recurrence analysis, two types of variabilities could be distinguished. Type 1 represents slow variations within the precession period bandwidth of 20 kyrs and a tendency towards extreme climatic events whereas type 2 represents fast, highly variable climatic transitions between wet and dry climate states. While type 1 variability is linked to eccentricity maxima, type 2 variability occurs during the 400 kyrs eccentricity minimum.

The climate history presented here shows that during high eccentricity a strongly insolation-driven climate system prevailed, whereas during low eccentricity the climate was more strongly affected by short-term variability changes. The short-term environmental changes, reflected in the increased variability might have influenced the evolution, technological advances and expansion of early modern humans who lived in this region. In the Olorgesaille Basin the temporal changes in the occurrence of stone tools, which bracket the transition from Acheulean to Middle Stone Age (MSA) technologies at between 499–320 kyrs, could potentially correlate to the marked transition from a rather stable climate with less variability to a climate with increased variability in the CHB. We conclude that populations of early anatomically modern humans are more likely to have experienced climatic stress during episodes of low eccentricity, associated with dry and high variability climate conditions, which may have led to technological innovation, such as the transition from the Acheulean to the Middle Stone Age.

Zusammenfassung

Bei der von uns entwickelten Multi-band Wavelet Age-Modeling (MUBAWA) Methode handelt es sich um eine Methode zur Erstellung eines orbital abgestimmten Altersmodells.

Diese Methode verwendet, anders als bisherige Methoden, keinen stationären Filter, sondern eine kontinuierliche Wavelet Transformation (CWT) um die orbitale Komponente der zyklischen Sedimentabfolge zu extrahieren. Durch die Anwendung der CWT können zeitliche Änderungen der Sedimentationsrate berücksichtigt werden. Mit Hilfe der neuen MUBAWA Methode haben wir ein orbital abgestimmtes Altersmodell mit einem Basisalter von 620 kyrs für die Sedimentkerne des Chew Bahir Beckens (CHB) erstellt, welches mit den radiometrisch datierten Vulkanaschen der Sedimentkerne übereinstimmt.

In dem folgenden Kapitel haben wir die Ergebnisse der Röntgenfluoreszenz (XRF) - Analyse der Sedimentkerne genutzt um einen neuen Feucht-trocken Anzeiger zu entwickeln Um Umwelteinflüsse, sowie lineare Zusammenhänge der Elementkonzentrationen zu entschlüsseln, haben wir eine Hauptkomponentenanalyse angewendet. Die erste Hauptkomponente (PC1) haben wir als Feucht-Trockenanzeiger interpretiert. Auf Grundlage des direkt datierten Altersmodells haben wir die PC1 genutzt um eine CWT zu berechnen. Das resultierende Wavelet Powerspektrum stellt das Auftreten von Zyklen/Frequenzen in der Zeit dar. Die Ergebnisse zeigen, dass vor 400 kyrs, während eines Exzentrizitätsmaximums, der Präzessionszyklus besonders stark ausgeprägt war, wohingegen der Präzessionszyklus während eines Exzentrizitätsminimums eher schwach ausgeprägt war. Dies deutet darauf hin, dass die Sonneneinstrahlung, welche in den Tropen durch den Präzessionzyklus beeinflusst wird, ein dominanter Faktor für die klimatische Variabilität in CHB während der letzten 620 kyrs darstellt. Darüber hinaus wurde die Prävalenz von Halbpräzessions- und Obliquitätszyklen dokumentiert. Obliquitätszyklen werden dem intertropischen Gradienten der Sonneneinstrahlung zugeschrieben, der klimatische Veränderungen in den Tropen erzwingt und nicht als ein Einfluss der hohen Breiten interpretiert. Darüber hinaus wurde eine gefensterte Variabilitätsanalyse der PC1 verwendet um eine zeitliche Veränderung der Variabilität zu erfassen. Diese zeigte, dass starke Klimavariabilität vor allem entlang des Übergangs von einem dominanten insolationsgesteuerten feuchten Klima zu einem überwiegend trockenen und weniger insolationsgesteuerten Klima auftrat.

Das letzte Kapitel befasst sich mit nichtlinearen Aspekten der Klimavariabilität, repräsentiert durch die Kaliumkonzentration des Sediments des CHBs. Die Kaliumkonzentration in den Sedimenten des Sees ist geochemischen Prozessen unterworfen, die mit der Verdunstungsrate des Seewassers zum Zeitpunkt der Ablagerung zusammenhängen und daher als Feucht-Trockenanzeiger interpretiert werden. Basierend auf der Rekurrenzanalyse konnten zwei Arten von Variabilitäten unterschieden werden. Typ 1 repräsentiert langsame Variationen innerhalb der Bandbreite der Präzessionsperiode von 20 kyrs und eine Tendenz zu extremen klimatischen Ereignissen, während Typ 2 schnelle, sehr variable klimatische Übergänge zwischen feuchten und trockenen Klimazuständen repräsentiert. Die Variabilität vom Typ 1 ist mit Exzentrizitätsmaxima verbunden, wohingegen die Variabilität vom Typ 2 während des Exzentrizitätsminimums vor 400 kyrs auftritt.

Die hier vorgestellte Klimageschichte zeigt, dass bei hoher Exzentrizität ein stark insolationsgetriebenes Klimasystem vorherrschte, während bei niedriger Exzentrizität das Klima stärker von kurzfristigen Variabilitätsänderungen beeinflusst wurde. Die kurzfristigen Umweltveränderungen, die sich in der erhöhten Variabilität widerspiegeln, könnten die Entwicklung, den technologischen Fortschritt und die Expansion der frühneuzeitlichen Menschen, die in dieser Region lebten, beeinflusst haben. Im Olorgesaille-Becken könnten die zeitlichen Veränderungen des Vorkommens von Steinwerkzeugen, die den Übergang von Acheulean zu mittel- steinzeitlichen (MSA) Technologien bei 499-320 kyrs markieren, möglicherweise mit dem deutlichen Übergang von einem eher stabilen Klima mit geringerer Variabilität zu einem Klima mit erhöhter Variabilität in der CHB korrelieren. Wir kommen zu dem Schluss, dass Populationen früher anatomisch moderner Menschen während Episoden geringer Exzentrizität klimatischen Stress erfahren haben könnten. Diese trockenen und hochvariablen Klimabedingungen könnten zu technologischen Innovationen geführt haben, wie z.B. dem Übergang von der Acheulean zur MSA.

Introduction

1 MILANKOVITCH THEORY

Changes in the Earth's climate system on time scales of 104–105 years (orbital time scales) are forced by changes in the eccentricity of the Earth's orbit around the Sun (eccentricity), the inclination of the Earth's axis (obliquity), and the combined effect of the precession of the Earth's axis (axial precession) and the precession of the ellipse of the Earth's orbit (apsidal precession), resulting in the precession of the equinoxes (Milankovitch, 1941, Berger et al., 2006). These so-called Milankovitch cycles are quasi-periodic changes of the earth orbit which are the result of a complex gravitational interaction between the Earth and the Moon as well various other planets within our solar system (Berger, 1978; Berger et al., 1993; Laskar, 2004, Berger et al., 2006). These changes ultimately determine the amount and geographical distribution of solar radiation which is received at the top of the atmosphere (Berger et al., 2006; Nicholson 2017; Goldsmith et al., 2017; Kutzbach et al., 2020). Early achievements in the reconstruction of orbital parameters date back to the 17th century (Lagrange, 1781; Pontécoulant 1834; Agassiz, 1840, Adhémar, 1842; Le Verrier, 1856; Croll, 1890; Pilgrim, 1904; Milankovitch, 1941). Today the increase in computational power and the refinement of the orbital model allows a more precise reconstruction of the geographical distribution of insolation changes on Earth for the past 250 million years (Laskar et al. 1993; Laskar et al., 2004; Bergeret al., 2006).

Eccentricity (e) is the longest of the Milankovitch Cycles with periods of 95, 125, and 413 kyrs (Hays et al., 1976; Berger and Loutre, 1991). It is defined as the ratio of the distance of the Sun from the centre of the ellipse of the Earth's orbit around the Sun and the major axis of the ellipse of the same orbit (Fig.1) (Berger, 1978; Berger et al., 1993; Paillard 2001; Berger et al., 2006). In short, eccentricity describes how elliptical the Earth's orbit is. Within the last one million years, eccentricity reached, on average, a value of e = 0.0281, its highest value of e = 0.0578 at 971 kyrs and its lowest value of e = 0.0042 at 374 kyrs (Laskar, 2004). During that time, the Earth's orbit resembled an almost perfect circle. In contrast, the modern eccentricity value of e = 0.0167 indicates that the Earth's orbit is currently more elliptic (Laskar, 2004).

As a consequence of an elliptical orbit, the Earth reaches a point once a year when it is closest to the Sun (perihelion) and one point when it is furthest from the Sun (aphelion), respectively (Berger, 1978; Berger et al., 1993; Paillard 2001; Berger et al., 2006). During perihelion, more solar radiation reaches the Earth than during aphelion. As aphelion is almost reached during the Northern Hemisphere's summer and the Southern Hemisphere's summer occurs close to perihelion, more energy reaches the Earth's surface during Southern Hemisphere summers than during Northern Hemisphere summers (Paillard 2001, Berger et al., 2006). However, as other orbital parameters, which will be listed below, cause aphelion and perihelion to shift over time it is not necessarily the case for all climate states throughout the geological past. Another effect caused by eccentricity is the change of the length of the seasons. According to Kepler's second law, planets move faster as they get closer to the Sun. Therefore, seasons that occur near perihelion become significantly shorter if e is larger (Paillard et al., 2001).

The 41 kyrs (kyr = kilo years) and 1.2 Myrs (Myr = million years) long obliquity (ε) cycle represents changes in the tilt of the rotational axis of the Earth to the normal of the ellipse of the Earth's orbit around the Sun (Berger, 1978; Berger et al., 1993; Paillard 2001; Berger et al., 2006) (Fig.1). The tilt has fluctuated between ε = 22.1° and ε = 24.5° over the last one million years; with its modern value at ε = 23.4° (Laskar, 2004). An increase in the inclination of the Earth's axis causes the poles to receive more solar energy in summers and stay longer in the polar night during winter (Paillard 2001). An increased inclination of the axis enhances the difference between summer and winter in the Northern and Southern Hemispheres. Obliquity therefore does not change the total solar energy budget that reaches the Earth, but its seasonal distribution and therefore initiates the heat flow away from the equator towards the poles (Berger, 1978; Berger et al., 1993; Paillard 2001; Berger et al., 2006).

Climatic precession is the shortest of the three Milankovitch cycles with the largest climatic effects due to its anti-phase occurrence on both hemispheres (Maslin and Brierley, 2015). It has periods between 19 to 23.5 kyrs, and is measured by the angle ϖ between vernal equinox and perihelion (Fig.1) (Paillard, 2001). Its periods are a result of

the interplay between the axial precession, apsidal precession, and eccentricity. The axial precession represents the precession of the rotational axis of the Earth around the normal of the orbital plane causing a clockwise motion of the solstices and equinoxes (Paillard, 2001). By shifting the rotational axis of the Earth, the strength and distribution of insolation in the Southern and Northern Hemisphere changes anti-phased. Changes in axial precession thus intensify seasonality in one hemisphere while it decreases in the other (Berger, 1988). The apsidal precession describes the precession of the Earth's orbit around the Sun, and has a cycle of 112 kyrs, shifting perihelion and aphelion. The interplay of both cycles results in the precession of the equinoxes, also called climate precession, with a period of 19-23.5 kyrs. Therefore, every 19-23.5 kyrs the Northern Hemisphere is at its maximum tilt (june solstice) towards the Sun during perihelion, while December solstice is at aphelion, and vice versa. Thus, since the climatic precession is related to the simultaneous occurrence of the solstice and the perihelion, the intensity of the climatic precession depends on the eccentricity which determines the insolation differences occurring during perihelion. If eccentricity is at a minimum, and Earth's orbit is almost circular, there is no climatic effect associated with precessional change (Paillard, 2001).
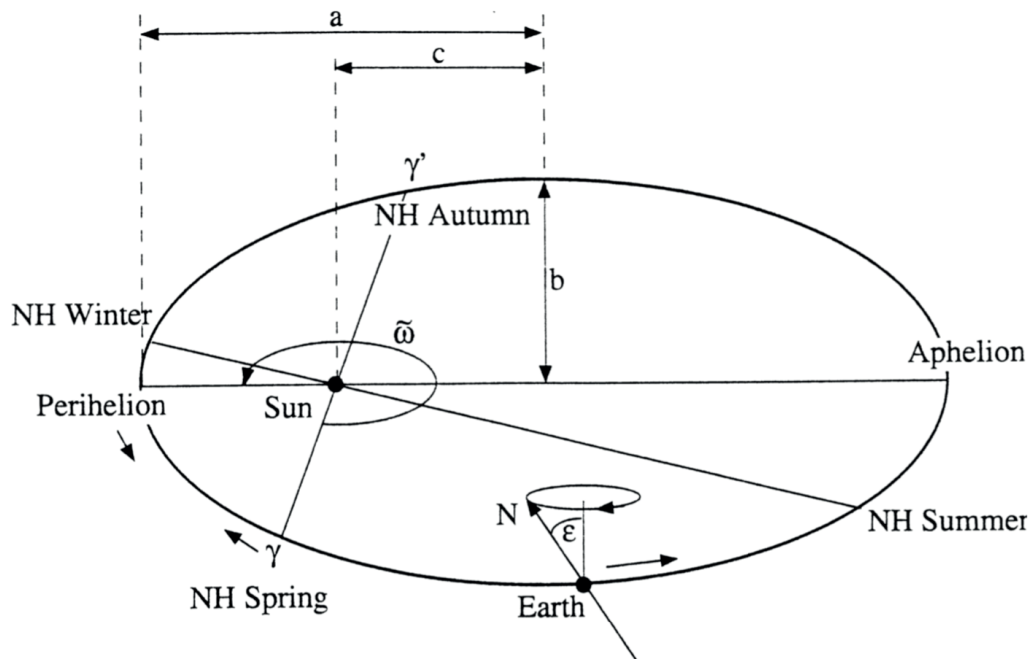
Figure 1
Earth's orbit around the Sun. a is the semi-major axis of the ellipse, b the semi-minor axis and c the distance from focus to centre. ε is the tilt or obliquity. ῶ is the angle between vernal equinox (γ) and perihelion, a measure of precession. Perihelion and aphelion are the points closest and furthest away from the Sun, respectively. NH (Northern Hemisphere) Spring, Summer, Autumn and Winter indicate vernal equinox, summer solstice, autumn equinox and winter solstice. From Paillard (2001).

2 GEOGRAPHICAL, TECTONIC AND GEOLOGICAL SETTING OF THE STUDY AREA

The sediment cores studied herein were recovered from the Chew Bahir basin in the Southern Ethiopian Rift (4.1–6.3°N, 36.5–38.1°E; Fig. 2), a segment of the East African Rift System (Chorowicz, 2005). The East African Rift System is subdivided into three smaller segments; the Main Ethiopian Rift in the northernmost part of the East African Rift System and two branches to the South, the western Rift and Eastern Rift, respectively. The Chew Bahir basin is located in the western part of the Southern Main Ethiopian Rift within the broadly rifted zone (Ebinger et al., 2000; Moore & Davidson, 1978), where the East African Rift System branches into the Eastern and western Rift.

Fig. 2
Study area and drill site location. The Chew Bahir basin (CHB) is marked by a red square. The different seasonal latitudinal positions of the African rain belt (ARB) are marked by white dashed lines. The seasonal position of the Congo Air Boundary (CAB) is marked by a black dashed line (modified after Foerster et al., 2012).
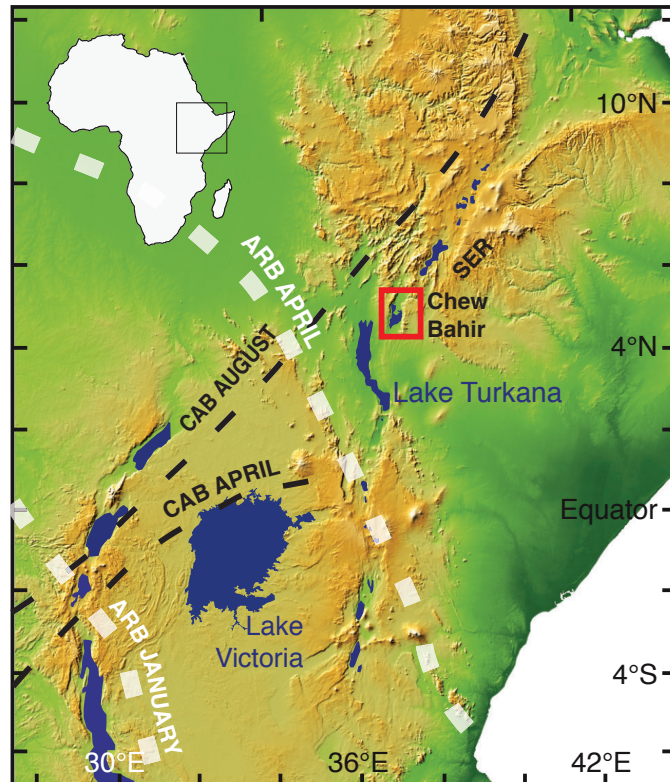
The broadly rifted zone is a 10-50 km-wide, north-south to northeast-southwest trending rift basin with intervening ranges (Davidson, 1983; Ebinger et al., 2000). The complex rift structures developed concurrent with the formation of the East African Rift System during the early Miocene by the eastward migration of the rift along inherited pre-rift structures of the Anza Rift (Boone et al., 2019). Active seismicity and scattered Pliocene-Holocene volcanism to the north of the study area suggests active rifting and a kinematic linkage between the Eastern and Main Ethiopian Rift via the Chew Bahir basin (Ebinger et al., 2000).

Today's dried-out Chew Bahir paleo-lake system is bordered to the west by the Hammar Range representing the Precambrian basement (Davidson, 1983). The metamorphic unit comprises gneisses mainly consisting of feldspar, biotite, muscovite and hornblende bearing rocks, but also a wide range of different high-grade metamorphic rocks containing sillimanite and hornblende (Davidson, 1983). The basin is bound on its Eastern flank by the Teltele-Konso Range, which mainly consists of Miocene basaltic lava flows (Foerster et al., 2012, and reference therein). In the North, the catchment area of the Chew Bahir basin is heart-shaped, with two defined catchments of the perennial Segen and Weyto rivers expanding to the North. Oligocene basalt flows with subordinate rhyolites, trachytes, tuffs and ignimbrites cover the Precambrian basement there (Foerster et al., 2012). The river Weyto flows from the Northwest and the river Segan from the Northeast towards the Chew Bahir basin. Where these two rivers intersect, wetlands have developed which are currently used for intensive agricultural activity.

Two recovered ~290 m long cores of fluvio-lacustrine sediments from the Chew Bahir basin encompass varying environments indicating deep lake phases with clay rich horizons as well as sandy and calcareous layers representing shallow lake phases. The base of the duplicate cores is assumed to be ~620 kyrs old. The drilled sediment cores from Chew Bahir encompasses the time period of the rise of Homo sapiens in Africa and its migration pulses out of Africa (Foerster et al., submitted), thus enabling studies on feedback between climate and human evolution in Eastern Africa, where major events in hominin evolution have occurred (Maslin et al., 2014).

3 EASTERN AFRICAN CLIMATE: PRESENT AND PAST

Rainfall in Eastern Africa, including the Chew Bahir basin, is associated with the seasonal migration of the African Rain Belt (ARB), resulting in two rainy seasons in March-May (long rains) and October-November (short rains), respectively (Nicholson, 2017). The occurrence of the ARB in turn depends on seasonal insolation changes following with a one month delay the zenith of the sun (Nicholson, 2017). When increasing surface temperature leads to enhanced convection over Eastern Africa, moisture bearing air masses from the adjacent Indian Ocean are pulled in via the summer monsoon winds on land, eventually condensing while ascending in the interior of the African continent (Nicholson, 2017). Additionally, on inter annual time scales, an eastward shift of the Congo Air Boundary (CAB), caused by an anomalous low-pressure system over West India, may carry additional moisture from the Atlantic Ocean across the Congo Basin to Southern Ethiopia, where it may cause a third rainy season (Camberlin and Philippon, 2002).

Superimposed on insolation changes, the Eastern African rainfall patterns are also influenced by sea-surface temperature (SST) changes of the Atlantic and Indian Ocean, causing anomalies in the Walker Circulation (WC) (Bjerknes, 1969). These changes are caused by the Indian Ocean Dipole (IOD) and the El Niño-Southern Oscillation (ENSO), which also explain the recent reduction of rainfall intensities in Eastern Africa over the last two decades (Saji et al., 1999; Seleshi and Zanke, 2004; Segele et al., 2009; Nicholson, 2016, 2017). Although ENSO results from SST anomalies in the Pacific Ocean and IOD from those of the Indian Ocean, there is a strong coupling between these climate anomalies (Abram et al., 2020). In this respect ENSO anomalies often trigger IOD anomalies (Allan et al., 2001; Hong et al., 2008; Lau and Nath, 2004). A possible linkage between the ENSO and IOD related WC anomalies may occur via Kelvin and Rossby waves (Pausata et al., 2017). Although ENSO often forces IOD anomalies, IOD events can occur independently of ENSO events (Abram et al., 2020).

However, IOD has a major climate influence on the occurrence of Eastern African rainfall, as shown by the correlation between lake level fluctuations of Lake Naivasha and positive IOD states within the last 70 years (Trauth et al., 2010). In this vein, positive IOD states result in increased rainfall in Eastern Africa, coinciding with enhanced ocean upwelling along the coast of Java and Sumatra. In turn, negative IOD states are associated with upwelling in the Eastern Indian Ocean and droughts in Eastern Africa (Abram et al., 2020). Although numerical modelling of the Western African climate has predicted a more frequent occurrence of positive IOD events (increased rainfall in Eastern Africa) due to the global increase in greenhouse gases (Collins et al., 2019; IPCC, 2019), climate of Eastern Africa has so far been dominated by droughts within the recent decades (Nicholson, 2017). This has been linked to a later onset and earlier cessation of the long rains from March to May (Wainwright et al., 2019).

Another important process that modulates the moisture levels over Southern Ethiopia is the occurrence of the Turkana Jet, a topographically induced low level jet stream (LLJ), which appears to suppress rainfall during the boreal summer (Nicholson 2016). The Turkana Jet occurs within the Turkana Channel, a 700 km long stretch of low elevation, between the Ethiopian and East African Highlands (Nicholson 2016). The jet has a strong influence on the diurnal rainfall in the channel, with less rainfall during increased wind speeds and increased rainfall during reduced wind speeds (Nicholson 2016). One possible explanation for the intensity changes of the Turkana jet is the so-called Bernoullie effect, which is produced by increased low-level-ridging along the coast of the Indian Ocean (Nicholson 2016). This changes the height/pressure ratio within the channel and thus leads to a strengthening of the Turkana Jet (Vizy and Cook, 2019).

On orbital time scales, climate of Eastern Africa is strongly influenced by the Earth's precession cycle, changing the N-S distribution of insolation, allowing the ARB to penetrate farther north during precession minima (e.g., Kutzbach and Street-Perrott, 1985; Tuenter et al., 2003; Clement et al., 2004; Berger et al., 2006; Trauth et al., 2009, 2010; Kutzbach et al., 2020). During a precession minimum, the zenith of the Sun migrates north and south due to the increase of the inclination of the Earth's rotational axes throughout the year. This alone does not change the insolation budget of the tropics, but since the summer solstice during precession minimum coincides with perihelion, the northern tropics receive more solar energy during boreal summer than the austral tropics, causing an intensification of the North African summer monsoon (e.g., Kutzbach et al., 2020). As the occurrence and latitudinal of the ARB is insolation dependent, rainfall regimes also change in pace with precession (e.g., Kutzbach and Street-Perrott, 1985; Berger et al., 2006, Kutzbach et al., 2020). As a consequence, during a precession minimum, when the zenith of the Sun migrates farther north and the Northern Hemisphere receives more solar radiation, large parts of today's semi-arid Sahel and Sahara desert receive considerably more rainfall, resulting in an overal greening of the Sahara region and the appearance of large freshwater lakes (Larasoaña et al., 2003; Trauth et al., 2010; Larasoaña et al., 2013, Grant et al., 2017). Additionally, modelling results indicate that an increase in Mediterranean storm track precipitation during glacials may also have contributed to the greening of the Sahara (Kutzbach et al., 2020).

In regions near the equator that receive rainfall from local sources, precession-controlled climate changes have a different effect. Due to the symmetry of the precession-controlled insolation changes, the annual insolation budget at the equator remains constant, while solar energy received during the autumn and spring equinoxes is anti-phased. The insolation maxima reached during spring and autumn equinoxes are out of phase by half a precession cycle (Berger and Loutre 1997), so that during a precession maximum, the rainy season from March to May is intensified, whereas the rainy season from October to November is weakened (Berger and Loutre 1997; Berger 2006; Trauth 2007). On orbital time scales, this results in a wet period every 9-11 kys in addition to a full precession cycle (19-23 kyrs) (Berger and Loutre 1997). In addition to half precession cycles, a quarter precession cycle is likely to occur if intensification of rainfall strictly follows insolation maxima (Berger, 2006).

Precession-controlled climate cycles have been documented in numerous paleo-climatic archives on the African continent and in marine sediments of its surrounding oceans (e.g. deMenocal, 1995, 2004; Johnson et al., 2016; Grant et al., 2017). In the Mediterranean Sea the analysis of marine drill cores indicated that the cyclical sequence of sapropels, organic rich depositions within the deep-basins of the Mediterranean Sea which are linked to increased Nile discharge, occur in phase with orbital precession (e.g. Grant et al., 2017). In Eastern Africa, paleo lake shore lines of Lake Naivasha that reflect precipitation changes are also paced seemingly by precession (Trauth et al., 2010). Additionally, analysis of dust deposits in the Mediterranean Sea reveal that within the last 8 Myrs, green Sahara periods occurred simultaneously with precession minima (Larasoaña et al., 2013).

An important global climatic transition that affected African climate change is the Early Mid Pleistocene Transition (EMPT). This marks the intensification of glacial-interglacial cycles that initiated after 900 kyrs and resulted in more unstable climate conditions accompanied by a long-term drying trend on the African continent (Maslin and Brierley, 2015). While the global climate before the MPT was characterized by low ice sheet formation and weak glacial cycles forced by changes in orbital obliquity (e.g. Imbrie et al., 1992; Tiedemann et al., 1994; Clark et al., 2006; Elderfield et al., 2012), the glacial interglacial cycles after the MPT intensified and lasted longer (Rohling et al., 2014). The intensified glacial fluctuations had a sawtooth character with slowly rising glacial conditions and abrupt terminations that may have been forced by sea level fluctuation (Maslin and Brierley, 2015).

4 PALEOANTHROPOLOGY AND CLIMATE CHANGE

The Earth's climatic system has changed dramatically during the last ~3 Myrs, including the intensification of northern hemisphere glaciation (~2.75 Myrs BP), the onset of the WC (~1.9 Myrs BP) and the EMPT (~920 kyrs BP), of which all might have had a possible effect on the evolution and dispersal of species living during that time

(deMenocal, 2004; Trauth et al., 2010; Maslin et al., 2014). At the same time, the species diversity of hominins has been greatly reduced and *H. sapiens* has remained the last surviving human species on Earth (e.g. Stringer, 2016).

Over the course of the last few decades, archaeological finds as well as genetic studies have indicated that the origin of our direct ancestor *H. sapiens* is most likely located in Africa (e.g. Vigilant et al., 1991; Hublin, et al. 2017; Scerri et al., 2018). While the previously oldest fossil finds in Eastern Africa of anatomically modern humans (AMH) were dated 200 kyrs BP (Omo I and Omo II, McDougall et al., 2005) and 160 kyrs BP (White et al., 2004), pointed to an origin of *H. sapiens* in Eastern Africa, the newly dated archaic *H. sapiens* (315 kyrs BP) found in Jebbel Irhoud, Morocco, North Africa, questions the origin of *H. sapiens* in a single region (Hublin et al., 2017; Scerri et al., 2018). In this context sub-divisions of early humans were shaped and sustained by temporary geographical and climatic barriers within fractured habitable zones across whole Africa (Trauth et al., 2010; Timmermann and Friedrich, 2017; Hublin, et al. 2017; Scerri et al., 2018).

Additionally, the influence of environmental change on human behaviour can be observed by technological or cultural transitions, documented by stone tool usage (Potts et al., 2018). In the Olorgesaillie Basin in Eastern Africa, the transition from Acheulean (before 499 kyrs BP) stone tools to MSA (after 320 kyrs BP) tools are particularly well documented (Deino et al., 2018). The transition is accompanied by dramatic climatic changes from a wet climate to a drier and more variable climate (Potts et al., 2018). The stone tools before the transition, which belong to the Acheulean technology, are much heavier and made from various different materials, whereas the stone tools after the transition are much smaller and were made from precisely selected materials, some of which were transported over long distances (Potts et al., 2018). This suggests that hominins living during that time in Eastern Africa adapted to a change from wet to dry climate conditions by changing the use of stone tool technology.

A more recent example of climatically induced technological evolution and dispersal is the African Humid Period (AHP), which started roughly 15 kyrs BP ago, representing a pan African wet phase, and led to the colonization of today's Sahara region (e.g. deMenocal, 2004; Kuper and Kröpelin, 2006, Tierney et al., 2017). At the end of the AHP at ~5.3 kyrs BP, when today's Sahara region began to dry out again, the population sizes of *H. sapiens* occupying the region also decreased. Remaining populations are argued to have retreated towards the still fertile areas of the Nile Valley where the first advanced civilization of the Pharaohs developed during the same time (Kuper and Kröpelin, 2006). Thus, the termination of the AHP represents a profound cultural and technological transition (Kuper and Kröpelin, 2006). The AHP also represents a pronounced wet period in Eastern Africa (Foerster et al., 2012). While during the AHP large regions in Eastern Africa were suitable as a settlement area for *H. sapiens*, early human populations retreated to the coasts of Eastern Africa (Joordens et al., 2019) or the highlands of the East African Rift System after the AHP (Tribolo et al., 2017; Brandt et al., 2012; Vogelsang and Wendt, 2018), documenting that climatic changes have influenced the spread and life style of *H. sapiens* living in Eastern Africa during that time.

5 INTRODUCTION TO THE CHAPTERS

This doctoral thesis deals with the effects of orbital-driven insolation fluctuations on the climate in eastern Africa, as documented in a ~290 m long composite core from the Chew Bahir basin, southern Ethiopian rift.

The **chapter two** of this doctoral thesis is about the development of an orbital tuned age model for the composite sediment core. Applying the traditional tuning approach requires several prerequisites such as: i) that insolation is the most dominant driver of climate change at Chew Bahir and is thus reflected by repetitive sedimentary facies within the recovered sedimentary sequence, and ii) a continuous and relatively constant sedimentation rate without hiatuses. Assuming that these prerequisites are fulfilled, the orbital frequencies of precession, obliquity and eccentricity can be isolated due to bandpass filtering. The filtered time series is then synchronised with the known course of the corresponding orbital cycle for the same time interval to create an age-depth transfer function. However, a lacustrine system such as CHB, is usually characterised by highly variable sedimentation rates. To account for the effects of sedimentation rate changes on the spectral expression of the orbital cycles, we developed a new method: the Multi-band Wavelet Age modeling technique (MUBAWA). By using a continuous wavelet transformation, we were able to track frequency

shifts that resulted from changing sedimentation rates and thus calculated a more accurate tuned age model encompassing the last 620 kyrs. The results show a good agreement with the directly dated age model that is available from the dating of volcanic ashes.

This work was written in cooperation with several co-authors. Part of the team were Walter Duesing, Nadine Berner, Hauke Kraemer, Norbert Marwan and Martin H. Trauth. Walter Duesing is the lead author of the publication and was involved in all crucial steps from initiation of the first ideas, implementation of the statistical analysis, and the writing process. Hauke Kraemer and Nadine Berner were mainly involved in supporting the development of the methods section. Martin H. Trauth, as well as Norbert Marwan have accompanied the entire process and supported the development of the work on numerous issues ranging from code implementation to the interpretation of climate processes.

In **chapter three** the XRF data from CHB were analysed to develop a new and robust humid-arid index of east African climate during the last 620 kyrs. For this purpose, we selected XRF elements, whose geochemical relationships can be clearly linked to changes in climatic background conditions at Chew Bahir. To disentangle the relationship of the selected elements we performed a principal component analysis. In the next step, we applied continuous wavelet transformation on the PC1 which explains the most variance of the used XRF data set. The resulting wavelet power spectrum, unlike a normal power spectrum, displays the occurrence of cycles/frequencies in time. The results highlight that the precession cycles are most dominantly expressed under the 400 kyrs eccentricity maximum whereas weakly expressed during eccentricity minimum. This suggests that insolation is a key driver of the climatic variability observed at Chew Bahir throughout the last 620 kyrs. In addition, the prevalence of half-precession and obliquity signals was documented. The latter is attributed to the inter-tropical insolation gradient and not interpreted as an imprint of high latitudes forcing on climatic changes in the tropics. In addition, a windowed analysis of variability was used to detect changes in variance over time and showed that strong climate variability occurred especially along the transition from a dominant insolation-controlled humid climate background state towards a predominantly dry and less-insolation controlled climate.

This chapter is the result of a cooperation with several authors, Walter Duesing, Stefanie Kaboth-Bahr, Martin H. Trauth, Asfawossen Asrat, Andrew S. Cohen, Verena Foerster, Henry F. Lamb, Finn Viehberg. Walter Duesing is the lead author of this chapter and was responsible for the statistical analysis and its interpretations. Stefanie Kaboth-Bahr helped in the interpretation of the statistical analysis in relation to marine paleo-climate data. All other authors were involved in the development of the manuscript and contributed to the improvement of this chapter within several internal review cycles.

The **fourth chapter** focuses on non-linear aspects of climate changes represented by the sediments of the Chew Bahir Basin. We use recurrence quantification analysis to detect non-linear changes within the potassium concentration of Chew Bahir sediment cores during the last 620 kyrs. The concentration of potassium in the sediments of the lake is subject to geochemical processes related to the evaporation rate of the lake water at the time of deposition (Foerster et al., 2018). Based on recurrence analysis, two types of variabilities could be distinguished. Type 1 represents slow variations within the precession period bandwidth of 20 kyrs and a tendency towards extreme climatic events whereas Type 2 represents fast, highly variable climatic transitions between wet and dry climate states. While type 1 variability is linked to eccentricity maxima, type2 variability occurs during the 400 kyrs eccentricity minimum.

This chapter is the result of a cooperative effort by several authors including Martin H. Trauth, Asfawossen Asrat, Andrew S. Cohen, Walter Duesing, Verena Foerster, Stefanie Kaboth-Bahr, Hauke Kraemer, Henry F. Lamb, Norbert Marwan, Mark A. Maslin, Frank Schaebitz. Martin Trauth, Norbert Marwan, as well as Hauke Kraemer worked in close cooperation on the development and improvement of statistical analysis. Walter Duesing was involved from the beginning of the project and provided various age models and revised the manuscript. All other authors were involved in improving the manuscript within several internal reviews, contributing significantly to the improvement of the chapter.

REFERENCES

Abram, N. J., Hargreaves, J. A., Wright, N. M., Thirumalai, K., Ummenhofer, C. C., & England, M. H. (2020). Palaeoclimate perspectives on the Indian Ocean Dipole. Quaternary Science Reviews, 237, 106302.

Adhémar, J. (1842). Révolutions de la mer, (Paris: Bachelier)

Agassiz, L. (1840). Études sur les glaciers (Paris)

Allan, R., Chambers, D., Drosdowsky, W., Hendon, H.H., Latif, M., Nicholls, N., Smith, I., Stone, R., Tourre, Y., (2001). Is there an Indian Ocean Dipole, and is it independent of the El Nin~o - Southern Oscillation. CLIVAR Exchanges 6, 18e22.

Berger, A. L. (1978). Long-Term Variations of Caloric Insolation Resulting from the Earth's Orbital Elements 1. Quaternary research, 9(2), 139-167.

Berger, A., & Loutre, M. F. (1991). Insolation values for the climate of the last 10 million years. Quaternary Science Reviews, 10(4), 297-317.

Berger, A., Loutre, M. F., & Tricot, C. (1993). Insolation and Earth's orbital periods. Journal of Geophysical Research: Atmospheres, 98(D6), 10341-10362.

Berger, A., & Loutre, M. F. (1997). Intertropical latitudes and precessional and half-precessional cycles. Science, 278(5342), 1476-1478.

Berger, A., Loutre, M. F., & Mélice, J. L. (2006). Equatorial insolation: from precession harmonics to eccentricity frequencies.

Bjerknes, J. (1969). Atmospheric teleconnections from the equatorial Pacific. Mon. Wea. Rev, 97(3), 163-172.

Boone, S. C., Balestrieri, M. L., Kohn, B. P., Corti, G., Gleadow, A. J. W., & Seiler, C. (2019). Tectonothermal evolution of the Broadly Rifted Zone, Ethiopian Rift. Tectonics, 38(3), 1070-1100.

Brandt, S.A., Fisher, E.C., Hildebrand, E.A., Vogelsang, R., Ambrose, S.H., Lesur, J., Wang, H. (2012). Early MIS 3 occupation of Mochena Borago Rockshelter, Southwest Ethiopian Highlands: implications for Late Pleistocene archaeology, paleoenvironments and modern human dispersal. Quaternary International 274, 38e54.

Camberlin, P., & Philippon, N. (2002). The East African March–May rainy season: Associated atmospheric dynamics and predictability over the 1968–97 period. Journal of Climate, 15(9), 1002-1019.

Castañeda, I. S., Mulitza, S., Schefuß, E., dos Santos, R. A. L., Damsté, J. S. S., & Schouten, S. (2009). Wet phases in the Sahara/Sahel region and human migration patterns in North Africa. Proceedings of the National Academy of Sciences, 106(48), 20159-20163.
Chorowicz, J. (2005). The east African rift system. Journal of African Earth Sciences, 43(1-3), 379-410.

Clark, P. U., Archer, D., Pollard, D., Blum, J. D., Rial, J. A., Brovkin, V., ... & Roy, M. (2006). The middle Pleistocene transition: characteristics, mechanisms, and implications for long-term changes in atmospheric pCO_2. Quaternary Science Reviews, 25(23-24), 3150-3184.

Clement, A. C., Hall, A., & Broccoli, A. J. (2004). The importance of precessional signals in the tropical climate. Climate Dynamics, 22(4), 327-341.

Collins, M., Sutherland, M., Bouwer, L., Cheong, S.-M., Frolicher, T., Combes, H.J.D., Roxy, M.K., Losada, I., McInnes, K., Ratter, B., Rivera-Arriaga, E., Susanto, R.D., Swingedouw, D., Tibig, L. (2019). Extremes, abrupt changes and managing risk. In: Portner, H.-O., Roberts, D.C., Masson-Delmotte, V., Zhai, P., Tignor, M., Poloczanska, E., Mintenbeck, K., Alegría, A., Nicolai, M., Okem, A., Petzold, J., Rama, B., Weyer, N.M. (Eds.), IPCC Special Report on the Ocean and Cryosphere in a Changing Climate.

Croll, J. (1890). Climate and Time (London)

Davidson, A., (1983). The Omo River project: reconnaissance geology and geochem- istry of parts of Ilubabor, Kefa, Gemu Gofa and Sidamo. Ethiopian Institute of Geological Surveys Bulletin 2, 1e89.

Demenocal, P. B. (1995). Plio-pleistocene African climate. Science, 270(5233), 53-59.

Peter, B. D. (2004). African climate change and faunal evolution during the Pliocene–Pleistocene. Earth and Planetary Science Letters, 220(1-2), 3-24.

Ebinger, C. J., Yemane, T., Harding, D. J., Tesfaye, S., Kelley, S., & Rex, D. C. (2000). Rift deflection, migration, and propagation: Linkage of the Ethiopian and Eastern rifts, Africa. Geological Society of America Bulletin, 112(2), 163-176.

Foerster, V., Junginger, A., Langkamp, O., Gebru, T., Asrat, A., Umer, M., ... & Trauth, M. H. (2012). Climatic change recorded in the sediments of the Chew Bahir basin, southern Ethiopia, during the last 45,000 years. Quaternary International, 274, 25-37.

Goldsmith, Y., Broecker, W. S., Xu, H., Polissar, P. J., Demenocal, P. B., Porat, N., ... & An, Z. (2017). Northward extent of East Asian monsoon covaries with intensity on orbital and millennial timescales. Proceedings of the National Academy of Sciences, 114(8), 1817-1821.

Grant, K. M., Rohling, E. J., Westerhold, T., Zabel, M., Heslop, D., Konijnendijk, T., & Lourens, L. (2017). A 3 million year index for North African humidity/aridity and the implication of potential pan-African Humid periods. Quaternary Science Reviews, 171, 100-118.

Hays, J.D., Imbrie, J., Shackleton, N.J., 1976. Variations in the Earth's orbit: pacemaker of the Ice Ages. Science 194, 1121e1132.

Hershkovitz, I., Weber, G. W., Quam, R., Duval, M., Grün, R., Kinsley, L., ... & Arsuaga, J. L. (2018). The earliest modern humans outside Africa. Science, 359(6374), 456-459.

Hong, C. C., Lu, M. M., & Kanamitsu, M. (2008). Temporal and spatial characteristics of positive and negative Indian Ocean dipole with and without ENSO. Journal of Geophysical Research: Atmospheres, 113(D8).

Hublin, J. J., Ben-Ncer, A., Bailey, S. E., Freidline, S. E., Neubauer, S., Skinner, M. M., ... & Gunz, P. (2017). New fossils from Jebel Irhoud, Morocco and the pan-African origin of Homo sapiens. Nature, 546(7657), 289-292.

Imbrie, J., Boyle, E. A., Clemens, S. C., Duffy, A., Howard, W. R., Kukla, G., ... & Molfino, B. (1992). On the structure and origin of major glaciation cycles 1. Linear responses to Milankovitch forcing. Paleoceanography, 7(6), 701-738.

IPCC, (2019). Summary for Policymakers. In: Pörtner, H.-O., Roberts, D.C., Masson- Delmotte, V., Zhai, P., Tignor, M., Poloczanska, E., Mintenbeck, K., Alegría, A., Nicolai, M., Okem, A., Petzold, J., Rama, B., Weyer, N.M. (Eds.), IPCC Special Report on the Ocean and Cryosphere in a Changing Climate. World Meteorological Organization.

Johnson, T. C., Werne, J. P., Brown, E. T., Abbott, A., Berke, M., Steinman, B. A., ... & Scholz, C. A. (2016). A progressively wetter climate in southern East Africa over the past 1.3 million years. Nature, 537(7619), 220-224.

Joordens, J. C., Feibel, C. S., Vonhof, H. B., Schulp, A. S., & Kroon, D. (2019). Relevance of the eastern African coastal forest for early hominin biogeography. Journal of human evolution, 131, 176-202.

Kuper, R., & Kröpelin, S. (2006). Climate-controlled Holocene occupation in the Sahara: motor of Africa's evolution. Science, 313(5788), 803-807.

Kutzbach, J. E., & Street-Perrott, F. A. (1985). Milankovitch forcing of fluctuations in the level of tropical lakes from 18 to 0 kyr BP. Nature, 317(6033), 130-134.

Kutzbach, J. E., Guan, J., He, F., Cohen, A. S., Orland, I. J., & Chen, G. (2020). African climate response to orbital and glacial forcing in 140,000-y simulation with implications for early modern human environments. Proceedings of the National Academy of Sciences, 117(5), 2255-2264.

Lagrange, J. L. (1781). Oeuvres complètes, t. V, Gauthier-Villars, Paris, 1870, 125

Lamarck, J.B. (1809). Philosophie zoologique, ou exposition des considérations relatives à l'histoire naturelle des animaux. Translated by H. Elliot, 1984, Chicago University Press.

Larrasoaña, J.C., Roberts, A.P., Rohling, E.J., Winklhofer, M., Wehausen, R. (2003). Three million years of monsoon variability over the northern Sahara. Climate Dynamics 21, 689–698, doi:10.1007/s00382-003-0355-z.

Larrasoaña, J. C., Roberts, A. P., & Rohling, E. J. (2013). Dynamics of green Sahara periods and their role in hominin evolution. PloS one, 8(10).
Laskar, J., Joutel, F., & Boudin, F. (1993). Orbital, precessional, and insolation quantities for the Earth from-20 Myr to+ 10 Myr. Astronomy and Astrophysics, 270, 522-533.

Laskar, J., Gastineau, M., Joutel, F., Robutel, P., Levrard, B., Correia, A. (2004). A long term numerical solution for the insolation quantities of Earth. Astronomy and Astrophysics, 428, 261-285, available online at http://vo.imcce.fr/insola/earth/online/earth/online/.

LAU, N. C., NATH, M. J., & WANG, H. (2004). Simulations by a GFDL GCM of ENSO-related variability of the coupled atmosphere-ocean system in the East Asian monsoon region. In East Asian Monsoon (pp. 271-300).

Le Verrier, U. (1856), Ann. Obs. Paris, II, Mallet-Bachelet, Paris

Maslin, M. A., Brierley, C. M., Milner, A. M., Shultz, S., Trauth, M. H., & Wilson, K. E. (2014). East African climate pulses and early human evolution. Quaternary Science Reviews, 101, 1-17.

Maslin, M. A., & Brierley, C. M. (2015). The role of orbital forcing in the Early Middle Pleistocene Transition. Quaternary International, 389, 47-55.

McDougall, I., Brown, F.H., Fleagle, J.G. (2005) Stratigraphic placement and age of modern humans from Kibish, Ethiopia. Nature, 433, 733–736.

Milankovitch, M. (1941). Kanon der Erdbestrahlung und seine Anwendung auf das Eiszeitenproblem, Royal Serbian Academy
Moore Jr, J. M., & Davidson, A. (1978). Rift structure in southern Ethiopia. Tectonophysics, 46(1-2), 159-173.

Nicholson, S. E. (2016). An analysis of recent rainfall conditions in Eastern Africa. International Journal of Climatology, 36(1), 526-532.

Nicholson, S. E. (2017). Climate and climatic variability of rainfall over Eastern Africa. Reviews of Geophysics, 55(3), 590-635.

Owen, R.B., et al., (2018). Progressive aridification in East Africa over the last half million years and implications for human evolution, PNAS, doi:10.1073/pnas.1801357115, 1–6.

Paillard, D. (2001). Glacial cycles: toward a new paradigm. Reviews of Geophysics, 39(3), 325-346

Pausata, F. S., Zhang, Q., Muschitiello, F., Lu, Z., Chafik, L., Niedermeyer, E. M., ... & Liu, Z. (2017). Greening of the Sahara suppressed ENSO activity during the mid-Holocene. Nature communications, 8(1), 1-12.

Pilgrim, L. (1904). Versuch einer rechnerischen Behandlung des Eiszeitenproblems. Jahreshefte für vaterländische Naturkunde in Württemberg, 60.

Pontécoulant, G. (1834). Théorie Analytique du Système du Monde, t. III, Bachelier, Paris

Potts, R., Behrensmeyer, A. K., Faith, J. T., Tryon, C. A., Brooks, A. S., Yellen, J. E., ... & Levin, N. E. (2018). Environmental dynamics during the onset of the Middle Stone Age in Eastern Africa. Science, 360(6384), 86-90.

Rohling, E. J., Cane, T. R., Cooke, S., Sprovieri, M., Bouloubassi, I., Emeis, K. C., ... & Kemp, A. E. S. (2002). African monsoon variability during the previous interglacial maximum. Earth and Planetary Science Letters, 202(1), 61-75.

Saji, N. H., Goswami, B. N., Vinayachandran, P. N., & Yamagata, T. (1999). A dipole mode in the tropical India Ocean. Nature, 401(6751), 360-363.

Scerri, E. M., Thomas, M. G., Manica, A., Gunz, P., Stock, J. T., Stringer, C., ... & d'Errico, F. (2018). Did our species evolve in subdivided populations across Africa, and why does it matter?. Trends in ecology & evolution, 33(8), 582-594.

Segele, Z. T., Lamb, P. J., & Leslie, L. M. (2009). Large-scale atmospheric circulation and global sea surface temperature associations with Horn of Africa June–September rainfall. International Journal of Climatology: A Journal of the Royal Meteorological Society, 29(8), 1075-1100.

Seleshi, Y., & Zanke, U. (2004). Recent changes in rainfall and rainy days in Ethiopia. International Journal of Climatology: A Journal of the Royal Meteorological Society, 24(8), 973-983.

Stringer, C. (2016). The origin and evolution of Homo sapiens. Philosophical Transactions of the Royal Society B: Biological Sciences, 371(1698), 20150237.

Tiedemann, R., Sarnthein, M., & Shackleton, N. J. (1994). Astronomic timescale for the Pliocene Atlantic δ18O and dust flux records of Ocean Drilling Program Site 659. Paleoceanography, 9(4), 619-638.

Tierney, J. E., Pausata, F. S., & deMenocal, P. B. (2017). Rainfall regimes of the Green Sahara. Science advances, 3(1), e1601503.

Timmermann, A., & Friedrich, T. (2016). Late Pleistocene climate drivers of early human migration. Nature, 538(7623), 92-95.

Trauth, M. H., Maslin, M. A., Deino, A. L., Strecker, M. R., Bergner, A. G., & Dühnforth, M. (2007). High-and low-latitude forcing of Plio-Pleistocene East African climate and human evolution. Journal of Human Evolution, 53(5), 475-486.

Trauth, M. H., Larrasoana, J. C., & Mudelsee, M. (2009). Trends, rhythms and events in Plio-Pleistocene African climate. Quaternary Science Reviews, 28(5-6), 399-411.

Trauth, M. H., Maslin, M. A., Deino, A. L., Junginger, A., Lesoloyia, M., Odada, E. O., ... & Tiedemann, R. (2010). Human evolution in a variable environment: the amplifier lakes of Eastern Africa. Quaternary Science Reviews, 29(23-24), 2981-2988.

Tribolo, C., Asrat, A., Bahain, J. J., Chapon, C., Douville, E., Fragnol, C., ... & Pleurdeau, D. (2017). Across the gap: Geochronological and sedimentological analyses from the Late Pleistocene-Holocene sequence of Goda Buticha, southeastern Ethiopia. PloS one, 12(1), e0169418.

Tuenter, E., Weber, S. L., Hilgen, F. J., & Lourens, L. J. (2003). The response of the African summer monsoon to remote and local forcing due to precession and obliquity. Global and Planetary Change, 36(4), 219-235.

Vigilant, L., Stoneking, M., Harpending, H., Hawkes, K., & Wilson, A. C. (1991). African populations and the evolution of human mitochondrial DNA. Science, 253(5027), 1503-1507.

Vizy, E. K., & Cook, K. H. (2019). Observed relationship between the Turkana low-level jet and boreal summer convection. Climate Dynamics, 53(7-8), 4037-4058.

Vogelsang, R., & Wendt, K. P. (2018). Reconstructing prehistoric settlement models and land use patterns on Mt. Damota/SW Ethiopia. Quaternary International, 485, 140-149.

Wainwright, C. M., Marsham, J. H., Keane, R. J., Rowell, D. P., Finney, D. L., Black, E., & Allan, R. P. (2019). 'Eastern African Paradox'rainfall decline due to shorter not less intense Long Rains. npj Climate and Atmospheric Science, 2(1), 1-9.

White et al. (2003) Pleistocene Homo sapiens from Middle Awash, Ethiopia. Nature, 423, 742–747.

Multiband wavelet age modeling (MUBAWA) for a ~293 m (~600 kyr) sediment core from Chew Bahir basin, southern Ethiopian Rift

Walter Duesing[1], Nadine Berner[2], Alan L. Deino[3], Verena Foerster[4], K. Hauke Kraemer[1,5], Norbert Marwan[5], Martin H. Trauth[*1]

[1] University of Potsdam, Institute of Geoscience, Potsdam, Germany

[2] Safety Analyses Department, Gesellschaft für Anlagen- und Reaktorsicherheit (GRS) GmbH, Forschungszentrum Garching, Germany

[3] Berkeley Geochronology Center, Berkeley, USA

[4] University of Cologne, Institute of Geography Education, Cologne, Germany

[5] Potsdam Institute for Climate Impact Research, Potsdam, Germany

[*]Corresponding Author: email wduesing@uni-potsdam.de

ABSTRACT

The use of cyclostratigraphy to reconstruct the timing of deposition of lacustrine deposits requires sophisticated tuning techniques that can accommodate continuous long-term changes in sedimentation rates. However, most tuning methods use stationary filters that are unable to take into account such long-term variations in accumulation rates. To overcome this problem we present herein a new multiband wavelet age modeling (MUBAWA) technique that is particularly suitable for such situations and demonstrate its use on a 293 m composite core from the Chew Bahir basin, southern Ethiopian rift. In contrast to traditional tuning methods, which use a single, defined bandpass filter, the new method uses an adaptive bandpass filter that adapts to changes in continuous spatial frequency evolution paths in a wavelet power spectrum, within which the wavelength varies considerably along the length of the core due to continuous changes in long-term sedimentation rates. We first applied the MUBAWA technique to a synthetic data set before then using it to establish an age model for the approximately 293 m long composite core from the Chew Bahir basin. For this we used the 2nd principal component of color reflectance values from the sediment, which showed distinct cycles with wavelengths of 10–15 m and of ~40 m that were probably a result of the influence of orbital cycles. We used six independent $^{40}Ar/^{39}Ar$ ages from volcanic ash layers within the core to determine an approximate spatial frequency range for the orbital signal. Our results demonstrate that the new wavelet-based age modeling technique can significantly increase the accuracy of tuned age models.

1 INTRODUCTION

When investigating paleoclimate records derived from lake cores, the reliability of the age model used is crucial. This reliability depends largely on the density of independent age-control points, which should ideally be evenly distributed along the entire length of the core. Such age-control points are derived from radiometric age determinations obtained by, for example, $^{40}Ar/^{39}Ar$ dating of volcanic ash layers, ^{14}C dating of organic material, or luminescence

dating of feldspar and quartz crystals. Datable material is, however, often scarce in sediment cores. Cyclostratigraphy can be used in such cases to add additional age control points, evenly distributed in time. This method has been applied since the mid-1970s to marine records that extend beyond the range of the radiocarbon dating technique (e.g., Hays et al., 1976; Pisias et al., 1984; Martinson et al., 1987; Tiedemann et al., 1994; Imbrie et al., 1984; Grant et al., 2017). Orbital tuning has often been used to increase the temporal resolution between radiometric age control points, more commonly in paleoceanography than in paleolimnology (e.g., Grant et al., 2017).

Traditional tuning techniques first assume a maximum age for the base of the core (the base age), which is typically derived from existing radiometric dating and/or magnetostratigraphy, to derive a preliminary linear age model assuming constant sedimentation rates. (e.g., Hays et al., 1976; Pisias et al., 1984; Martinson et al., 1987; Tiedemann et al., 1994). The next step involves using a bandpass filter to reduce the proxy data to a single orbital frequency, which should match that of the tuning target (TT). The TT is a reference time series used during tuning, whose exact time course is known and whose frequency is also expressed in the proxy data. The final step is then to align the peaks of the filtered time series with those of the TT (fine tuning the preliminary age model) and to interpolate all core data to the new tuned age model.

Variants of this technique use frequency shifts by applying a moving-window Fourier technique Meyers et al. 2001), a method that tracks the dominant harmonic in the data series (Park and Herbert, 1987), an average spectral misfit method (Meyer and Sageman et al., 2007), or a spectral moment approach (Sinnesael et al., 2018), to establish an age model (Hinnov, 2013, and references therein). Some published applications of the method have been criticized for over tuning (e.g. Tiedemann et al., 1994; Raymo et al. 1997) which is why Muller and MacDonald (2000) proposed the use of *minimal tuning*, for which only a few age control points are required (for example ages obtained from magnetic field reversals or radiometric ages) obtained from within the core. One of the main assumptions of the minimal tuning methods is a relatively constant sedimentation rate, which allows a stationary bandpass filter to be used. This tuning method, which is increasingly popular in paleolimnology (e.g., Wagner et al., 2019), consequently needs to be adapted in order to be applicable to lake environments, where the sedimentation rate is unlikely to be constant.

In this paper we present a new tuning technique that is suitable for use with paleoclimate records that have few radiometric age determinations but show significant orbital cyclicity. The fundamental difference between this new technique and other tuning techniques is that instead of a fixed bandpass filter we use a new adaptive filtering method that takes into account continuous long-term changes in sedimentation rates. The multiband wavelet age modeling (MUBAWA) approach uses a continuous wavelet spectral analysis to identify and trace the orbital signal within a user-defined range of possible base ages for the core.

We first used a synthetic example to demonstrate the advantages of the new method compared to a traditional method of cyclostratigraphy similar to the minimal tuning approach of Muller and MacDonald (2000). We then applied the technique to a 292.87 m composite core collected from the Chew Bahir basin in southern Ethiopia. The results demonstrate how this method can be used to further improve orbital tuning as an age-modeling technique and facilitate its use in a broad range of applications.

2 METHODS
2.1 THE PRINCIPLE OF THE MUBAWA APPROACH

The MUBAWA approach is based on the application of a continuous wavelet transformation (CWT) to a depth series, with the aim of generating a tuned age model. We use the CWT to track variations in the spatial frequency of the astronomical component with depth (which we refer to as the spatial frequency path), in order to be able to adaptively bandpass filter the astronomical component from the proxy data. The MUBAWA technique is specifically designed for lacustrine depositional environments such as that of the Chew Bahir basin, with their continuous, long-term changes in sedimentation rates, whereas methods using stationary filters are not suitable for such complex depositional environments.

The MUBAWA algorithm consists of several modular functions, which are provided as MATLAB scripts in the Appendix. The algorithm is divided into the following four steps (Fig.1). Step 1: preprocessing, which involves resampling and evenly spacing the input data defined by the frequency of the TT and the maximum possible base age (t_{max}). Step 2: spatial frequency range approximation (SFRA), which is an optional step that uses the available age control to approximate the spatial frequency range of the targeted orbital component, Step 3: spatial frequency path mapping, which involves determining spatial frequencies using a CWT and applying a weighting function to prevent the inclusion of unrealistic sedimentation rates, and Step 4: identification of the best continuous spatial frequency path, adaptive filtering by the consecutive application of Taner filters along this spatial frequency path, and identification of the best age model solution.
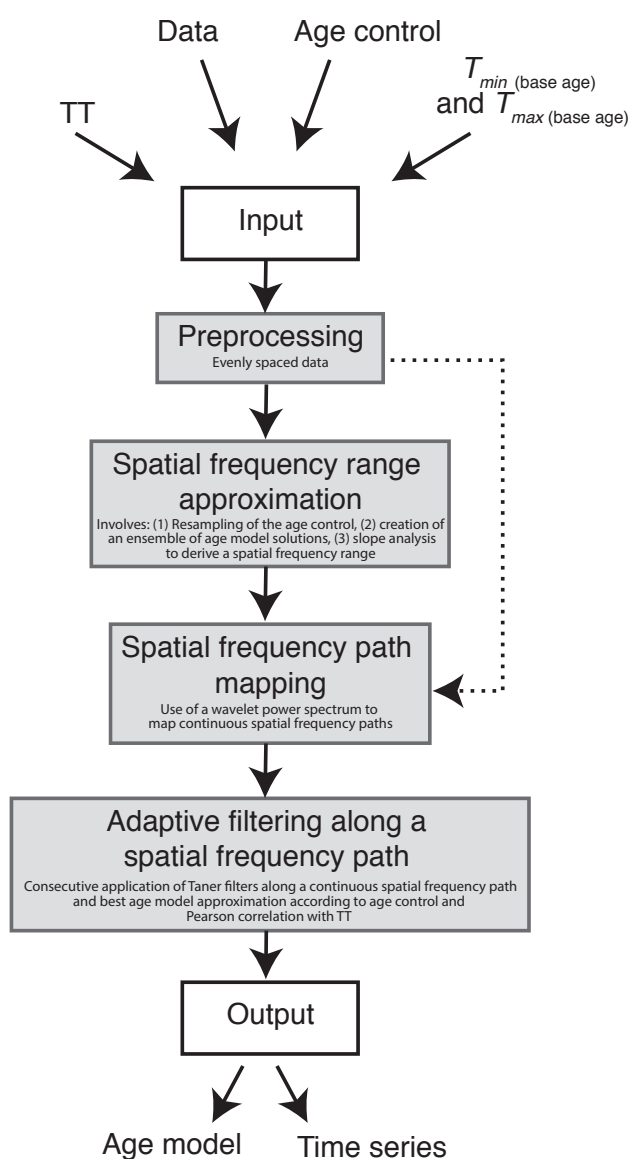

Figure 1

Flow chart of the MUBAWA algorithm, showing the individual steps involved in the analysis. Grey boxes represent MATLAB functions provided in the supplementaries. Please note that the spatial frequency range approximation step can be skipped, as indicated by the bypass arrow.

2.2 PREPROCESSING

The filter methods used in this method, as well as the CWT, require evenly spaced data and the sample size should be restricted in order to avoid long computation times. We chose a sample size that did not exceed 20 data points for each cycle occurring in the TT within the time interval between t_0 and t_{max}. We then established an evenly spaced depth vector to match the new sampling rate and interpolated the proxy values in order to obtain an evenly spaced subsampled data set. The resulting computed depth series was then used in all of the subsequent steps.

2.3 SPATIAL FREQUENCY RANGE APPROXIMATION (SFRA)

In this step we use the age control points and their corresponding uncertainties to estimate a spatial frequency range, which is defined by the frequency of the TT and the maximum and minimum slopes of the ensemble of age model solutions for each depth point. This procedure is based on the assumption that every age model solution results in a particular spatial frequency path for each depth point, depending on the frequency of the TT and the slope of the age model solution. This procedure can help to find tuned age model solutions that conform with the age control points (within their respective uncertainties). This is an optional procedure that is not essential for the determination of a frequency path, but it provides an auxiliary strategy with which to improve the chances of approximating a path that will yield results that conform with the age control points, within their uncertainty ranges.

This resampling-based approach involves obtaining random samples from the normal distribution of the available age control points and computing an age model for each set of random samples. A piecewise cubic Hermite interpolating polynomial (PCHIP; Frisch and Carlson, 1980) is used to interpolate between the resampled age control points. Using a PCHIP yields solutions that tend not to have any strong fluctuations, since the interpolations are generally more gradual and do not deviate markedly from each other in the way that they do with other methods, such as the classic cubic spline interpolation method.

The maximum and minimum slopes of the age models derived from the resampling of the age control points, are then computed for each depth point. Only monotonically increasing solutions are accepted, in order to avoid any solutions that describe time reversals. The slopes are converted into a spatial frequency range with respect to the TT. Two depth series are then generated in which the maximum slope values lead to a depth series with a low spatial frequency limit, and the minimum slope values to a depth series with a high spatial frequency limit.

The spatial frequency limits are then used to adaptively bandpass filter the regularly sampled depth series obtained from the preprocessing, using Taner filters (Taner 1992).

2.4 SPATIAL FREQUENCY PATH MAPPING

The following steps use either the adaptively filtered depth series obtained from the SFRA or, if the SFRA has not been used, the preprocessed depth data.

A continuous power spectrum (CWT) resolves the evolution of frequencies through time or space. Throughout this paper we focus on the perspective of spatial frequencies, since we are dealing with depth series. A spatial frequency path can be obtained by analyzing the frequency evolution of a CWT-based wavelet power spectrum of the input depth series. Further on in this section, we describe how we identify these paths. We then use the identified spatial frequency paths to adjust bandpass filter center points for each point in the depth series, thus creating an adaptive filter.

A wavelet is the basis function used for the wavelet transformation (WT) and can be thought of a specific wave defined by its frequency and amplitude, with the amplitude decaying to zero towards either end. Since wavelets can be stretched and translated in both frequency and space, with a flexible resolution, they can easily map changes in the spatial frequency domain (Fig. 2A and B). We define β as the depth variable such that $y(\beta)$ is the signal under consideration
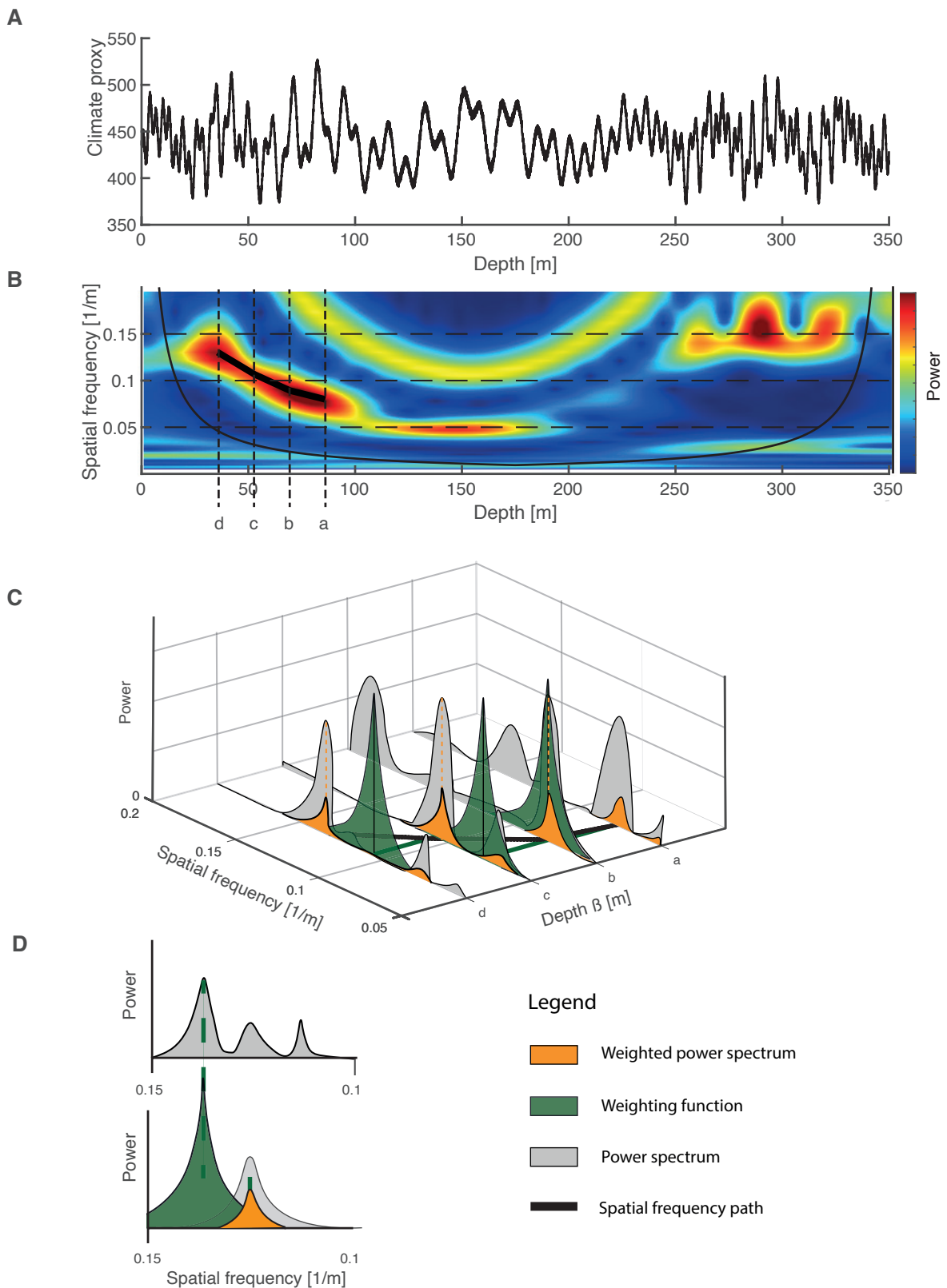
Figure 2

(A) To illustrate how to map spatial frequency paths we generated a demonstration depth series consisting of an insolation signal (from Laskar et al., 2004) and superimposed sinusoids. The result was a depth series that had been stretched and compressed by variations in the sedimentation rate. (B) We computed a CWT from the depth series and plotted the results in a wavelet power spectrum. Note that the frequency evolution followed curved paths. We extracted four profiles from the CWT, labelled a, b, c, and d. (C) Showing how continuous spatial frequency paths are mapped along the profiles a, b, c, and d. (D) Showing how a peak is detected and how the power spectrum of the next profile is weighted by application of the green weighting function. The grey peak is weighted and forms the orange weighted power spectrum.

(i.e. the climate proxy data as a function of the core depth β). A continuous wavelet transformation (CWT) mathematically decomposes $y(\beta)$ into the elementary functions $\Psi_{a,b}(\beta)$, derived from a mother wavelet $\Psi(\beta)$ by dilation and translation (Trauth, 2015; Addison, 2017). The dilation indicates a compressing or stretching of the mother wavelet $\Psi(\beta)$, resulting in a variation in its frequency, controlled by the scale parameter a. The spatial resolution of the CWT follows the translation of the mother wavelet $\Psi(\beta)$ along the depth β and is controlled by the translation parameter b (Lau and Weng, 1995). The wavelet transform of the signal $y(\beta)$ is then defined as the convolution integral

$$CWT_{\Psi}(a,b) = \frac{1}{\sqrt{a}} \int \Psi^* \left(\frac{\beta - b}{a} \right) y(\beta) d\beta \tag{1}$$

in which the asterisk indicates the complex conjugate of the mother wavelet Ψ and the factor $1/\sqrt{a}$ ensures the preservation of energy. By varying b for a range of values for the scale parameter a, the final wavelet power spectrum and the corresponding scalogram can be obtained (Equation 4, Fig. 2B).

The CWT can be computed for a broad spectrum of different mother wavelets. In geoscience, however, the complex Morlet wavelets are most widely used because they can be more easily adapted to capture oscillatory behavior (Torrence and Copo, 1988):

$$\Psi_{Morlet}(\beta) = \frac{1}{\pi^{1/4}} e^{i2\pi f_0 \beta} e^{-\beta^2/2} \tag{2}$$

from which the elementary functions

$$\Psi_{a,b}(\beta) = \frac{1}{\pi^{1/4}} e^{\left(i2\pi f_0 \frac{\beta-b}{a} \right)} e^{-\left(\frac{\beta-b}{\sqrt{2}a} \right)^2} \tag{3}$$

are derived and then used in Equation (1). Computing the CWT of the spatial data results in a complex spatial frequency output, of which the absolute value represents a wavelet power spectrum for a particular (a,b)-parameter configuration:

$$E(a,b) = | CWT(a,b) |^2 \tag{4}$$

This is called a scalogram, representing the energy density surface of the fast Fourier transform, analogous to a spectrogram (Addison 2017). Mapping $E(a,b)$ for a variety of (a,b)-parameter value pairs yields a three-dimensional frequency map (Fig. 2B) in which the x-values represent core depth-values β (related to the dilation parameter b in Equations 1, 3, and 4), the y-values represent frequencies (related to the scale parameter a in Equations 1, 3, and 4), and the color coded z-values represent the power of the (spatial) frequencies at each given β/b-value, $E_b(a)$ (Equation 1). We refer to this as the wavelet power spectrum throughout this paper. Finally the relationship between the scale parameter a and a spatial frequency f ,at depth β, is

$$a = \frac{f_c}{f} \tag{5}$$

where   is the center frequency of the Morlet wavelet used and is chosen automatically, depending on the energy spread of the wavelet in spatial frequency and depth (MathWorks, 2020a).

The wavelet power spectrum (Fig. 2B) allows us to map frequency paths by following the β-axis along a high energy ridge (represented by a continuous color band and reflecting sufficiently high energies), remaining at the highest local energy level, following changes in spatial frequency without jumping from one ridge to another (Fig. 2C). These ridges are referred to as spatial frequency paths. They represent continuous changes in the spatial frequencies within a certain power range of the signal (e.g. a color range of a band in Fig. 2B). To map a spatial frequency path we need to set starting points in the wavelet transform plot, which are derived from the absolute value of the first complex

spatial frequency output $E_{b_{first}}(a)$ (Equation 4) and its respective maxima in spatial frequency, where each maximum represents a starting point. Since we can in theory start our spatial frequency path tracking from either end of the wavelet transform plot, starting points are derived from maxima of the absolute value of the complex frequency output of the CWT, $E_{b_{first}}(a)$, from either end of the core (i.e. where $\beta = 0$ and $\beta = $ max.):

$$\text{Starting point} = \zeta_{\beta_{first}} = \max_{a} E_{b_{first}}(a)$$

In the application presented herein, in which spatial frequency paths are used to derive cutoff frequencies for adaptive filtering of the depth series, jumps in the spatial frequency paths represent abrupt changes in the sedimentation rate. These need to be avoided because the resolution of our method is limited to one cycle of the TT, and it is therefore unable to detect such abrupt changes. We therefore assume that any changes in spatial frequency occur continuously. This is achieved by introducing a weighting function that penalizes any sudden fluctuations in spatial frequency, e.g. when going from $E_{b=\beta_0}(a)$ at depth β_0 to the next point in the path $E_{b=\beta_1}(a)$ at depth β_1 (Equation 6,7). For an illustration of such a path through slices $E_b(a)$ of the wavelet transform plot see Figure 2 (C and D), in which the weighting function is highlighted in green. The weighting procedure prevents sudden jumps in the spatial frequency when following along a spatial frequency path and avoids the inclusion of a neighboring cycles. A suitable weighting function is a negative exponential function with a decay parameter $\kappa = 20$, which we place at the location of the previous spatial frequency point in the wavelet transform plot (ξ_{β_0}) before determining the next point (ξ_{β_1}):

$$\xi_0 = max(E_{b=\beta_0}(a))$$
$$\xi_1 = max(E_{b=\beta_1}(a) \cdot f_{\text{weighting}}) \tag{6}$$

with

$$f_{\text{weighting}} = e^{-\kappa \cdot |a - \xi_1|} \tag{7}$$

The frequency path analysis is sensitive to the directionality of the weighting strategy, i.e. to whether the weighting is applied top-down or bottom-up along the core. Our age model is based on spatial frequency paths that are computed bottom-up, which we interpret as the physically correct approach, assuming that the preceding spatial frequency point contains information about the subsequent spatial frequency point, proceeding along a positive time scale.

Completing this step of the algorithm typically yields a number of continuous frequency paths from which the best approximation to the orbital component needs to be identified in the following final step.

2.5 ADAPTIVE FILTERING ALONG THE SPATIAL FREQUENCY PATH

For our adaptive filter approach we use a series of Taner filters (Taner, 1992; Zeeden et al., 2018). These filters have decisive advantages over the widely used Butterworth filters due to their steep roll off rates for narrow bandpass configuration. On the other hand, the longer computation times compared to Butterworth filters are an obvious disadvantage. The method proposed herein uses continuous spatial frequency paths, identified by spatial frequency mapping, to design adaptive bandpass filters for use on the depth series along these paths, assuming that one of these paths approximates the orbital component that we ultimately want to tune. Adapting the cutoff frequencies used in the filtering process allows continuous variations in sedimentation rates, which ultimately cause changes in the wavelength of the orbital component, to be taken into account.

The spatial frequency path mapping usually yields a number of possibly suitable paths. The following steps are performed with all of the spatial frequency paths that resulted from the previously described spatial frequency mapping. Each frequency path is first smoothed using a 20 data point Gaussian filter, in order to avoid abrupt changes

in frequency. Both forward and reverse filtering are used to avoid phase shifts. The frequency paths are then converted into a lower cutoff depth series and an upper cutoff depth series. (For the lower cutoff frequency we subtracted one sixth of the frequency of the spatial frequency path and for the upper cutoff frequency we added one sixth: these values were found to be practicable for our purposes.) The result is a frequency tube enclosing the frequency path used.

Each data point in the entire time series is then filtered separately using Taner filters. From the results of the filtering a new adaptively filtered composite depth series is created in which each value is the result of an individual bandpass filter setting that was derived from a particular spatial frequency path. To reduce any noise that can derive from the adaptive filtering, the resulting composite depth series is filtered with a Taner filter. The upper cutoff frequency is set to the maximum cutoff frequency of the spatial frequency path that was used for the adaptive filtering and the lower cutoff frequency to the minimum cutoff frequency.

The set of maxima appearing in each of the adaptively filtered depth series is then determined. The first and last maxima of the adaptively filtered depth series are rejected in order to avoid edge effects at either end of the wavelet power spectrum. An age model can be obtained for each of the spatial frequency paths by assigning the remaining maxima in the adaptively filtered depth series to the minima of the TT, translating each adaptively filtered depth series into a time series. Each age model is applied to the filtered time series and an adaptively filtered time series thus obtained.

In order to identify the most suitable age model on the basis of its agreement with age control points and the TT, each age model is ranked using the following procedure. For each age control point (and uncertainty) that is included, the age model corresponding to the time series is assigned a score of one point. Pearson correlation coefficients between each of the adaptively filtered time series and the TT are also used to provide an indication of the degree of correlation. The age model corresponding to the time series that has the highest degree of correlation gains an additional point. The age model and its corresponding time series that has the highest final score is rated as the best age model. The full data set is then interpolated using the best age model approximation and the maximum sampling rate, as defined by the length of the original data set.

2.6 TRADITIONAL TUNING

We compared the MUBAWA tuning technique with an established tuning technique widely used in paleoceanography (e.g., Hays et al., 1976; Imbrie et al., 1984). In contrast to the MUBAWA method, established tuning approaches use a preliminary estimate for the basal age of the core (e.g. from magnetostratigraphy) and interpolate an environmental proxy (such as benthic oxygen isotopes) to a preliminary age scale, before then bandpass filtering and tuning this proxy to an orbital cycle (e.g. Earth's precession cycle) as the TT. The maxima of the filtered time series are then interpolated to the minima of orbital precession based, for example, on the solution by Laskar et al. (2004). Both time series are then in phase and the age model is complete.

3 MATERIALS
3.1 SYNTHETIC DATA FOR TESTING

To test the MUBAWA algorithm we produced synthetic data using an insolation signal for 4°N and 35°E from Laskar et al. (2004), covering the past 800 kyrs with a sampling interval of 100 years. In addition to the insolation signal, we added a distinct 10-kyr cycle and a distinct 100-kyr cycle as two sine waves. Adding extra cycles to the quasi monochromatic insolation signal produced synthetic data that was closer to real climate data, in which multiple continuous frequencies can occur. We created an artificial age model that was characterized by a continuous increase in sedimentation rates down core from 0.3 m/kyr to 0.9 m/kyr, transferred the time series into a space series, and added white noise. For age control points we generated randomly distributed ages that were resampled from the time series, simulating, for example, the presence of Argon-dated volcanic ash layers in the core. The result was a synthetic depth series that was derived from a time series and in which the sediment deposition rate varied with time, simulating a climate proxy record.

The Chew Bahir sediment cores described herein were collected from the Chew Bahir paleolake basin in the southern Ethiopian Rift (4.1–6.3°N, 36.5–38.1°E; Fig. 3), a segment of the East African Rift System (EARS). The Chew Bahir record discussed in this work is a composite record from duplicate sediment cores, HSPDP-CHB14-2A and HSPDP-CHB14-2B (Foerster et al., 2019). In the following sections we use meter composite depth [m.c.d.] as our unit for depth.
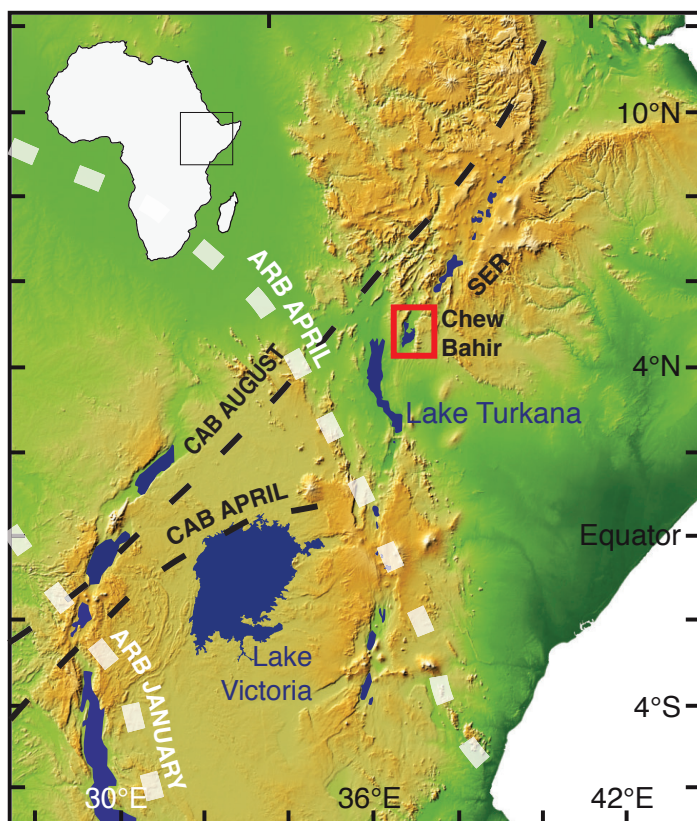

Figure 3
The Chew Bahir basin is located in southern Ethiopia, within the southern Ethiopian rift (indicated by the red box). Rainfall in the area is determined by the annual migration of the tropical rain belt (TRB), and on inter annual time scales by the migration of the Congo air boundary (CAB). On millennial time scales rainfall shows a strong correlation with orbital precession cycles.

Rainfall in the area is determined by the migration of the tropical rain belt, which in turn follows the zenith of the sun and results in two rainy seasons (Nicholson, 2017). During the Pleistocene, African climatic changes on millennial time scales are thought to have been caused by periodic (23-19 kyr) variations in insolation resulting from Earth's orbital precession (e.g., Kutzbach and Street-Perrott, 1985; Berger et al., 2006). Due to the geometry of precession, changes in summer solar radiation are anti-phased between hemispheres, resulting in maximum monsoonal circulation and maximum precipitation every 19–23 kyrs in northern and southern Africa (Partridge et al., 1997; Trauth et al., 2003; Berger et al., 2006). In contrast, periods of increased humidity in equatorial East Africa occurred at 10–11 kyr intervals following maximum equatorial insolation in March and September (Trauth et al., 2003; Berger et al., 2006).

For this study, with its focus on calculating an age model by orbital tuning, we used the 39 band color reflectance data, which show distinct continuous cycles at ~10–15 m and ~40 m depth intervals. Past variations in rainfall are reflected in the color of the sediments of the Chew Bahir basin, with blue-green colors during wet episodes and reddish-brown colors during dry episodes (Foerster et al., 2012). The sediment color can be primary, resulting from direct detrital sediment input, or secondary, due to diagenesis of the deposited sediments by, for example, redox processes at the sediment-water boundary under lacustrine conditions (Giosan et al., 2002 and references therein). Color reflectances within the blue green spectrum suggest reactions at the sediment-water boundary as a result of H_2S production, fueled by organic matter and its consumption by sulfate reducing bacteria. H_2S in the anoxic zone at the water-sediment boundary reacts with iron hydroxides, reducing any Fe^{3+} that is attached to clay minerals, bound in

iron-hydroxides, or present in aqueous solution. During this process mono-sulphides and pyrite form on the lake floor and within the uppermost centimeters of sediment (Giosan et al., 2002), resulting in a spectral shift towards green/blue reflectances.

Organic matter input can derive from algal blooms within the lake and from plant material washed into the lake from the Chew Bahir catchment area. Algal blooms are in turn driven by nutrient and iron influx to the lake system (Storch and Dunham, 1986). Dissolved iron (Fe) and iron hydroxide may originate from the catchment areas at the upper eastern edge of the Chew Bahir basin, from the Teltele Plateau, and from the northeastern part of the catchment, where volcanic rocks are exposed to weathering (Foerster et al., 2012). Wind-blown dust from more distant sources may also have contributed to the nutrient and iron flux into the lake (Foerster et al., 2012). In the absence of oxygen the reduced minerals retain their diagenetic signatures and associated color reflectances until they are eventually sealed off from the lake water and possible chemical alteration by subsequent sedimentation.

We used a principal component analysis (PCA) to unmix the environmental factors controlling sediment color and to increase the signal-to-noise ratio, as well as to assist in interpreting the multivariate data set. The first principal component (PC1) showed similar loadings for all color bands; it was interpreted to represent the total reflectance of the sediment and was not used in this method. We Instead used PC2 (3.4% of the total variance), with positive loadings within the short wavelengths (blue reflected light), as a proxy for precipitation within the catchment area (Fig. 4A and B). Complete linear unmixing was, however, not possible because the intensity values within individual wavelength bands were not perfectly Gaussian distributed.

We also used six Argon ages, which date the sediment a the bottom of the core to 629±11 kyrs BP (one sigma error) (Roberts et al., submitted).
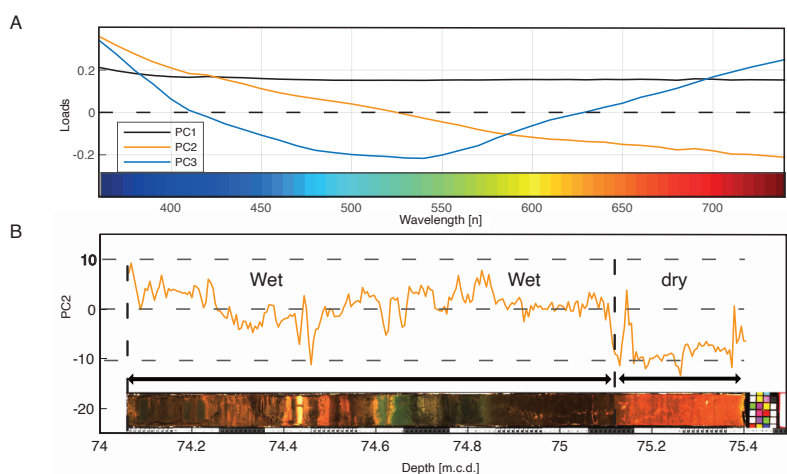

Figure 4

(A) To extract the environmental signal from the 39 band color reflectance data set we used a principal component analysis (PCA). The first three principal components explained 99.88% of the total variance. We used the 2nd principal component (PC2) as an environmental indicator, with positive values indicating wet periods.

(B) The PC2 corresponds to red blue green color shifts that are characteristic for the sediments of the Chew Bahir core displayed at the bottom of the diagram. The colors of the core have been photographically enhanced.

4 RESULTS

4.1 SYNTHETIC DATA RESULTS

We first applied the new MUBAWA technique, including the SFRA, to the synthetic data set. To visualize the frequency evolution of the synthetic data we computed a wavelet power spectrum (Fig. 5A). We used the time series of orbital precession between –1.0 and 0 Ma BP from Laskar et al. (2014) as the TT and the synthetic ages as the age control points for our hypothetical core. We selected a minimum base age of 550 kyrs BP (t_{min}) and a maximum base age of 850 kyrs BP (t_{max}).

The reconstructed accumulation rates calculated using MUBAWA age modeling largely correspond to the true (synthetic) accumulation rates (Fig. 5, B and C). A closer look at the results reveals minor deviations of the modeled accumulation rate from the true accumulation rate. The maximum age of the core determined from the synthetic data by MUBAWA age modeling, agrees well with the true maximum age.

In order to compare the results obtained from the MUBAWA method with those obtained using established tuning methods, we reconstructed the accumulation rate of the synthetic data using a traditional tuning method. We first transformed the space series into a time series with a maximum age of 800 kyrs BP. We then bandpass filtered the signal to extract the 19–23 kyr cycle that we wanted to use as the TT. Since we knew that the time series had been compressed and stretched by varying sedimentation rates, we chose a relatively wide passband with cutoff frequencies of 1/15 kyr-1 and 1/30 kyr-1 for the filter. Finally, we aligned the maxima of the filtered time series with the minima of the TT.

Although the traditional tuning method found the correct base age for the synthetic data, it did not reconstruct the accumulation rates of the synthetic example correctly. In order to visualize which spatial frequencies resulted in the final traditionally tuned age model we used peak distances, these being the distances between each of the peaks in the filtered depth series. The variations in these distances ultimately determine the age model. A projection of the inverse of the peak distances into a wavelet power spectrum reveals which of the spatial frequencies the tuned age model is based on. The projection of the inverse of the peak distances into the wavelet power spectrum showed that the traditional method generated an age model on the basis of different spatial frequency paths from our original insolation signal. The reconstructed accumulation rates diverged from the "true" accumulation rates where the peak distances projected into the wavelet power spectrum failed to follow the continuous spatial frequency evolution of our initial insolation signal (Fig. 5A, B andC). The result obtained using the traditional tuning method cannot be considered satisfactory, indicating the need for a different strategy that avoids such a failure. The MUBAWA approach, which clearly follows a continuous spatial frequency path, provides such an alternative strategy.
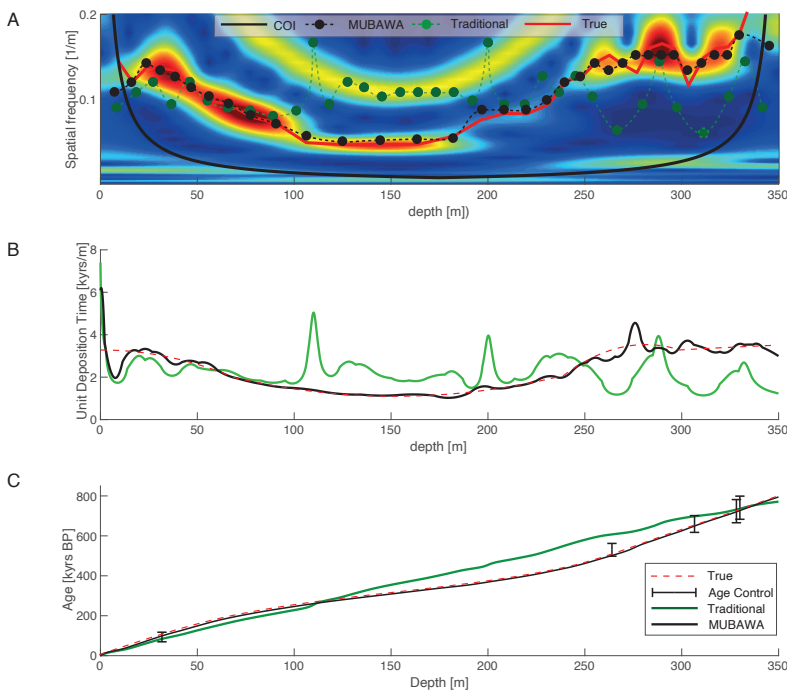

Figure 5
(A) The wavelet power spectrum that resulted from the CWT of the synthetic depth data demonstrates the frequency shift that has been applied by the continuous sedimentation rate changes induced by the synthetic age model. Blue colors refer to low power and red colors to high power. The green dots represent the peak distances of the filtered linear interpolated time series from the first step of the traditional tuning method. Note that where the peak distances do not follow a continuous frequency path, the traditional tuning method failed to reconstruct the synthetic sedimentation rate shown in (B). (C) The depth-age plot shows that even though the traditional method failed to reconstruct the correct sedimentation history, it yielded a similar base age.

4.2 CHEW BAHIR DATA RESULTS

We first created a linear age model by extrapolating through the age control at 240 m (400 kyrs). We used this age because a similar age has been obtained from the same depth in the parallel core (Roberts et al., 2019). The age model yielded a base age of 570 kyrs. We calculated a Lomb-Scargle power spectrum for the time series and computed the detection probability limit (Lomb, 1976; Scargle, 1982) (Fig. 6). We found power above the detection probability limit within the precession frequency range (PFR). The possible precession cycles indicated by the simple linear age model suggested that the cycles already observed in the depth scale were indeed related to orbital precession.

We then used the MUBAWA algorithm to calculate an orbitally-tuned age model for the Chew Bahir composite core. We used PC2 from the color reflectance data, an orbital precession (according to Laskar et al., 2014) of between −1 and 0 Ma BP as the TT, and the Argon ages (together with their uncertainties) as age control points. We rejected the Argon age at a depth at 234.066 m.c.d. because of its large uncertainty and its proximity to the age date at 234.048 m.c.d., which had a smaller uncertainty. We chose 850 kyrs as the maximum base age (t_{max}) and 550 kyrs as the minimum base age (t_{min}). Preprocessing with the MUBAWA function resulted in a sampling rate of 0.3661 m^{-1}. The resulting evenly spaced subsampled data set contained 800 data points.
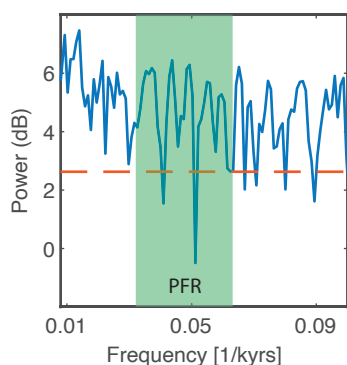

Figure 6
Lomb-Scargle power spectrum derived from a simple linear age model. The green color represents the precession frequency range (PFR) within which the precession frequencies can be expected to occur. The red line indicates the 95% detection probability. Frequencies within the PFR are above the detection probability suggesting that there is enough power within the precession band to run the MUBAWA approach.

We then used the SFRA to approximate the frequency range that corresponded to the age control (within their uncertainty ranges) by randomly resampling the age control points to create an age model ensemble (Fig. 7A). The SFRA resulted in a relatively broad frequency range in the top and bottom sections of the core, where more radiometric ages were available, and a narrower range in between (Fig.7B).

We used Taner filters to adaptively bandpass filter the y-values using the upper and lower frequency limits from the SFRA, thus obtaining an adaptively filtered depth series. We performed the spatial frequency path mapping using the data from the SFRA. Ten different spatial frequency paths were mapped. All paths had different starting positions but merged after a certain depth (Fig. 7B). We adaptively filtered along the frequency paths by adjusting the cutoff frequencies of the Taner filters according to the values of each individual frequency path.

Each frequency path resulted in an adaptively filtered depth series. We computed the maxima of the depth series and the minima of the TT, as negative precession resulted in an increase in monsoon strength within the study area. The interpolation points were then arranged in chronological order so that the second maximum of the filtered time series and the second minimum of the TT were assigned to each other, until the penultimate maxima of the filtered time series. We omitted the first and last maxima to avoid any edge effect of the wavelet power spectrum.
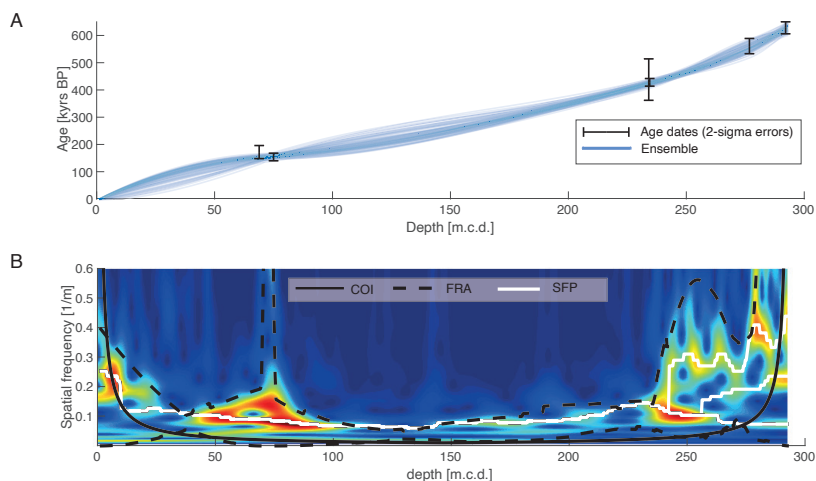

Figure 7
(A) We computed 100,000 realizations (blue lines) between the randomly resampled age control points to approximate a spatial frequency range depending on the frequency of the TT and the minimum and maximum slopes of the age model ensemble. (B) The wavelet power spectrum of the adaptively filtered PC2, with blue colors indicating low power and red colors high power. The SFRA resulted in the black dashed lines that have been used to adaptively filter the depth series. The white lines are spatial frequency paths that resulted from the spatial frequency mapping. Note that we left out the age at 230 m.c.d. from the SFRA because it was very close to a better dated age with less uncertainty (close ages expand the SFRA).
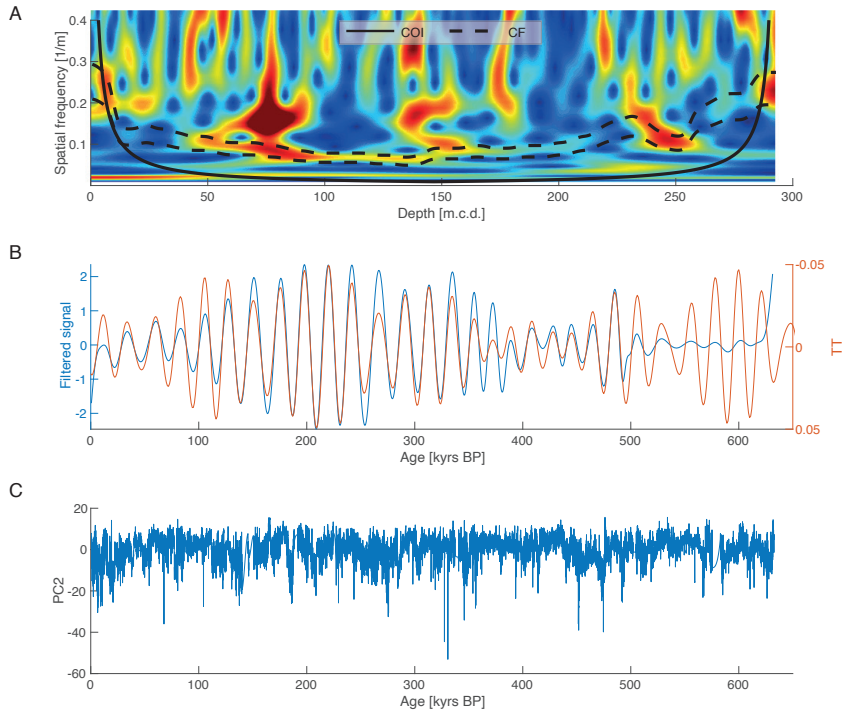
Figure 8
(A) Each frequency path was converted into an upper and lower cutoff frequency to adaptively filter along the spatial frequency path. The cutoff frequencies that resulted in the best age model are shown as black dashed lines. (B) The peaks of the adoptively filtered signal were consecutively projected onto the peaks of the tuning target (TT) to generate an age model. (C) The age model was used to convert the PC2 depth series into a time series, as shown.
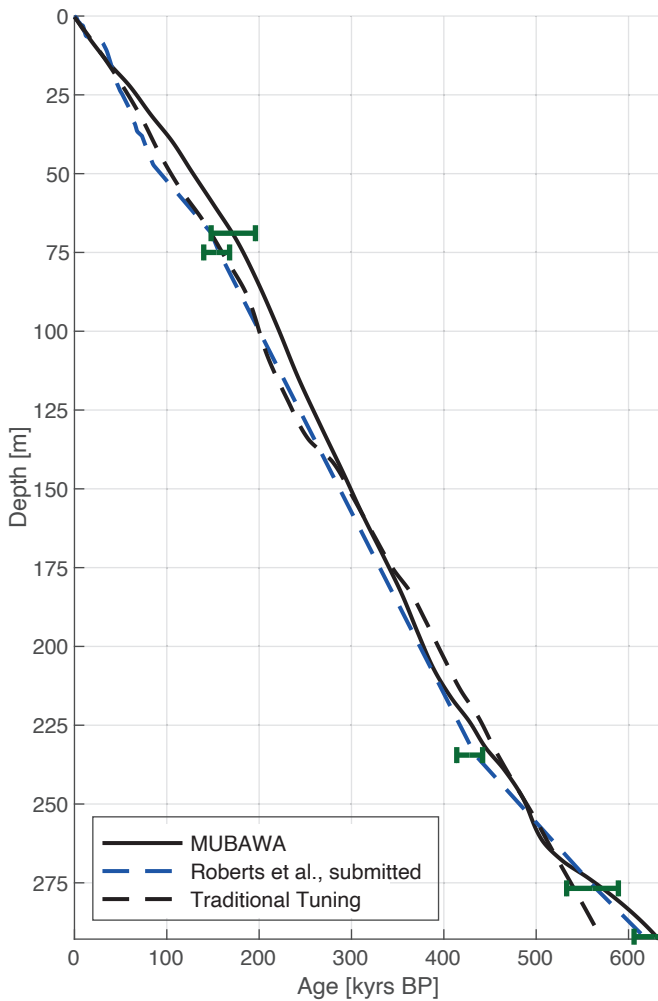

Figure 9
Two additional age models have been developed for the Chew Bahir project: a direct-dated age model (Roberts et al., submitted) and a traditionally tuned age model. Note that the MUBAWA age model is in strong agreement with the age controls.

Multiband wavelet age modeling (MUBAWA) for a ~293 m (~600 kyr) sediment core from Chew Bahir basin, southern Ethiopian Rift

We then used a PCHIP to interpolate between the new tie-points, derived by assigning the maxima of the adaptive filtered depth series to the minima of the TT, and generated an age model for each spatial frequency path. We used the agreement between the age models resulting from the interpolation and the age control points (within their uncertainties) to evaluate the age models. We also used the Pearson correlation coefficient to rate the age models. The cutoff frequencies that eventually led to the best age model are shown in Fig. 8 A. The adaptively filtered time series then correlated with the TT (Fig. 8B). Applying the resulting age model to the original data results in a time series of PC2 (Fig. 8C). This analysis resulted in an age model that was in agreement with most of the age control points (within their two sigma errors) and indicated a maximum age for the base of the core of 632.62 kyrs BP (Fig. 9). We applied our MUBAWA-based age model to the PC2 of the 39 band color reflectance record; the wavelet power spectrum of the resulting time series showed significant orbital cycles with periods of 100, 60, 19-25, 10-15, and 5 kyrs (Fig. 10).

In order to further compare our MUBAWA approach with the traditional method we also applied the previously described traditional tuning method to the Chew Bahir data. For this we first assumed a preliminary base age of 500 kyrs. We generated a time series based on this simple linear preliminary model and then applied a relatively wide bandpass filter with cutoff frequencies of 1/28 kyr^{-1}. and 1/16 kyr^{-1}. Both methods can be seen from the peak distances to operate in the same frequency domain (Fig 11A). The accumulation rates show a strong correlation with the peak distances (Fig. 11B). The age-depth gradients differ only slightly and remain within the uncertainties of the Argon ages (Fig. 11 C).
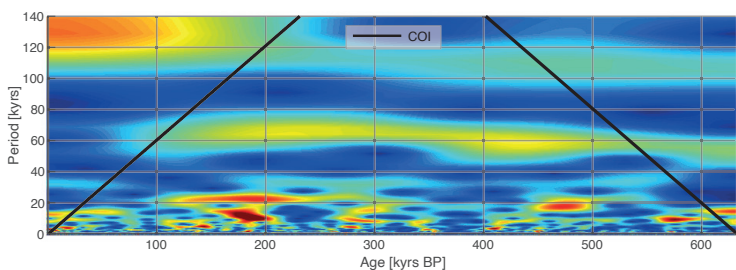
Figure 10
Wavelet power spectrum, with the age along the x-axis and the period along the y-axis. The colors indicate the power of the cycle, with red colors for high power and blue colors for low power. The wavelet power spectrum computed from the PC2 time series shows the anticipated precession cycles, since the age model was tuned to that cycle. The continuity of the longer wavelength periods at 60 kyrs and 100-120 kyrs shows that the tuning has been successful.
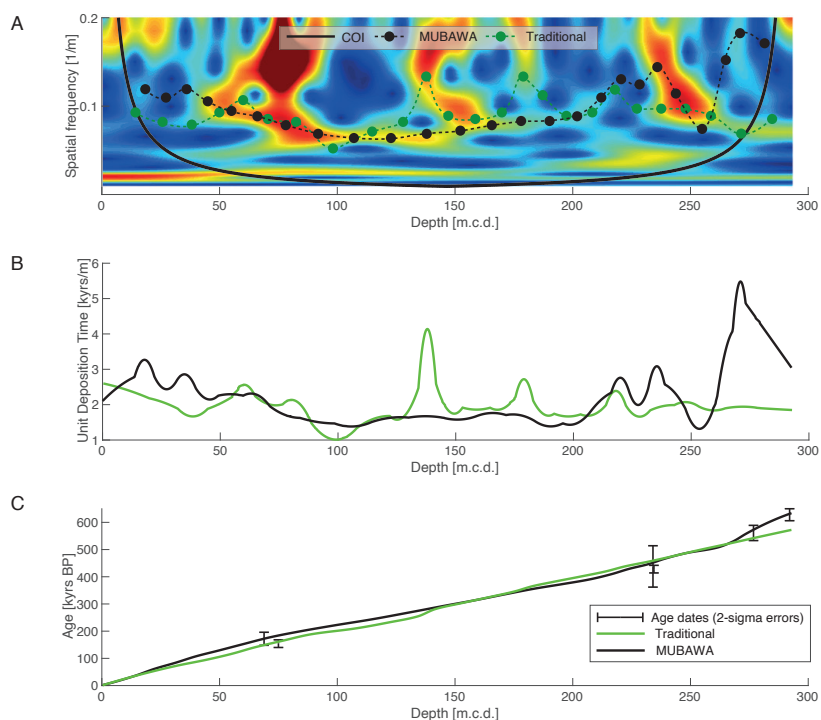
Figure 11
(A) Wavelet power spectrum, with frequency along the y-axis and depth along the x-axis. The power is indicated by color, with red colors for high power and blue colors for low power. The peak distances can be used to compare the traditional approach with the new MUBAWA approach. Both methods follow approximately the same cycle until 230 m.c.d., after which they show marked differences. (B) Where the peak distances differ in (A), the accumulation rates are significantly different. (C) The two age models only vary insignificantly in the depth age plot. However, the MUBAWA model tracks to higher frequencies below 250 m.c.d. on, which allows it to reach the argon age at the base of the composite core.

5 DISCUSSION

We have developed a new age modeling technique that is specifically suited to climate records with distinct orbital cycles and limited age control. The approach involves statistical analysis of an age model ensemble to delimit the spatial frequency range of the targeted orbital frequency. It uses a wavelet power spectrum derived from the CWT to trace the evolution of the orbital frequency and ultimately adapt the bandpass filter to its variations, allowing for continuous long-term changes in sedimentation rates. This new technique is in improvement on traditional tuning techniques that use a single bandpass filter to tune paleoclimate records. The method depends on a number of parameters that may need to be adjusted when using data sets other than those presented herein. These include the amount of weighting, the sampling rate, and the bandwidth of the adaptive filter.

By applying a traditional tuning method to synthetic data we have shown that when the data to be tuned are characterized by continuous long-term changes in sedimentation rates, jumps occur in the spatial frequency that lead to misinterpretation of the spectral data and ultimately to a false age model. We have shown that such misinterpretation of the data set can be detected by plotting the peak distances of the filtered, but untuned, time series into a wavelet power spectrum of the untuned raw spatial data. If the peak distances correspond to a continuous frequency evolution, the traditional tuning method will produce accurate results. If, however, the peak distances show no match with a continuous frequency evolution the method will fail to deliver accurate results. It is specifically for cases resembling the synthetic data, which are common in nature, that we have developed the MUBAWA method. The MUBAWA technique has demonstrated its ability to handle such special circumstances by correctly solving the synthetic example.

Application of the MUBAWA approach to the Chew Bahir record and using PC2 from its color reflectance data set has produced a tuned age model that is in strong agreement with independent age controls and shows continuous orbital cycles in the wavelet power spectrum. As expected, the tuning revealed particularly distinct cycles corresponding to frequencies contained in the TT. Furthermore, a set of higher frequencies with periods of ~5 kyr that, according to Berger et al. (2006), are attributable to fundamental harmonics, can be identified in the tuned time series. The occurrence of a distinct ~10–15 kyr cycle suggests half precessional forcing of the Chew Bahir environmental conditions, as previously suggested by Berger et al. (1997, 2006), Berger and Loutre (1997), and Trauth et al. (2003). We also identified a distinct continuous 63 kyr cycle. Its occurrence can possibly be attributed to heterodynes, as described by Clemens et al. (2010, 2018) and recently identified in South Asian precipitation records (Gebregiorgis et al., 2018). We also recognized a continuous 100 kyr cycle that can be ascribed to eccentricity in the earth's orbit (Fig. 10).

We also created a traditional tuned age model (according to common practice) using the Chew Bahir data, for comparison with the MUBAWA age model. The result again revealed a strong agreement with the age control points (Fig. 11C), with the exception of the oldest age at the base of the composite core. This model would certainly be a satisfactory result for users of established tuning methods. To compare the resulting filtered depth series of the MUBAWA approach with the traditionally tuned filtered depth series we plotted the peak distances of the traditionally tuned filtered depth series and the peak distances of the MUBAWA filtered depth series into the wavelet power spectrum (Fig. 11 A), as demonstrated previously for the synthetic example.

The peak distance analysis revealed that, despite the agreement with the age control points and the increase in the power of the eccentricity cycle, a discontinuous spatial frequency evolution had been used through parts of the composite core. The synthetic data example showed that such jumps in spatial frequency can lead to misinterpretations (Fig. 11A). Although real data are far more complex and the exact sedimentation history of such data is largely unknown, we believe that the continuity assumption in our MUBAWA approach enables it to make an important contribution to tuning-based age modeling.

CONCLUSION

We have demonstrated in our synthetic example that tuning methods using stationary bandpass filters have difficulty reconstructing the correct accumulation history, whereas the MUBAWA algorithm presented herein, using the CWT to track a continuous frequency evolution, yielded the correct solution. Application of the MUBAWA approach to the Chew Bahir record and the PC2 of its color reflectance data revealed that the method is also applicable to real climate data sets. A comparison with traditional tuning showed that, whereas the traditional tuning method is limited to rather linear age models, the MUBAWA approach is capable of detecting and taking into account continuous long-term changes in sedimentation rates. Not only was the MUBAWA-generated age model in good agreement with the available age control points (within their uncertainties), but it was also able to reconstruct continuous orbital cycles, as shown in the wavelet power spectrum. We recommend the MUBAWA approach for use with a wide range of climate data sets that require sophisticated tuning methods.

ACKNOWLEDGMENTS

REFERENCES

Addison, P. S. (2017). The illustrated wavelet transform handbook: introductory theory and applications in science, engineering, medicine and finance. 2nd Ed. India: CRC Press.

Berger, A., & Loutre, M. F. (1997). Intertropical latitudes and precessional and half-precessional cycles. Science, 278(5342), 1476-1478.

Berger, A., Loutre, M. F., & Mélice, J. L. (2006). Equatorial insolation: from precession harmonics to eccentricity frequencies. Climate of the Past, 2(2), 131-136.

Campisano, F. A., Drake, A. J., Floyd, M. S., Hui, D. T., Owczarczyk, P., Tiner, M. D., & Yuan, X. (2017). U.S. Patent Application No. 14/879,269.

Cheung, Wing H., Gabriel B. Senay, and Ashbindu Singh. „Trends and spatial distribution of annual and seasonal rainfall in Ethiopia.“ International Journal of Climatology 28.13 (2008): 1723-1734.

Clemens, S. C., Prell, W. L., & Sun, Y. (2010). Orbital-scale timing and mechanisms driving Late Pleistocene Indo-Asian summer monsoons: Reinterpreting cave speleothem δ18O. Paleoceanography, 25(4).

Clemens, S. C., Holbourn, A., Kubota, Y., Lee, K. E., Liu, Z., Chen, G., ... & Fox-Kemper, B. (2018). Precession-band variance missing from East Asian monsoon runoff. Nature communications, 9(1), 3364.

Cohen, A., Campisano, C., Arrowsmith, R., Asrat, A., Behrensmeyer, A. K., Deino, A., ... & Lamb, H. (2016). The Hominin Sites and Paleolakes Drilling Project: inferring the environmental context of human evolution from eastern African rift lake deposits. Scientific Drilling.

Davidson, A., (1983). The Omo River project: reconnaissance geology and geochemistry of parts of Ilubabor, Kefa, Gemu Gofa and Sidamo. Ethiopian Institute of Geological Surveys Bulletin, 2, 1-89.

Ebinger, C. J., Yemane, T., Harding, D. J., Tesfaye, S., Kelley, S., & Rex, D. C. (2000). Rift deflection, migration, and propagation: Linkage of the Ethiopian and Eastern rifts, Africa. Geological Society of America Bulletin, 112(2), 163-176.

Foerster, V., Junginger, A., Langkamp, O., Gebru, T., Asrat, A., Umer, M., ... & Trauth, M. H. (2012). Climatic change recorded in the sediments of the Chew Bahir basin, southern Ethiopia, during the last 45,000 years. Quaternary International, 274, 25-37

Fritsch, F. N. & R. E. Carlson (1980). Monotone Piecewise Cubic Interpolation. SIAM Journal on Numerical Analysis, 17, 238–246.

Gebregiorgis, D., Hathorne, E. C., Giosan, L., Clemens, S., Nürnberg, D., & Frank, M. (2018). Southern Hemisphere forcing of South Asian monsoon precipitation over the past~ 1 million years. Nature communications, 9(1), 4702.

Giosan, L., Flood, R. D., & Aller, R. C. (2002). Paleoceanographic significance of sediment color on western North Atlantic drifts: I. Origin of color. Marine Geology, 189(1), 25-41.

Grant, K. M., Rohling, E. J., Westerhold, T., Zabel, M., Heslop, D., Konijnendijk, T., & Lourens, L. (2017). A 3 million year index for North African humidity/aridity and the implication of potential pan-African Humid periods. Quaternary Science Reviews, 171, 100-118.

Hays, J. D., Imbrie, J., & Shackleton, N. J. (1976, December). Variations in the Earth's orbit: pacemaker of the ice ages. Washington, DC: American Association for the Advancement of Science.

Hinnov, L. A. (2013). Cyclostratigraphy and its revolutionizing applications in the earth and planetary sciences. GSA Bulletin, 125(11-12), 1703-1734.

Hotelling, H. (1933). Analysis of a complex of statistical variables into principal components. Journal of educational psychology, 24(6), 417.

Imbrie, J., and Imbrie, J. Z. (1980). Modeling the climatic response to orbital variations. Science 207 (4434), 943–953. doi:10.1126/science.207.4434.943

Kutzbach, J. E., & Street-Perrott, F. A. (1985). Milankovitch forcing of fluctuations in the level of tropical lakes from 18 to 0 kyr BP. Nature, 317(6033), 130.

Laskar, J., Gastineau, M., Joutel, F., Robutel, P., Levrard, B., Correia, A., (2004). A long term numerical solution for the insolation quantities of Earth. Astronomy and Astrophysics, 428, 261-285, available online at http://vo.imcce.fr/insola/earth/online/earth/online/.

Lau, K.-M., and Weng, H. (1995). Climate signal detection using wavelet transform: how to make a time series sing. Bull. Am. Meteorol. Soc. 76 (12), 2391–2402. doi:10.1175/1520-0477(1995)076<2391:csduwt>2.0.co;2

Lomb, N. R. (1976). Least-Squares Frequency Analysis of Unequally Spaced Data. Astrophysics and Space Science 39, 447–462.

Martinson, D. G., Pisias, N. G., Hays, J. D., Imbrie, J., Moore, T. C., & Shackleton, N. J. (1987). Age dating and the orbital theory of the ice ages: Development of a high-resolution 0 to 300,000-year chronostratigraphy 1. Quaternary research, 27(1), 1-29.

MathWorks, (2020a). MATLAB Signal Processing Toolbox – User's Guide. The MathWorks, Inc., Natick, MA.

Meyers, S. R., Sageman, B. B., & Hinnov, L. A. (2001). Integrated quantitative stratigraphy of the Cenomanian-Turonian Bridge Creek Limestone Member using evolutive harmonic analysis and stratigraphic modeling. Journal of Sedimentary Research, 71(4), 628-644.

Meyers, S. R., & Sageman, B. B. (2007). Quantification of deep-time orbital forcing by average spectral misfit. American Journal of Science, 307(5), 773-792.

Meyers, S. R. (2015). The evaluation of eccentricity-related amplitude modulation and bundling in paleoclimate data: an inverse approach for astrochronologic testing and time scale optimization. Paleoceanography 30 (12), 1625–1640. doi:10.1002/2015pa002850

Muller, R. A., & MacDonald, G. J. (2002). Ice ages and astronomical causes: data, spectral analysis and mechanisms. Springer Science & Business Media.

Nicholson, S. E. (2017). Climate and climatic variability of rainfall over eastern Africa. Reviews of Geophysics, 55(3), 590-635.

Park, J., & Herbert, T. D. (1987). Hunting for paleoclimatic periodicities in a geologic time series with an uncertain time scale. Journal of Geophysical Research: Solid Earth, 92(B13), 14027-14040.

Partridge, T. C. (1997). Cainozoic environmental change in southern Africa, with special emphasis on the last 200 000 years. Progress in Physical Geography, 21(1), 3-22.

Pearson, K. (1901). LIII. On lines and planes of closest fit to systems of points in space. The London, Edinburgh, and Dublin Philosophical Magazine and Journal of Science, 2(11), 559-572.

Pik, R., Marty, B., Carignan, J., Yirgu, G., & Ayalew, T. (2008). Timing of East African Rift development in southern Ethiopia: Implication for mantle plume activity and evolution of topography. Geology, 36(2), 167-170.

Pisias, N. G., Martinson, D. G., Moore Jr, T. C., Shackleton, N. J., Prell, W., Hays, J., & Boden, G. (1984). High resolution stratigraphic correlation of benthic oxygen isotopic records spanning the last 300,000 years. Marine Geology, 56(1-4), 119-136.

Raymo, M. E., Oppo, D. W., & Curry, W. (1997). The mid-Pleistocene climate transition: A deep sea carbon isotopic perspective. Paleoceanography and Paleoclimatology, 12(4), 546-559.

Saji, N. H., Goswami, B. N., Vinayachandran, P. N., & Yamagata, T. (1999). A dipole mode in the tropical Indian Ocean. Nature, 401(6751), 360.

Scargle, J. D. (1982). Studies in Astronomical Time Series Analysis. II. Statistical Aspects of Spectral Analysis of Unevenly Spaced Data. Astrophysical Journal 263, 835–853.

Segele, Z. T., Richman, M. B., Leslie, L. M., & Lamb, P. J. (2015). Seasonal-to-interannual variability of ethiopia/horn of Africa monsoon. Part II: Statistical multimodel ensemble rainfall predictions. Journal of Climate, 28(9), 3511-3536.

Seleshi, Y., & Zanke, U. (2004). Recent changes in rainfall and rainy days in Ethiopia. International journal of climatology, 24(8), 973-983.

Sinnesael, M., Zivanovic, M., De Vleeschouwer, D., and Claeys, P. (2018). Spectral moments in cyclostratigraphy: advantages and disadvantages compared to more classic approaches. Paleoceano. Paleoclimatol. 33 (5), 493–510. doi:10.1029/2017pa003293

Storch, T.A., Dunham, V.L., (1986). Iron-mediated changes in the growth of Lake Erie phytoplankton and axenic algae cultures. J. Phycol. 22, 109–117.

Taner, M.T., (1992). Attributes Revisted. Technical Report. Rock Solid Images, Inc. http://www.rocksolidimages.com/attributes-revisited/#_Toc328470897.

Tiedemann, R., Sarnthein, M., & Shackleton, N. J. (1994). Astronomic timescale for the Pliocene Atlantic δ18O and dust flux records of Ocean Drilling Program Site 659. Paleoceanography, 9(4), 619-638.

Torrence, C., & Compo, G. P. (1998). A practical guide to wavelet analysis. Bulletin of the American Meteorological Society, 79(1), 61-78.
Trauth, M. H., Deino, A. L., Bergner, A. G., & Strecker, M. R. (2003). East African climate change and orbital forcing during the last 175 kyr BP. Earth and Planetary Science Letters, 206(3-4), 297-313.

Trauth, M. H., Deino, A. L., Bergner, A. G., and Strecker, M. R. (2003). East African climate change and orbital forcing during the last 175 kyr BP. Earth Planet Sci.
Lett. 206 (3–4), 297–313. doi:10.1016/s0012-821x(02)01105-6

Wagner, B., Vogel, H., Francke, A., Friedrich, T., Donders, T., Lacey, J. H., ... & Zanchetta, G. (2019). Mediterranean winter rainfall in phase with African monsoons during the past 1.36 million years. Nature, 1-5.

Woldegabriel, G., Aronson, J. L., & Walter, R. C. (1990). Geology, geochronology, and rift basin development in the central sector of the Main Ethiopia Rift. Geological Society of America Bulletin, 102(4), 439-458.

Zeeden, C., Kaboth, S., Hilgen, F. J., & Laskar, J. (2018). Taner filter settings and automatic correlation optimisation for cyclostratigraphic studies. Computers & geosciences, 119, 18-28.

Cyclicity and variability changes in eastern African paleoclimate during the last ~620 kyrs

Walter Duesing[1], Stefanie Kaboth-Bahr[1], Asfawossen Asrat[2], Andrew S. Cohen[3], Verena Foerster[4], Henry F. Lamb[5,6], Frank Schaebitz[4], Martin H. Trauth1, Finn Viehberg[7,8]

[1]University of Potsdam, Institute of Geosciences, Potsdam, Germany

[2]Addis Ababa University, School of Earth Sciences, Addis Ababa, Ethiopia

[3]University of Arizona, Department of Geosciences, Tucson, USA

[4] University of Cologne, Institute of Geography Education, Cologne, Germany

[5]Aberystwyth University, Department of Geography and Earth Sciences, Aberystwyth, UK, and

[6]University of Dublin, Trinity College, Department of Botany, Dublin, Ireland

[7]University of Cologne, Institute of Geology and Mineralogy, Cologne, Germany

[8]University of Greifswald, Institute of Geography and Geology, Greifswald, Germany

Corresponding author: Walter Düsing (wduesing@uni-potsdam.de)
Key words: African Climate, Times series analysis, Wavelet, Principle Component Analysis, Orbital Forcing

ABSTRACT

There is intensive debate whether and how both long- and short-term climate changes have affected the evolution, dispersal and technological/cultural innovation of our species *Homo sapiens*. To answer this question the analysis of sedimentary archives from Africa that captured the climate variability that hominins encountered are necessary. Here, we present a ~620,000 year climate record from the Chew Bahir Basin (CHB) situated in the southern Ethiopian rift. This paleoclimate record was collected ~90 km from the famous Omo Kibish fossil locality, which represents the first documented appearance of *H. sapiens* in eastern Africa. To decipher past climate variability in eastern Africa, we utilized micro X-ray fluorescence data from the Chew Bahir sediment core and applied a principal component analysis (PCA) to identify the factors controlling sediment composition, representing wet and dry climate states. In a second step we calculated the wavelet power spectrum from the first principal component (PC) to map temporal variations of orbitally-controlled cyclic variations in the sediment composition. Our results show that the long-term wet-dry changes of the eastern African climate recorded in the sediments of the CHB were mainly influenced by changes in orbital eccentricity, with drier and more variable climate occurring at times of minima in the 400 kyr band of the eccentricity cycle. In contrast, increased precipitation truncated with intermediate distinct drying phases paced by orbital precession occurred mainly during eccentricity maxima. The orbital-scale insolation forced humidity changes would have had an impact on the habitat of *H. sapiens* in the region. As an example, the transition from Acheulean to Middle Stone Age (MSA) documented in the Olorgesailie Basin coincides with a pronounced eccentricity minimum, accompanied with reduced moisture availability and repeated abrupt climate transitions. In contrast, during the first documented appearance of *H. sapiens* in eastern Africa climate was humid and less variable.

1 INTRODUCTION

Previous studies suggest that populations of anatomically modern *Homo sapiens* first evolved in Africa (e.g. Hublin et al., 2017, Scerri et al., 2018). Their important evolutionary steps, waves of expansion and technological/cultural innovation have been argued to be closely linked to the climate history of the continent (Castañeda., 2009; Grove, 2015, Potts et al., 2018). Although the influence of climate on modern human evolution is widely accepted, the exact link between climate conditions and human evolution and dispersal is debated, in part because of a lack of temporally and spatially high-resolution climate data, and the even poorer constraints on the paleoanthropological record.

A first order control on the modern climate of tropical Africa is the annual cycle of insolation, which produce monsoonal winds that carry rainfall into the interior of the continent (Nicholson et al., 2017). In areas close to the equator there are two rainy seasons per year due to the occurrence of two insolation maxima, the long rains from March to May and the short rains from October to December (Nicholson et al., 2017). On interannual time scales, the intensity, duration or failure of rainy seasons in eastern Africa also depend on irregularly periodic variation of tropical sea-surface temperatures (SSTs) such as the El Niño-Southern Oscillation (ENSO) and the Indian Ocean Dipole (IOD) (Nicholson, 2017). On the other hand, an eastward shift of the Congo Air Boundary (CAB), caused by an anomalous low-pressure system over West India, may carry additional Atlantic moisture across the Congo Basin to southern Ethiopia, where it may cause a third rainy season (Camberlin and Philippon, 2002). Eastern African climate has been affected in recent decades by several periods of drought, such as in 1998, 2000, 2005 and a trend towards a drier climate since 2009 (Nicholson 2014, 2016). The possible causes of this ongoing process are still largely unknown, one possible explanation being the global increase in greenhouse gases (e.g. Tierney et al., 2015).

On orbital time scales, the amplitude of global insolation is determined by the Milankovich cycles, which include orbital eccentricity (with periods of ~100-400 kyrs), obliquity (with periods of ~40 kyrs) and precession (with periods of ~19-25 kyrs). In the tropics, orbital-scale climate change is mainly governed by precession, controlling the latitudinal migration of the African rain belt (Kutzbach et al., 1982; Berger, 2006; Trauth et al., 2003, 2007). The amplitude of precession, in turn, is modulated by the cyclic (100 and 400 kyr) variations of the eccentricity of the Earth's orbit around the sun (Berger et al., 2006; Trauth et al., 2010). In contrast, the influence of obliquity, the tilt of the Earth's rotational axis, on incoming solar radiation at low-latitudes is small, yet several tropical and subtropical paleoclimate records have indicated the presence of an obliquity signal also at low-latitudes (deMenocal and Ruddiman, 1993; Tiedemann et al., 1994; deMenocal, 2004). To explain this phenomenon several mechanisms have been proposed such as the influence of high-latitude ice sheets on atmospheric circulation (Kutzbach et al., 2020).

Another aspect of tropical African climate has been the proposed presence of half-precession cycles (Berger et al., 2006). At the equator, the solar radiation during the half-yearly highest sun, and hence the intensity of the two rainy seasons, is determined by the March and September insolation. The intensity of this insolation is determined in each case by the precession cycle, but they are shifted by half a cycle against each other, resulting in half-precession cycles in the humidity on orbital time scales (Berger et al., 2006; Trauth et al., 2003).

Superimposed on low-latitude insolation forcing other driving mechanisms have also been proposed to influence tropical African climate on orbital time scales, such as variations in the atmospheric concentration of greenhouse gases (e.g. Johnson et al. 2016), and the expansion and contraction of the continental ice sheets in the high northern latitudes (e.g. Clement et al., 2004). A strong influence of high-latitude glacial-interglacial cycles is suspected for example in Lake Malawi's environmental history and the record of the Limpopo River outflow (Castañeda et al., 2016; Johnson et al., 2016). The relative influence of orbital cycles on the eastern African climate varied over time, just as the cycles of the drivers of climate change itself have changed (Trauth et al., 2009).

Given these uncertainties, and to better understand the role of cyclical climate changes on the habitat of early Homo sapiens and other related hominins, we calculated continuous wavelet transformation of a new ~620 kyr high-resolution sediment core record of past climate change from the CHB and analyzed the resulting power spectra. The CHB lies in the southern Ethiopian Rift, on the southern edge of the Ethiopian Plateau, and close to numerous important fossil hominin and archaeological sites spanning the Mid-Late Pleistocene. The resulting Mid-to Late Pleistocene climate record provides an important new representative archive of environmental history for northeastern Africa.

2 REGIONAL SETTING

The CHB is located in southern Ethiopia in northeastern tropical Africa (Fig. 1). The basin is bordered to the west by the Hammar Range of Precambrian basement rocks and on its eastern flank by the Teltele-Konso Range, which mainly consists of Miocene basaltic lava flows (Foerster et al., 2012, and reference therein). In the North, the catchment area of the CHB encompasses the perennial Segen and Weyto rivers, which drain the southwestern Ethiopian Highlands underlain by Oligocene basalt flows with subordinate rhyolites, trachytes, tuffs and ignimbrites over the Precambrian basement rocks (Davidson, 1983; Foerster et al., 2012).
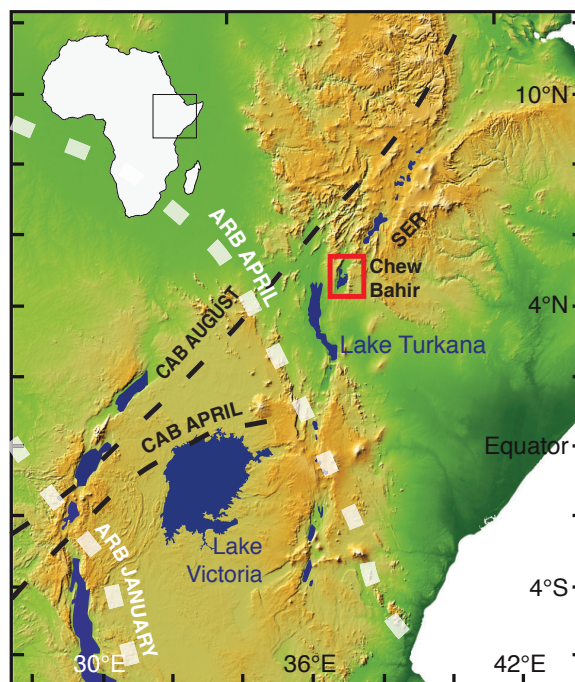

Figure 1
Study area and drill site location. The Chew Bahir basin (CHB), part of the Southern Ethiopian Rift (SER), is marked by a red square. The different seasonal latitudinal positions of the ~ are marked by white dashed lines. The seasonal position of the Congo Air Boundary (CAB) marked by a black dashed line (modified after Foerster et al., 2012).

The climate of the CHB is semi-arid with an annual mean precipitation of 912 mm/year (Fischer et al. accepted), and characterized by heavy biseasonal rainfall, with the „Belg" rainfall from March to May and the longer „Kiremet" rainfall from June to September (Nicholson, 2017). On the highlands northwest of Chew Bahir, precipitation is unimodal with a rainy season from March to November (Segele and Lamb, 2005; Williams and Funk, 2011). Chew Bahir is located in a transition zone between the climate zones of the equatorial tropics and the region of summer monsoons system, in which it is supplied on the one hand with moisture from the Indian Ocean and on the other hand with moisture from the Atlantic Ocean. CHB today is a playa lake, which is episodically flooded during the rainy seasons and then quickly dries up. During pronounced lake level high stands during the latest African Humid Period (AHP, ~15-5 kyr BP; deMenocal et al., 2000) the extensive paleo-lake Chew Bahir reached a maximum of ~50 m (Foerster et al., 2012; Fischer et al., accepted).

3 MATERIALS AND METHODS

The sediment cores used in this study were recovered from the CHB in the southern Ethiopian Rift (4.7612°N, 36.7668°E), The Chew Bahir record is a composite record that has been merged out of duplicate sediment sections of cores, HSPDP-CHB14-2A and 2B, resulting in a 292.87 m long composite core (Foerster et al., submitted.). The chronology of the composite core from CHB derives from the direct dated age model **RRMay2019** (Roberts et al., submitted). This age model combines AMS[14]C dating of molluscs, fish bones and ostracods, optically stimulated luminescence (OSL) dating of quartz and feldspar crystals, as well as $^{40}Ar/^{39}Ar$ dating of (micro)tephra.

All core sections were split lengthwise and analysed in 5 mm resolution using X-ray fluorescence (XRF) scans performed at the Large Lakes Observatory (LLO) of the University of Minnesota Duluth. We excluded all elements from further statistical analysis with poor signal-to-noise ratios and systematic offsets that were related to drilling and measuring artefacts. We used the following elements, that could be shown to relate to environmental variations through time (Foerster et al., in rev.): aluminum (Al), calcium (Ca), iron (Fe), potassium (K), manganese (Mn), sulfur (S), silicon (Si), strontium (Sr), titanium (Ti), and zirconium (Zr).

To investigate linear dependencies between the XRF-based elemental concentrations (XRF counts), we created a correlation matrix using Spearman correlation coefficient and interpreted these with a principal component analysis (PCA).

Prior to the PCA, using the MATLAB function *pca*, the data was normalized. In a second step, we utilized the dominant PC1 from the PCA to resolve temporal changes in its variability by running a sliding window approach determining for each window the distance between the median and the 25% quartile of the PC1. With this approach, we measure the changes of the width of the probability distribution of the PC. To avoid bias from interpolation, we performed the sliding window approach using the fully resolved raw depth data before we applied the age model to the resulting depth series. We used a 40 kyrs window size to cover sufficient data points for a robust analysis, and resolve variability changes beyond 20 kyrs insolation forcing, resulting in 3,376 data points per window. The window step size was set to one, i.e. the window moves by 40 kyrs / 3,376 ≈ 12 yrs with every step.

Lastly, we applied the directly dated age model and calculated a continuous wavelet transformation (CWT) from the evenly-spaced PC1 at a sampling rate of 0.012 kyrs, resulting in a continuous power spectrum, using the MATLAB function *cwt*. We chose Morse as the mother wavelet, and set *time band width* to 120 to increase spectral resolution.

4 RESULTS

The most significant elemental correlations in the CHB XRF record occurred between Al and Si (r=0.82), Ca and Sr (0.82), Ca and Mn (0.76), Fe and Ti (0.73), K and Si (0.57). The most prominent anti-correlations occurred between Ca and Fe (r =–0.55), Sr and Fe (r = -55), Ti and S (r=-0.47), and Zr and Ca (r = -0.41) (Fig. 2).
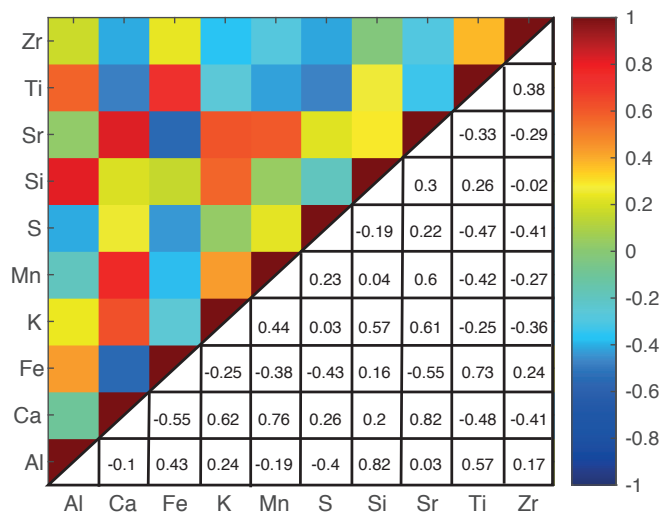

Figure 2
The Spearman correlation matrix of the selected XRF data from the composite Chew Bahir sediment core. One half shows the actual values of the correlation between each element while the other half uses color codes. A strong positive correlation is indicated by reddish colours whilst strong negative correlations are signaled by bluish colours.
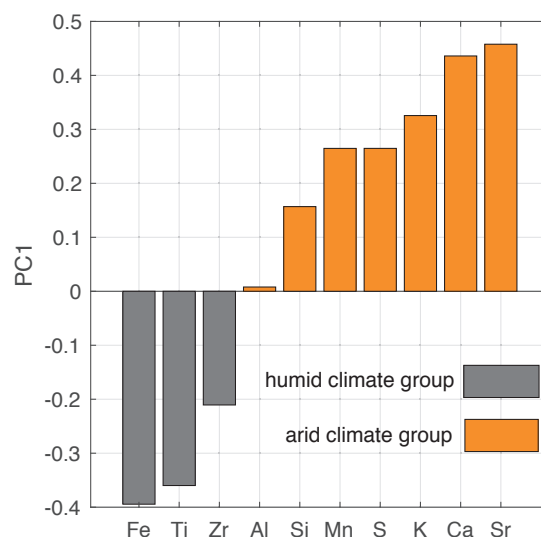
Figure 3
Results of the PCA of the selected XRF elements (see section 2 for more details). We distinguished between an arid climate group represented by Ca, Sr, S, K, Mn, Si, and Al, and a humid climate group consisting of Ti, Fe, Zr, based on the PC1 loads (34.31% of total variance explained).

We used a PCA to unmix and interpret the multidimensional data set. The first PC (PC1) represents 34.31% of the total variance, the second PC (PC2) 24.4%, and the third PC (PC3) 12.08% of the total variance. The total variances of the remaining PCs decrease exponentially. The elements are charged in the first PC in decreasing order as follows: Sr (0.4578), Ca (0.4360), K (0.3256), S (0.2648), Mn (0.2647), Si (0.1569), Al (0.0079), Zr(-0.2106), Ti(-0.3599), Fe (-0.3945) (Fig. 3).

Elements that have previously shown positive pairwise correlations are displayed in PC1 with similar loadings, such as Ca and Sr. Elements that have shown anti-correlation have loadings with opposite signs, such as Fe and Ca. PC1 in the time-domain shows a long-term decreasing trend from 620 kyrs BP to the present with values ranging from −2.5 to 2.5. In addition, several abrupt changes can be observed between 620 and 400 kyrs BP and from 150 kyrs BP to present (Fig. 4A).
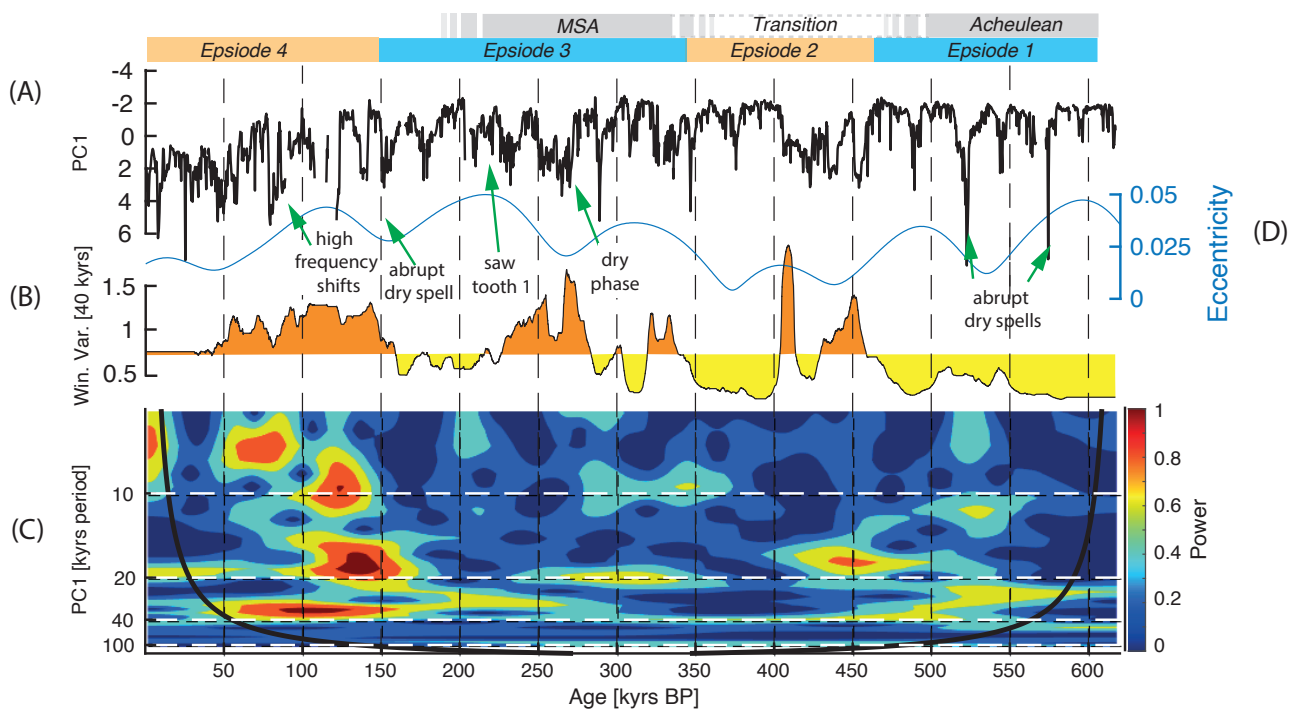

Figure 4
Results of the time-series analysis of the CHB composite core. (A) PC1 (33% of variance explained); positive values indicate increased aridity whilst negative values indicate humid climate conditions. The grey boxes represent the archaeological epochs Middle Stone Age (MSA) and Acheulean after Deino et al., 2018, and a transition between the epochs. (B) The windowed variability analysis using a window size of 40 kyrs; the yellow colour indicate variability values above the median distance between the first quartile and the median of the distribution, while orange colours indicate variability values below the median. (C) Wavelet power spectrum of the PC1 scores. The frequencies of orbital precession (~20 kyrs period), eccentricity (~100 kyrs period), obliquity (~40 kyrs period) and half precession (~10 kyrs) are marked by white dashed lines. The black line marks the cone of influence (COI) of the wavelet power spectrum. Results outside the COI are influenced by edge effects and should therefore be excluded from the interpretation.

We separate the time series into four segments characterized by different measures of central tendency (median) and dispersion (quartiles). Episode 1 (617–430 kyrs BP) represents relative stable, low PC1 values with two extreme shifts to positive values occurring at ~570 and ~525 ka BP. Episode 2 (430–350 kyrs BP) is characterized by initially strong shifts from low to high values and cycles with ~20 kyrs period, followed by a 30-kyrs-long period of increased values, and a fast transition to negative values at 400 kyrs BP. Episode 3 (350–200 kyrs BP) is characterized by negative PC1 values and a periodically recurring, sawtooth-shaped pattern, containing abrupt transitions to positive values followed by slowly declining values, and a 20-kyrs-long phase of positive values occurring from 270–250 kyrs BP. Episode 4 (200–0 kyrs BP), initially starting at relatively low values and an abrupt transition towards positive values at 150 kyrs, declines towards positive values, ending with two sawtooth-shaped patterns, characterized by a slow decrease towards negative values and an abrupt transition to positive values at the end of the record.

The windowed variability analysis of the PC1 record shows a trend of increasing variability towards the youngest time interval (Fig. 4B). Within the first episode the observed variability is low. Episode 2 starts with a strong increase in variability followed by values below the baseline. A drastic increase in variability at 410 kyrs BP can be observed which is followed by variability levels far below the median values. Episode 3 begins with intermediate variability levels plotting slightly above and below the median. At 280 ka BP the variability levels increase again and remain above the median until 240 kyrs BP. The last, youngest episode shows strong variability levels above the median.

The wavelet power spectrum of PC1 reveals significant cycles of 100, 40-30, 20-30, and 10 kyr periodicities (Fig. 4C). However, the presence of these cycles is transient. During Episode 1 we find increased power within the 40, 20 and ~10 kyr periods, and a weakly expressed 100 kyr cycle. In contrast, Episode 2 is characterized by weakly expressed ~100 and ~40 kyr cycles. During Episode 3 cycles with periods of ~100, ~40, ~20, and ~10 kyrs are again well expressed. Throughout the time interval covered by Episode 3, the ~40 kyr cycle shortens or is successively replaced by a 25 kyr and subsequently by a 10 kyr cycle. During Episode 4 we find strong ~35 kyr, ~20 kyrs and 8–10 kyrs cycles. The ~20 kyr cycle is very pronounced at the beginning of Episode 4 but its expression deteriorates and is subsequently replaced by 35 kyrs cycles towards the present.

5 DISCUSSION
5.1 ESTABLISHING PC1 AS WET-DRY INDEX

The results of the Spearman correlation matrix and the PCA reveal that the elements Ca and Sr, as well as S are highly correlated, and align with K, and Mn, all of which share all positive correlation values. We argue that the variances of the elements Ca, Sr, and S within the PC1 potentially relate to evaporation processes. Carbonates with high Ca-Sr replacement in the crystal lattice ($CaCO_3$, $SrCO_3$), as well as evaporite minerals such as gypsum ($CaSO_4$), and polyhalites ($K_2Ca_2Mg[SO_4]_4 \cdot 2H_2O$), can form when the evaporation rate of the water body is greater than the total water inflow, leaving a concentrated mineral residue (Schreiber and Tabakh, 2000). We argue that with the lowering of the lake level under more arid climate conditions the salinity of paleolake Chew Bahir increased, and consequently led to the formation of the evaporite succession, which could explain the simultaneous occurrence of Ca (carbonates, sulfates), Sr (carbonates with high Sr content), S (sulfate) (Schreiber and Tabakh, 2000). In fact, Ca in the CHB was deposited primarily as endogenic calcite and as biogenic calcite i.e., ostracod valves or mollusc shells (Viehberg et al., 2018). Additionally early diagenetic carbonate nodule formation in the CHB during dry playa lake conditions, comprising high Mg-/high Mn-calcite (Viehberg et al., 2018) could explain the simultaneous high Mn concentrations and aid our interpretation of Ca as an evaporation indicator. Similarly as Ca concentration has been used has aridity indicator in eastern African lakes Malawi and Tana (Johnson et al., 2016, Lamb et al., 2018). Ca, Sr, S and Mn ions required for the formation of the evaporites were most likely transported into paleolake Chew Bahir in solution, and derived from the chemical weathering of feldspathic gneisses, marbles, granulites and basalts of the Chew Bahir catchment (Foerster et al., 2012). In addition, Ca, Sr, S and Mn are also correlated to K which primarily originates from the weathering of quartzo-feldspathic gneisses and the associated micaceous granites of the surrounding Hammar range (Foerster et al., 2012). The contributions of K within the sediment largely represents the degree of authigenic illitization of smectites (Viehberg et al. 2018). This process including a progressive potassium-fixation is strongly depended on high temperatures, but also on alkalinity of pore water and lake water (Foerster et al., 2012; 2018; submitted, Viehberg et al. 2018) which subsequently is governed by the lake volume and a low precipitation/evaporation ratio (Foerster et al., 2018, Viehberg et al. 2018). Hence, this relationship closely ties changes in K also to aridity.

The elements Si and Mn, are also positive correlated with the evaporitic elements (Ca, Sr, S) as well as K. A process involving Mn enrichment in sediments is related to oxygenation of the lakes water. In general, arid periods are characterized by an oxygen-rich, unstratified, well-mixed water body during low lake levels. Under these conditions Mn precipitates as Mn-Oxides and accumulates in the lake sediments (Davison, 1993; Friedl et al., 1997). Hence, conditions with elevated Mn can also be interpreted as arid climate conditions. In contrast to Mn, the association of Si with evaporitic elements and K remains ambiguous. Generally, we argue that Si is closely associated with the abundance of

silicates, especially weathered feldspars, the influx being connected to activity of the extensive alluvial fans proximal to the basin-margin drill site (Foerster et al., 2012). The activity of the alluvial fans in CHB occurs mainly in dry phases, when the sediments accumulated there are not reclaimed by vegetation, but are flushed into the basin during sporadically heavy rainfall episodes (Foerster et al., 2012). The very low charge of 0.0079 within PC1 of Al indicates that changes in Al concentration in combination with the other included elements do not contribute much to the variability expressed within PC1. Based on these findings we argue that more positive PC1 loadings are indicative of more evaporitic conditions resulting from a more arid climate.

The abundance of elements with negative PC1 loadings such as Fe, Ti, and Zr may also have climatic significance. Dissolved iron (Fe^{2+}) and iron hydroxide ($Fe^{3+}OOH$) could originate from the catchment areas at the upper eastern edge of the CHB, from the Teltele plateau and from the north-eastern part of the catchment area, where volcanic rocks are exposed to weathering (Foerster et al., 2012). Similarly, Ti (which strongly correlates with Fe), as well as Zr are also products of the weathering of gneisses and granites in the catchment area (Foerster et al., 2012; Francus et al., 2013; Davies et al., 2015; Wagner et al., 2018; Viehberg et al., 2018, Foerster et al., 2020). Ti has been identified in the CHB to represent detrital input in a previous publication studying XRF sediment compositions (Viehberg et al., 2018). Even though, it seems plausible that vegetation cover reduces basin wide erosion rates leading to a reduction in detrital input, as observed in other eastern African regions (Acosta et al., 2015), we argue that high concentrations of Fe, Ti and Zr represent relative humid climate conditions that produced increased chemical weathering and enhanced fluvial input, due to an increase in stream power of the basins tributaries from the north-eastern catchment into the CHB.

Another process that might have also played a role during humid climate conditions, in particular explaining increased Fe concentrations, is reduction processes at the bottom-water-sediment boundary. In this scenario, high lake levels result in a well stratified lake with poor ventilation of the bottom water. The organic material is consumed by anaerobic bacteria in the surface sediment, releasing hydrogen sulphide (H_2S), which in turn reacts with the dissolved Fe to form pyrite (FeS_2) (Davidson, 1983; Nealson and Saffarini, 1994; O'Sullivan and Reynolds, 2005).

5.2 TIME SERIES ANALYSIS

Based on our previous findings we argue that the PC1 separates elements that dominantly respond to processes linked to either arid (positive PC1 scores) or humid (negative scores) conditions in the Chew Bahir and its catchment. Therefore, we believe that the PC1 can be used as a robust climate proxy during the last 620 kyrs for this part of northeastern Africa. After converting the PC1 scores from the depth domain to the time domain, we identified distinct humid episodes between 620–450 kyrs BP and 400–150 kyrs BP. Longer (~20 kyrs) arid phases occur mainly from 450–400 kyrs BP, 270–250 kyrs BP, and 100–0 kyrs BP. We recognised that the long-term trend of PC1 follows the 400 kyrs cycle of eccentricity, with arid phases occurring dominantly during eccentricity minima and more humid phases during eccentricity maxima. The eccentricity of the Earth's orbit modulates the amplitude of the precession cycle, which in turn determines the insolation budget of the tropics; intensifying and reducing monsoon strength every 19–25 kyrs (e.g. Kutzbach and Otto-Bliesner 1982; Berger, 2006; Trauth et al., 2007). The correlation between the long-term trend of eccentricity suggests that long-term changes in precipitation at CHB are linked to insolation changes. These findings agree with previous studies that argued the dominance of insolation forcing for eastern African climate change (Trauth et al., 2007, 2009; Kutzbach et al., 2020). The relationship between eccentricity and precession is also clearly demonstrated by the increased presence of cycles with a 19–25 kyrs periodicity during the ~400 kyrs eccentricity maximum between 325 kyrs BP and 110 kyrs BP. In contrast, we find that the presence of precession cycles during both 400 kyr eccentricity minima (between 450 kyrs BP and 350 kyrs BP) is strongly reduced.

In addition, our results show the presence of the ~10 kyrs cycle during increased eccentricity. This period, usually interpreted as a semi-precessional cycle, may be an indicator for a bimodal annual precipitation distribution (Berger 2006, Trauth 2003). Due to its proximity to the equator (4°N), the CHB is located in an area where two rainy seasons occur, as maximum insolation levels are reached twice a year, creating a boreal winter rainy season from March to May

and a longer summer rainy season from June to September (Nicholson, 2017). In turn, times of precession maxima experience increased seasonality, as has been demonstrated for the African Humid Period (AHP) (Rohling et al., 2002). The increased amplitude of precession caused by high eccentricity might have thus led to an increase in the contrast between the rainy and dry seasons. This relationship could explain the preferred occurrence of half precession cycles during eccentricity maxima rather than during minima.

Despite the limitations of the applied age model our findings clearly show that throughout the last ~620 kyrs orbitally-controlled insolation variations controlled wet-dry cycles in the CHB. This stands in strong contrast to other analysis of wet-dry indices from different tropical and subtropical sites in eastern and western Africa which postulated a possible linkage between humidity changes in tropical Africa and atmospheric CO_2 levels, high-latitudinal changes, as well as the waning and waxing of global ice sheets (Bloemendal and deMenocal, 1989; deMenocal et al., 1993; Tiedemann et al., 1994; Johnson et al., 2016; Castañeda et al. 2016; Miller et al. 2016; Owen et al., 2018; Liu et al., 2018). Although we do not observe a clear glacial-interglacial cyclicity in the PC1 our results highlight a possible ~40 kyrs obliquity cycle in the wavelet power spectrum which has been used as a finger print of the influence of high-latitude mechanisms on low-latitude climate despite the fact that obliquity induced insolation changes in the tropics are minimal (e.g. Castañeda et al., 2016).

We find that the 40 kyr signal at CHB is best expressed during increased eccentricity and high precession amplitudes at CHB between 550–450 kyrs BP, and between 150–50 kyrs BP. Thus, this spatiotemporal pattern actually argues against a high-latitude origin of the 40 kyr cycle at CHB as it was demonstrated that the influence of obliquity in the tropics is strongest during phases of low eccentricity, when insolation forcing is low (Kuechler et al., 2018). Another possible explanation could be that the 40 kyr cycle is an artefact from the partly low-resolved age model or a harmonic from the precession cycle which could explain its simultaneous occurrence with increased precession amplitude conditions. Alternatively, it has been previously proposed that the tropical 40 kyrs cycle relates to the inter-tropical insolation gradient during boreal summer as shown for the formation of the Mediterranean sapropels (Mantsis et al., 2014; Bosman et al., 2015). By adding equatorial insolation of the rainy seasons in December and June and dividing it by the sum of the equatorial insolation during the dry seasons in September and March, it is indeed possible to create a ~40 kyrs cycle using equatorial insolation only (Fig. 5). The comparison between the inter-tropical insolation gradient and our PC1 shows that in both cases the presence of ~40 kyrs and ~10 kyr cycles are best expressed during eccentricity maxima. This temporal coherence suggests that the climate of the CHB during eccentricity maxima was strongly modified by the equatorially influenced precipitation/evaporation ratio rather than changes to the global CO_2 budget or ice volume.

In addition, we attempted to detect changes in the variability of the PC1, and thus performed a windowed variability analysis. The results show a relative increase in variability from ~620 kyrs to the present which is in phase with the long-term aridity trend over the same time interval. Superimposed on this long-term trend is the increased signal variability at transitions from high to low eccentricity between 450–350 kyrs BP and vice versa. This increased signal variability most likely translates into frequent and abrupt climate transitions. In contrast, the variabilities during the eccentricity maximum at ~220 kyrs BP was in comparison strongly decreased which suggests a relatively stable climate system against high humidity background conditions.

The climate history presented here shows that during high eccentricity a strongly insolation-driven climate system prevailed, whereas during low eccentricity the climate was more strongly affected by short-term variability changes. The short-term environmental changes reflected in the increased variability might have influenced the evolution, technological advances and expansion of early modern humans who lived in this region (Foerster et al. in rev. Schaebitz et al in rev.). In the Olorgesaille Basin, the temporal changes in the occurrence of stone tools, which bracket the transition from Acheulean to Middle Stone Age (MSA) technologies at between 499–320 kyrs (Deino et al., 2018; Potts et al., 2018), could potentially correlate to the marked transition from a rather stable climate with less variability to a climate with increased variability in the CHB. In contrast, the much more stable climatic conditions of 250 – 150 kyrs BP during episode 3 were characterized by first waves of dispersal of *H. sapiens* to Europe and the Levant (Hershkovitz et al., 2018). The climatically stable conditions may have led to larger populations of humans, which increased the probability of successful expansion beyond the limits of the African continent. During the period of Omo I and II before 198±14 kyrs BP (McDougall et al., 2005), climatic conditions in Chew Bahir also indicate a humid climate.

6 CONCLUSION

We have established a new wet-dry climate proxy for the CHB, designed to capture climatic cyclicity and variability changes. Long term climate changes are seemingly driven by orbital eccentricity, with low eccentricity preconditioning increased aridity and a highly variable climate in eastern Africa whereas during high eccentricity the climate is less variable and wetter. Continuous frequency analyses showed the occurrence of precession and half precession cycles during increased eccentricity, pointing towards an insolation-driven climate in eastern Africa. During low eccentricity intervals we observe abrupt climate shifts, which are not readily explainable by insolation changes, and may point towards the sensitivity of eastern Africa climate during these time intervals to other driving mechanisms, such as atmospheric CO_2 levels. We conclude that populations of early anatomically modern humans are more likely to have experienced climatic stress during episodes of low eccentricity, associated with dry and high variability climate conditions, which may have led to technological innovation, such as the transition from the Acheulean to the Middle Stone Age.

7 ACKNOWLEDGEMENTS

REFERENCES

Armitage, S. J., Bristow, C. S., & Drake, N. A. (2015). West African monsoon dynamics inferred from abrupt fluctuations of Lake Mega-Chad. Proceedings of the National Academy of Sciences, 112(28), 8543-8548.

Bosmans, J. H. C., Hilgen, F. J., Tuenter, E., & Lourens, L. J. (2015). Obliquity forcing of low-latitude climate. Climate of the Past, 11(10), 1335-1346.

Bloemendal, J., & Demenocal, P. (1989). Evidence for a change in the periodicity of tropical climate cycles at 2.4 Myr from whole-core magnetic susceptibility measurements. Nature, 342(6252), 897-900.

Breunig, P., Neumann, K. & Van Neer, W. New research on the Holocene settlement and environment of the Chad Basin in Nigeria. African Archaeol Rev 13, 111–145 (1996). https://doi.org/10.1007/BF01956304

Camberlin, P., & Philippon, N. (2002). The East African March–May rainy season: Associated atmospheric dynamics and predictability over the 1968–97 period. Journal of Climate, 15(9), 1002-1019.

Castañeda IS, Mulitza S, Schefuß E, Santos RAL, Damste JSS, Schouten S (2009). Wet phases in the Sahara/Sahel region and human expansion patterns in North Africa. Proc Natl Acad Sci 106:1–5. https://doi.org/10.1073/pnas.0905771106

Castañeda, I. S., Caley, T., Dupont, L., Kim, J. H., Malaizé, B., & Schouten, S. (2016). Middle to Late Pleistocene vegetation and climate change in subtropical southern East Africa. Earth and Planetary Science Letters, 450, 306-316.

Clemens, S. C., Holbourn, A., Kubota, Y., Lee, K. E., Liu, Z., Chen, G., ... & Fox-Kemper, B. (2018). Precession-band variance missing from East Asian monsoon runoff. Nature communications, 9(1), 1-12.

Clement, A., Hall, A., and Broccoli, A.: The importance of precessional signals in the tropical climate, Climate Dynamics, 22, 327–341, 2004.

Davidson, A. (1983). The Omo River project: reconnaissance geology and geochemistry of parts of Ilubabor, Kefa, Gemu Gofa and Sidamo. Ethiopian Institute of Geological Surveys Bulletin, 2, 1–89.

Davies, S.J., Lamb, H.F., Roberts, S.J., 2015, Micro-XRF Core Scanning in Palaeolimnology: Recent Developments, in: Croudace, I.W., Rothwell, R.G. (eds.), 2015, Micro-XRF Studies of Sediment Cores, Springer.

Davison, W. (1993). Iron and manganese in lakes. Earth-Science Reviews, 34(2), 119-163.

Deino, A. L., Behrensmeyer, A. K., Brooks, A. S., Yellen, J. E., Sharp, W. D., & Potts, R. (2018). Chronology of the Acheulean to Middle Stone Age transition in eastern Africa. Science, 360(6384), 95-98.

Demenocal, P. B., Ruddiman, W. F., & Pokras, E. M. (1993). Influences of high-and low-latitude processes on African terrestrial climate: Pleistocene eolian records from equatorial Atlantic Ocean Drilling Program site 663. Paleoceanography, 8(2), 209-242

Demenocal, P., Ortiz, J., Guilderson, T., Adkins, J., Sarnthein, M., Baker, L., & Yarusinsky, M. (2000). Abrupt onset and termination of the African Humid Period:: rapid climate responses to gradual insolation forcing. Quaternary science reviews, 19(1-5), 347-361.

Peter, B. D. (2004). African climate change and faunal evolution during the Pliocene–Pleistocene. Earth and Planetary Science Letters, 220(1-2), 3-24

Diro, G. T., Grimes, D. I. F., & Black, E. (2011). Teleconnections between Ethiopian summer rainfall and sea surface temperature: part II. Seasonal forecasting. Climate Dynamics, 37(1-2), 121-131.

Foerster, V., Junginger, A., Langkamp, O., Gebru, T., Asrat, A., Umer, M., ... & Trauth, M. H. (2012). Climatic change recorded in the sediments of the Chew Bahir basin, southern Ethiopia, during the last 45,000 years. Quaternary International, 274, 25-37.

Foerster, V., Vogelsang, R., Junginger, A., Asrat, A., Lamb, H. F., Schaebitz, F., & Trauth, M. H. (2015). Environmental change and human occupation of southern Ethiopia and northern Kenya during the last 20,000 years. Quaternary Science Reviews, 129, 333-340.

Foerster, V., Deocampo, D. M., Asrat, A., Günter, C., Junginger, A., Krämer, K. H., ... & Trauth, M. H. (2018). Towards an understanding of climate proxy formation in the Chew Bahir basin, southern Ethiopian Rift. Palaeogeography, Palaeoclimatology, Palaeoecology, 501, 111-123.

Foerster et al., 2020 in prep.

Francus et al., (2013). Varved sediments of Lake Yoa (Ounianga Kebir, Chad) reveal progressive drying of the Sahara during the last 6100 years. Sedimentology (2013) 60, 911–934.

Friedl, G., Wehrli, B., Manceau, A., (1997). Solid phases in the cycling of manganese in eutro- phic lakes: new insights from EXAFS spectroscopy. Geochimica et Cosmochimica Acta 61, 275–290.

Grant, K.M., et al., (2017), A 3 million year index for North African humidity/aridity and the implication of potential pan-African Humid periods. Quaternary Science Reviews, 171, 100–118, doi: 10.1016/j.quascirev.2017.07.005.

Hershkovitz, I., Weber, G. W., Quam, R., Duval, M., Grün, R., Kinsley, L., ... & Arsuaga, J. L. (2018). The earliest modern humans outside Africa. Science, 359(6374), 456-459.

Grove, M. (2015). Palaeoclimates, plasticity, and the early dispersal of Homo sapiens. Quaternary International, 369, 17-37.

Hublin, Jean-Jacques, et al. „New fossils from Jebel Irhoud, Morocco and the pan-African origin of Homo sapiens." Nature 546.7657 (2017). 289-292.

Johnson, T. C., Werne, J. P., Brown, E. T., Abbott, A., Berke, M., Steinman, B. A., ... & Scholz, C. A. (2016). A progressively wetter climate in southern East Africa over the past 1.3 million years. Nature, 537(7619), 220-224.

Kuechler, R. R., Dupont, L. M., & Schefuß, E. (2018). Hybrid insolation forcing of Pliocene monsoon dynamics in West Africa. Climate of the Past, 14(1).

Kuper, R., & Kröpelin, S. (2006). Climate-controlled Holocene occupation in the Sahara: motor of Africa's evolution. Science, 313(5788), 803-807.

Kutzbach, J. E., & Otto-Bliesner, B. L. (1982). The sensitivity of the African-Asian monsoonal climate to orbital parameter changes for 9000 years BP in a low-resolution general circulation model. Journal of the Atmospheric Sciences, 39(6), 1177-1188.

Kutzbach, J. E., Guan, J., He, F., Cohen, A. S., Orland, I. J., & Chen, G. (2020). African climate response to orbital and glacial forcing in 140,000-y simulation with implications for early modern human environments. Proceedings of the National Academy of Sciences, 117(5), 2255-2264.

Lamb, H. F., Bates, C. R., Bryant, C. L., Davies, S. J., Huws, D. G., Marshall, M. H., ... & Toland, H. (2018). 150,000-year palaeoclimate record from northern Ethiopia supports early, multiple dispersals of modern humans from Africa. Scientific reports, 8(1), 1-7.

Larrasoana, J.C., Roberts, A.P., Rohling, E.J., Winklhofer, M., Wehausen, R., (2003). Three million years of monsoon variability over the northern Sahara. Climate Dynamics 21, 689–698, doi:10.1007/s00382-003-0355-z.

Larrasoaña, J. C., Roberts, A. P., & Rohling, E. J. (2013). Dynamics of green Sahara periods and their role in hominin evolution. PloS one, 8(10).

Laskar, J., Gastineau, M., Joutel, F., Robutel, P., Levrard, B., Correia, A., (2004). A long term numerical solution for the insolation quantities of Earth. Astronomy and Astrophysics, 428, 261-285, available online at http://vo.imcce.fr/insola/earth/online/earth/online/.

Liu, X., Rendle-Bühring, R., & Henrich, R. (2018). High-and low-latitude forcing of the East African climate since the LGM: Inferred from the elemental composition of marine sediments off Tanzania. Quaternary Science Reviews, 196, 124-136.

Mantsis, D. F., Lintner, B. R., Broccoli, A. J., Erb, M. P., Clement, A. C., & Park, H. S. (2014). The response of large-scale circulation to obliquity-induced changes in meridional heating gradients. Journal of climate, 27(14), 5504-5516.

Marshall M, Schlolaut G, Nakagawa T, Lamb H, Brauer A, Staff R, Ramsey C, Tarasov P, Go- tanda K, Haraguchi T, Yokoyama Y, Yonenobu H, Tada R (2012). A novel approach to varve counting using µXRF and X-radiography in combination with thin-section microscopy, applied to the Late Glacial chronology from Lake Suigetsu, Japan. Quat Geochronol 13:70–80. doi:10.1016/j.quageo.2012.06.002

McDougall, I., Brown, F. H., & Fleagle, J. G. (2005). Stratigraphic placement and age of modern humans from Kibish, Ethiopia. Nature, 433(7027), 733-736.

Miller, C. S., Gosling, W. D., Kemp, D. B., Coe, A. L., & Gilmour, I. (2016). Drivers of ecosystem and climate change in tropical West Africa over the past 540 000 years. Journal of Quaternary Science, 31(7), 671-677.

Nealson, K. H., & Saffarini, D. (1994). Iron and manganese in anaerobic respiration: environmental significance, physiology, and regulation. Annual review of microbiology, 48(1), 311-343.

Nicholson, S. E. (2014). A detailed look at the recent drought situation in the Greater Horn of Africa. Journal of Arid Environments, 103, 71-79.

Nicholson, S. E. (2016). An analysis of recent rainfall conditions in eastern Africa. International Journal of Climatology, 36(1), 526-532.

Nicholson, S. E. (2017). Climate and climatic variability of rainfall over eastern Africa. Reviews of Geophysics, 55(3), 590-635.

O'Sullivan, P. E. (2005). The lakes handbook: Vol. 2: Lake restoration and rehabilitation. Blackwell Publishing.

Owen, R.B., et al., (2018). Progressive aridification in East Africa over the last half million years and implications for human evolution, PNAS, doi:10.1073/pnas.1801357115, 1–6.

Potts, R., Behrensmeyer, A. K., Faith, J. T., Tryon, C. A., Brooks, A. S., Yellen, J. E., ... & Levin, N. E. (2018). Environmental dynamics during the onset of the Middle Stone Age in eastern Africa. Science, 360(6384), 86-90.

Rohling, E. J., Cane, T. R., Cooke, S., Sprovieri, M., Bouloubassi, I., Emeis, K. C., ... & Kemp, A. E. S. (2002). African monsoon variability during the previous interglacial maximum. Earth and Planetary Science Letters, 202(1), 61-75

Rossignol-Strick, M. (1985). Mediterranean Quaternary sapropels, an immediate response of the African monsoon to variation of insolation. Palaeogeography, palaeoclimatology, palaeoecology, 49(3-4), 237-263.

Scerri, E. M., Thomas, M. G., Manica, A., Gunz, P., Stock, J. T., Stringer, C., ... & d'Errico, F. (2018). Did our species evolve in subdivided populations across Africa, and why does it matter?. Trends in ecology & evolution, 33(8), 582-594.

Schreiber, B. C., & Tabakh, M. E. (2000). Deposition and early alteration of evaporites. Sedimentology, 47, 215-238.

Schuster, M., Roquin, C., Duringer, P., Brunet, M., Caugy, M., Fontugne, M., ... & Ghienne, J. F. (2005). Holocene lake Mega-Chad palaeoshorelines from space. Quaternary Science Reviews, 24(16-17), 1821-1827

Segele, Z. T., & Lamb, P. J. (2005). Characterization and variability of Kiremt rainy season over Ethiopia. Meteorology and Atmospheric Physics, 89(1-4), 153-180.

Shanahan, T. M., Overpeck, J. T., Hubeny, J. B., King, J., Hu, F. S., Hughen, K., ... & Black, J. (2008). Scanning micro-X-ray fluorescence elemental mapping: A new tool for the study of laminated sediment records. Geochemistry, Geophysics, Geosystems, 9(2).

Storch, T. A., & Dunham, V. L. (1986). IRON-MEDIATED CHANGES IN THE GROWTH OF LAKE ERIE PHYTOPLANKTON AND AXENIC ALGAL CULTURES 1. Journal of phycology, 22(2), 109-117.

Tierney, J. E., Abram, N. J., Anchukaitis, K. J., Evans, M. N., Giry, C., Kilbourne, K. H., ... & Zinke, J. (2015). Tropical sea surface temperatures for the past four centuries reconstructed from coral archives. Paleoceanography, 30(3), 226-252.

Tierney, J. E., Pausata, F. S., & deMenocal, P. B. (2017). Rainfall regimes of the Green Sahara. Science advances, 3(1), e1601503.

Acosta, V. T., Schildgen, T. F., Clarke, B. A., Scherler, D., Bookhagen, B., Wittmann, H., ... & Strecker, M. R. (2015). Effect of vegetation cover on millennial-scale landscape denudation rates in East Africa. Lithosphere, 7(4), 408-420.

Trauth, M. H., Maslin, M. A., Deino, A. L., Strecker, M. R., Bergner, A. G., & Dühnforth, M. (2007). High-and low-latitude forcing of Plio-Pleistocene East African climate and human evolution. Journal of Human Evolution, 53(5), 475-486

Trauth, M. H., Deino, A. L., Bergner, A. G., & Strecker, M. R. (2003). East African climate change and orbital forcing during the last 175 kyr BP. Earth and Planetary Science Letters, 206(3-4), 297-313.

Trauth, M. H., Maslin, M. A., Deino, A. L., Strecker, M. R., Bergner, A. G., & Dühnforth, M. (2007). High-and low-latitude forcing of Plio-Pleistocene East African climate and human evolution. Journal of Human Evolution, 53(5), 475-486.

Trauth, M. H., Larrasoana, J. C., & Mudelsee, M. (2009). Trends, rhythms and events in Plio-Pleistocene African climate. Quaternary Science Reviews, 28(5-6), 399-411.

Trauth, M. H., Maslin, M. A., Deino, A. L., Junginger, A., Lesoloyia, M., Odada, E. O., ... & Tiedemann, R. (2010). Human evolution in a variable environment: the amplifier lakes of Eastern Africa. Quaternary Science Reviews, 29(23-24), 2981-2988.

Viehberg, F.A., Just, J., Dean, J.R., Wagner, B., Franz, S.O., Klasen, N., Kleinen, T., Ludwig, P., Asrat, A., Lamb, H., Leng, M., Rethemeyer, J., Milodowski, A.E., Claussen, M., Schäbitz, F., (2018). Environmental change during MIS4 and MIS 3 opened corridors in the Horn of Africa for Homo sapiens expansion, Quaternary Science Reviews, 202, 139-153, doi:10.1016/j.quascirev.2018.09.008.

Viste, E., & Sorteberg, A. (2013). The effect of moisture transport variability on Ethiopian summer precipitation. International journal of climatology, 33(15), 3106-3123.

Wagner, Bernd, et al. (2018), 'Holocene rainfall runoff in the central Ethiopian highlands and evolution of the River Nile drainage system as revealed from a sediment record from Lake Dendi', Global and Planetary Change, 163 29-43.

Wainwright, C. M., Marsham, J. H., Keane, R. J., Rowell, D. P., Finney, D. L., Black, E., & Allan, R. P. (2019). 'Eastern African Paradox'rainfall decline due to shorter not less intense Long Rains. npj Climate and Atmospheric Science, 2(1), 1-9.

Williams, A.P., Funk, C., (2011). A westward extension of the warm pool leads to a westward extension of the Walker circulation, drying eastern Africa. Climate Dynamics. http://dx.doi.org/10.1007/s00382-010-0984-y.

Recurring types of variability and transitions in the ~620 kyr record of climate change from the Chew Bahir basin, southern Ethiopia

Martin H. Trauth*[1], Asfawossen Asrat[2], Andrew S. Cohen[3], Walter Duesing[1], Verena Foerster[4], Helen Roberts[5], Stefanie Kaboth-Bahr[1], Hauke Kraemer[1,6], Henry F. Lamb[6], Norbert Marwan[6], Mark A. Maslin[7], Frank Schaebitz[4]

[1] University of Potsdam, Institute of Geosciences, Potsdam, Germany

[2] Addis Ababa University, School of Earth Sciences, Addis Ababa, Ethiopia

[3] University of Arizona, Department of Geosciences, Tucson, USA

[4] University of Cologne, Institute of Geography Education, Cologne, Germany

[5] Aberystwyth University, Department of Geography and Earth Sciences, Aberystwyth, UK

[6] Potsdam Institute for Climate Impact Research, Potsdam, Germany

[7] University College London, Geography Department, London, UK

*Corresponding Author: email trauth@uni-potsdam.de, Tel. +49 331 977 5810, Fax +49 331 977 5700

ABSTRACT

The Chew Bahir Drilling Project (CBDP) aims to test possible linkages between climate and hominin evolution in Africa through the analysis of sediment cores that have recorded environmental changes in the Chew Bahir basin (CHB). In this statistical project we used recurrence plots (RPs) together with a recurrence quantification analysis (RQA) to distinguish two types of variability and transitions in the Chew Bahir aridity record and compare them with the ODP 967 wetness index from the eastern Mediterranean. The first type of variability is one of slow variations with cycles of ~20 kyr, reminiscent of the Earth's precession cycle, and subharmonics of this orbital cycle. In addition to these cyclical wet-dry fluctuations in the area, extreme events often occur, i.e. short wet or dry episodes, lasting for several centuries or even millennia, and rapid transitions between these wet and dry episodes. The second type of variability is characterized by relatively low variation on orbital time scales, but significant century-millennium-scale variations with progressively increasing frequencies. Within this type of variability there are extremely fast transitions between dry and wet within a few decades or years, in contrast to those within type 1 with transitions over several hundreds of years. Type 1 variability probably reflects the influence of precessional forcing in the lower latitudes at times with maximum values of the long (400 kyr) eccentricity cycle of the Earth's orbit around the sun, with the tendency towards extreme events. Type 2 variability seems to be linked with minimum values of this cycle. There is no systematic correlation between Type 1 or Type 2 variability with atmospheric CO_2 concentration. The different types of variability and the transitions between those types had important effects on the availability of water, and could have transformed eastern Africa's environment considerably, which would have had important implications for the shaping of the habitat of *H. sapiens* and the direct ancestors of this species.

INTRODUCTION

Some hypotheses about the relationship of climate and human evolution suggest that episodes of increased climate variability (e.g. Potts, 1996, 2013, Maslin and Trauth, 2009) or prominent transitions (e.g. Vrba, 1985, 1993) may have enhanced rates of speciation, dispersal and technological innovation. Examples on long time scales are the termination of the permanent El Nino/establishment of the modern Walker/Hadley circulation between 3.5–2.0 Ma, possibly linked to the closure of the Indonesian sea way (Cane and Molnar, 2001; Ravelo et al., 2004; Trauth et al., 2009), and the intensification of the Northern Hemisphere Glaciation at 2.75 Ma (e.g., Bonnefille, 2010; Trauth et al., 2009), both being subject to lively discussions during the last four decades (Vrba 1985, 1983; deMenocal 1995, 2004; Brovkin and Claussen, 2008; Kröpelin et al., 2008a,b; Trauth et al., 2005, 2009). As the most recent example of a major climate shift in the tropics, in particular in Africa, the termination of the African Humid Period (AHP, ~15–5 kyr BP) has also been intensely investigated, in particular the extent to which it was abrupt or gradual (deMenocal et al., 2000; Kuper and Kröpelin, 2006; Tierney and deMenocal, 2013; Trauth et al., 2018), which is important for potential migration scenarios within and across the Sahara and cultural transformations (Kuper and Kröpelin, 2006).

Revived by these debates, statistical methods have recently been used to make quantitative statements about the degree of variability and character of transitions. According to their analysis, the most important transition during the long-term trend towards a more arid climate was at ~1.9 Ma, at about the time of the establishment of the modern Walker/Hadley circulation (Ravelo et al., 2004; Trauth et al., 2009), and not, as suggested earlier by deMenocal (1995, 2004) during the intensification of the Northern Hemisphere Glaciation (INHG). Similarly, the termination of the AHP at ~5 kyr BP was tested for its relative abruptness comparing observed and theoretical probability distributions of paleoclimate time series from multiple locations in and around Africa (Tierney and deMenocal, 2013). According to their analysis, the wet-dry transition occurred within centuries, which agrees with the results of Trauth et al. (2018) using a change point analysis to determine a ~880 yr interval within which this important climate shift occurred.

More sophisticated approaches to classifying variability and transitions were used by Trauth et al. (2019) with recurrence plots together with a recurrence quantification analysis on six short (<17 m) sediment cores collected during the Chew Bahir Drilling Project (CBDP) from the Chew Bahir basin (CHB) in southern Ethiopia, reaching back to ~47 kyr BP. Recurrence plots (RPs) are graphic displays of recurring states in the environmental system (Eckmann et al. 1987; Marwan et al. 2007). Quantitative descriptions (measures of complexity) have been developed to complement visual inspection of recurrence plots (RPs) and for recurrence quantification analysis (RQA) (e.g. Zbilut and Webber 1992; Marwan et al. 2007; Marwan 2008). Trauth et al. (2019) presented and discussed results from such an RQA on the environmental record of the CHB short cores. The different types of variability and transitions in these records were classified to shed light on our understanding of the response of the biosphere to climate change, particularly the response of humans in the area.

One of the most interesting transitions examined with the RP/RQA was once again the termination of the African Humid period (Trauth et al., 2018, 2019). The rapid (~880 yr) change of climate in response to a relatively modest change in forcing appears to be typical of tipping points in complex systems such as the Chew Bahir basin (Lenton et al., 2008; Ditlevsen and Johnsen, 2010). If this is the case then 14 dry events at the end of the AHP, each of them 20–80 yrs long and recurring every 160±40 yrs as documented in the Chew Bahir cores could represent precursors of an imminent tipping point which, if properly interpreted, would allow predictions to be made of future climate change in the Chew Bahir basin (Trauth et al., 2018, 2019). Compared to the low-frequency cyclicity of climate variability before and after the termination of the AHP, this type of cyclicity occurs on time scales equivalent to a few human generations. In other words, it is very likely (albeit speculative) that people were conscious of these changes and adapted their lifestyles to the consequent changes in water and food availability. A deeper analysis of our data is however required to understand whether the wet-dry climate transition in the area was due to a saddle-node bifurcation in the structural stability of the climate, or whether it was induced by a stochastic fluctuation (Lenton et al., 2008; Ditlevsen and Johnsen, 2010).

Here we present a RP/RQA-based analysis of two long (~290 m) cores collected in 2014 in the Chew Bahir basin (4°45'40.55"N 36°46'0.85"E), spanning the time from ~620 kyr to present. The Chew Bahir basin is situated in a transition zone between the Main Ethiopian Rift and the Omo-Turkana basin, adjacent to the Lower Omo Basin,

where some of the oldest known fossils of anatomically modern humans were found (McDougall et al., 2005). According to recent archeological findings, the adjoining highlands in the area may have been a refuge area for groups of *H. sapiens* during times of climatic stress (Ambrose et al., 1998; Brandt and Hildebrand, 2005; Vogelsang et al., 2018; Ossendorf et al., 2019).

We compare the Chew Bahir record of environmental change during the past ~620 kyr with the wetness index for the wider northeastern Saharan/North Africa from ODP Site 967 (Grant et al., 2017). The site was drilled during ODP Leg 160 in the eastern Mediterranean (34°N, 34°E, 2,252 m water depth), where Saharan and North African dust and Nile riverine input are the primary contributors of sediment. The ODP 967 wetness index is a combined run-off and dust signal in a single metric, reflecting the effects of both strengthening/northward migration (increased run-off) and weakening/southward retreat (increased dust) of the northern and northeastern African monsoon (Grant et al., 2017). The catchment of the Nile River with its two tributaries, the White Nile and the Blue Nile, extends from southeastern Africa to parts of the northwestern Ethiopian highlands. In the very wet phases, the Lakes Abaya-Chamo-Chew Bahir-Turkana system with its connecting rivers drained into the Nile catchment (Junginger et al., 2013). Therefore, both the upper Nile catchment and the Chew Bahir catchments are in spatial proximity and are most likely exposed to similar climate fluctuations and their causes. Humid conditions, recorded in both ODP 967 and CHB cores, could indicate the regional significance of a wet phase. Similar patterns in the types of variability and transitions could be indicative of the effect of a similar climate dynamic.

As a contribution to the reconstruction of environmental conditions for eastern Africa based on long terrestrial sediment records, our CHB record is firstly used to classify variability down core in order to identify recurring episodes of stable wet or dry, of cyclic or more complex but predictable variability, and of chaotic/random variability. Second, we classified types of transitions, including episodes with no change, linear/gradual shifts with different rates of change, as well as different types of rapid transitions such as tipping points. As soon as a classification of variability and transitions is available, one can discuss possible reasons for the similarity, e.g. similar boundary conditions such as global ice volume, local insolation, atmospheric CO_2 levels and ocean sea-surface temperatures. Finally, we hypothesize which types of variability and transitions may have affected the biosphere including hominins.

MATERIALS AND METHODS

THE MIDDLE PLEISTOCENE–HOLOCENE PALEOCLIMATE RECORD OF THE CHEW BAHIR BASIN

The sediment cores described herein were collected in the western part of the Chew Bahir basin in the southern Ethiopian Rift (4.1–6.3°N, 36.5–38.1°E, ~500 above sea level; Fig. 1). Chew Bahir is a tectonic basin, separated from the Lower Omo basin to the west by the Hammar Range, which is the source of most of the sediments at the coring site. This range to the west and the highlands to the north and north-east consist of Late Proterozoic granitic and mafic gneisses, whereas the eastern part of the catchment is dominated by Miocene basaltic lava flows. Oligocene basalt flows with subordinate rhyolites, trachytes, tuffs and ignimbrites cover the Precambrian basement units in the distal north-eastern, northern, and north-western parts of the catchment (Moore and Davidson, 1978; Davidson, 1983). Being a closed basin, Chew Bahir forms a terminal sink for weathering products from its 32,400 km² catchment.

The present-day climate in eastern and northeastern Africa is influenced by a number of major air streams and convergence zones, with their effects superimposed on regional influences associated with topography, large lakes, and the oceans (Nicholson, 2017). Rainfall in the Chew Bahir catchment is associated with the passage of the tropical rain belt, resulting in a strongly bimodal annual cycle. Most of the moisture reaching the Ethiopian highlands in June–August comes from the Mediterranean and Red Sea (55%), and from the Indian Ocean (31%) (Viste and Sorteberg, 2013). Short-term (annual to decadal) fluctuations in the intensity of precipitation relate to E-W adjustments in the zonal Walker circulation associated with the El Niño-Southern Oscillation (ENSO) and the Indian Ocean Dipole (IOD), possibly as a direct response to sea-surface temperature (SST) variations in the Indian and Atlantic Oceans, which are in turn affected by the ENSO and the IOD (Nicholson, 2017).

The paleoclimate of Chew Bahir was first reconstructed using six short cores, up to ~17 m long and collectively spanning ~47 kyr, which were collected in 2009–2010 (Foerster et al., 2012, 2015; Trauth et al., 2015, 2018, 2019). In the context of the Hominin Sites and Paleolakes Drilling Project (HSPDP) to drill at key fossil hominin and archeo-logical sites (Cohen et al., 2016; Campisano et al., 2017), we collected parallel, duplicate cores: HSPDP-CHB14 2A (4°45'40.32"N 36°46'0.48"E) and 2B (4°45'40.68"N 36°46'1.20"E) in the Chew Bahir basin, 266.38 and 278.58 m long, respectively, in Nov–Dec 2014 (Foerster et al., in prep; Schäbitz et al., in prep). A 292.87 m long composite core of the Chew Bahir Drilling Project (CBDP) with more than 90% recovery was created from the duplicate cores.
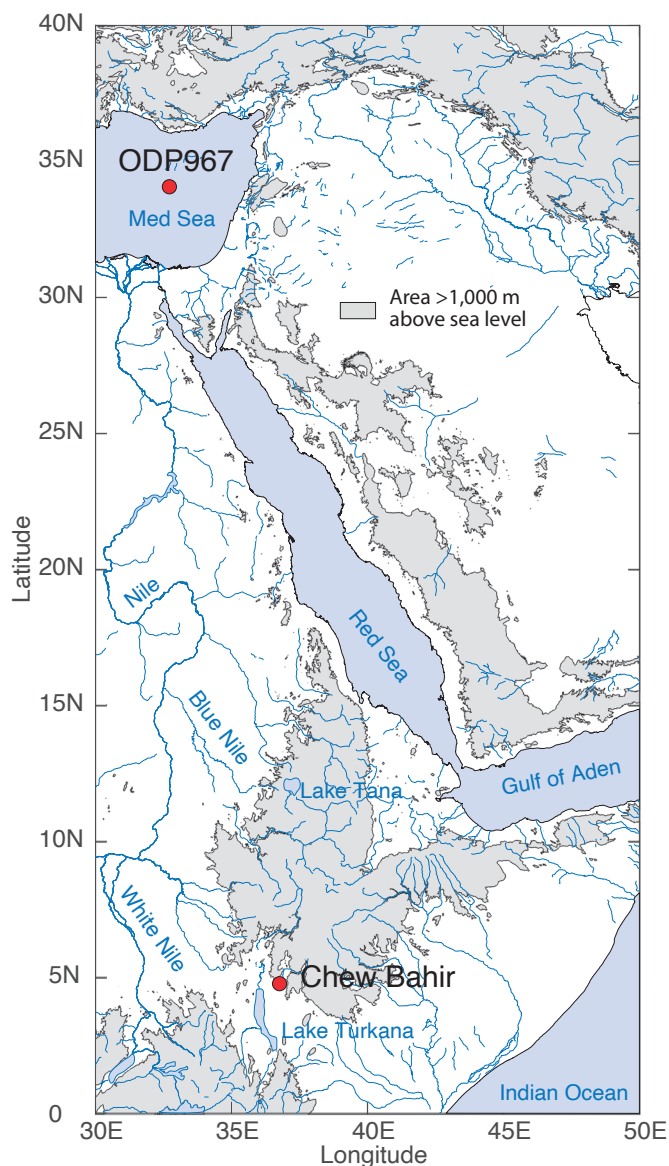
Figure 1

Map of northeastern Africa and adjacent areas showing the location of the Chew Bahir basin (4°45'40.55"N 36°46'0.85"E, ~500 m above sea level), the ODP Leg 160 Site 967 in the eastern Mediterranean Sea (34°4'6"N 32°43'31"E, ~2,254 m water depth), and the river Nile with its two tributaries the White and Blue Niles connecting both regions. Coastline and river polygons from the Global Self-consistent, Hierarchical, High-resolution Geography data set (GSHHG) (Wessel and Smith 1996). Topography from the 1 arc-minute global relief model of the Earth's surface (ETOPO1) (Amante and Eakins 2009).

The composite core was developed by merging the two parallel cores 2A and 2B by core-to-core correlation using MSCL logs, core images, lithological description and XRF data sets. Radiometric age constraints were based on ^{14}C dating of ostracodes, optically stimulated luminescence (OSL) dating of fine-silt sized quartz grains, and single-crys-tal total-fusion (SCTF) ^{40}Ar/^{39}Ar dating of feldspars from tuffaceous zones within the core. In addition, a volcanic ash layer identified in the core has been correlated on the basis of major and minor element geochemistry to a dated tephra found in the outcrop at Konso, in the southern Main Ethiopian Rift, namely the Silver Tuff (Roberts et al., in prep.). The ages generated are stratigraphically consistent, and Bayesian age-depth modeling incorporating ^{14}C, OSL and ^{40}Ar/^{39}Ar ages, and tephrochronological data has been used to build an age model for the Chew Bahir cores (age model **RRMay2019**, Roberts et al., in prep.).

We analyzed the potassium (K) concentrations of the sediment, determined by micro X-ray fluorescence (μXRF) scanning which was previously shown to be a reliable proxy for aridity in the Chew Bahir basin (Foerster et al., 2012; Trauth et al., 2015, 2018). The most likely process linking climate with K concentrations is the authigenic illitization of smectites during episodes of higher alkalinity and salinity in the closed-basin lake resulting from a drier climate (Foerster et al., 2018). After processing the μXRF data to remove coring and scanning artifacts, the data were corrected for outliers and jumps, before we applied various types of normalizations and standardizations of the data (Foerster et al., in prep.).

PRINCIPLES OF RECURRENCE PLOTS (RP) AND RECURRENCE QUANTIFICATION ANALYSIS (RQA)

As a first approximation we can describe the Chew Bahir paleolake as a complex system composed of interacting components, such as the water body, the sediment below the bottom of the lake, and the organisms living in the lake and its surroundings (Marwan et al., 2007; Trauth et al., 2019). This multi-dimensional system is characterized by many state variables such as precipitation (with more rain causing higher weathering and erosion of rocks in the catchment, and hence more potassium (K) washed into the lake), evaporation (causing higher K concentrations in the sediment through authigenic K fixation in smectites, Foerster et al., 2018) and wind speed (blowing higher quantities of K-rich particles from the catchment into the lake).

One way to unfold the dynamics of the multi-dimensional system from one-dimensional time series is time-delay embedding, whereby the dynamic characteristics of the system are preserved (Packard et al., 1980). The reason for a complete reconstruction of the system from a single variable is that the information about the system and its state variables is contained in the one-dimensional time series. The embedding of the time series in a three-dimensional (m=3) phase space, for example, means that three successive values with a temporal distance τ (or tau) are represented as a point in a three-dimensional coordinate system (the phase space) (Iwanski and Bradley, 1998; Webber and Zbilut, 2005; Marwan et al., 2007). The phase space portrait then displays the embedded time series of observations as a trajectory in the phase space, i.e. the phase space trajectory represents the path over which the system's state evolves through time. The reconstruction of the phase space (from embedding) is not exactly the same as the original phase space (the true variables describing the lake), but its topological properties are preserved, provided that the embedding dimension is sufficiently large (Packard et al., 1980; Takens, 1981).

A common feature of dynamical systems is the property of recurrence (Webber and Zbilut, 2005). Patterns of recurring states of a system reflect typical system characteristics whose description contributes significantly to understanding the system's dynamics. A recurrence plot (RP), introduced by Eckmann et al. (1987), is a graphical display of such recurring states of the system, calculated from the distance (e.g. Euclidean) between all pairs of observations, within a cutoff limit (Marwan et al., 2007). To complement the visual inspection of recurrence plots, measures of complexity were introduced for their quantitative description to perform the recurrence quantification analysis (RQA) (e.g., Marwan et al., 2007; Marwan, 2008). Among these, a selection of measures based on the recurrence density, others based on diagonal and vertical lines typically appearing in recurrence plots are very useful for studying the behavior of the Chew Bahir lake system. As an example of measurements based on the recurrence density, the *recurrence rate (RR)* is the density of black dots in the recurrence plot. This measure simply describes the probability of recurring states of the system in a particular time period.

Diagonal lines in recurrence plots typically occur when a segment of the trajectory runs almost (e.g. within a given tolerance) in parallel to another segment, representing an earlier episode of the system's history in the phase space, for a certain period of time. Diagonal lines in recurrence plots are therefore diagnostic of cyclic behavior in time series, and in contrast to the time series analysis using Fourier-based methods, this cyclic behavior is not restricted to sinusoidal structures when using recurrence plots. Since cyclic behavior can be used to predict future conditions from the present and past, the ratio of the recurrence points that form diagonal structures (of a minimum length) to all recurrence points is therefore a measure for *determinism* (*DET*, or predictability) of the

system. Vertical lines in recurrence plots typically correspond to periods where the trajectory remains in the same phase space region (Marwan et al., 2007; Marwan 2010). Vertical lines are therefore diagnostic of episodes when the state of the system does not change or changes very slowly. In other words, the system seems to be trapped in a specific state for some time, which is typical for irregular transitions between different types of dynamics.
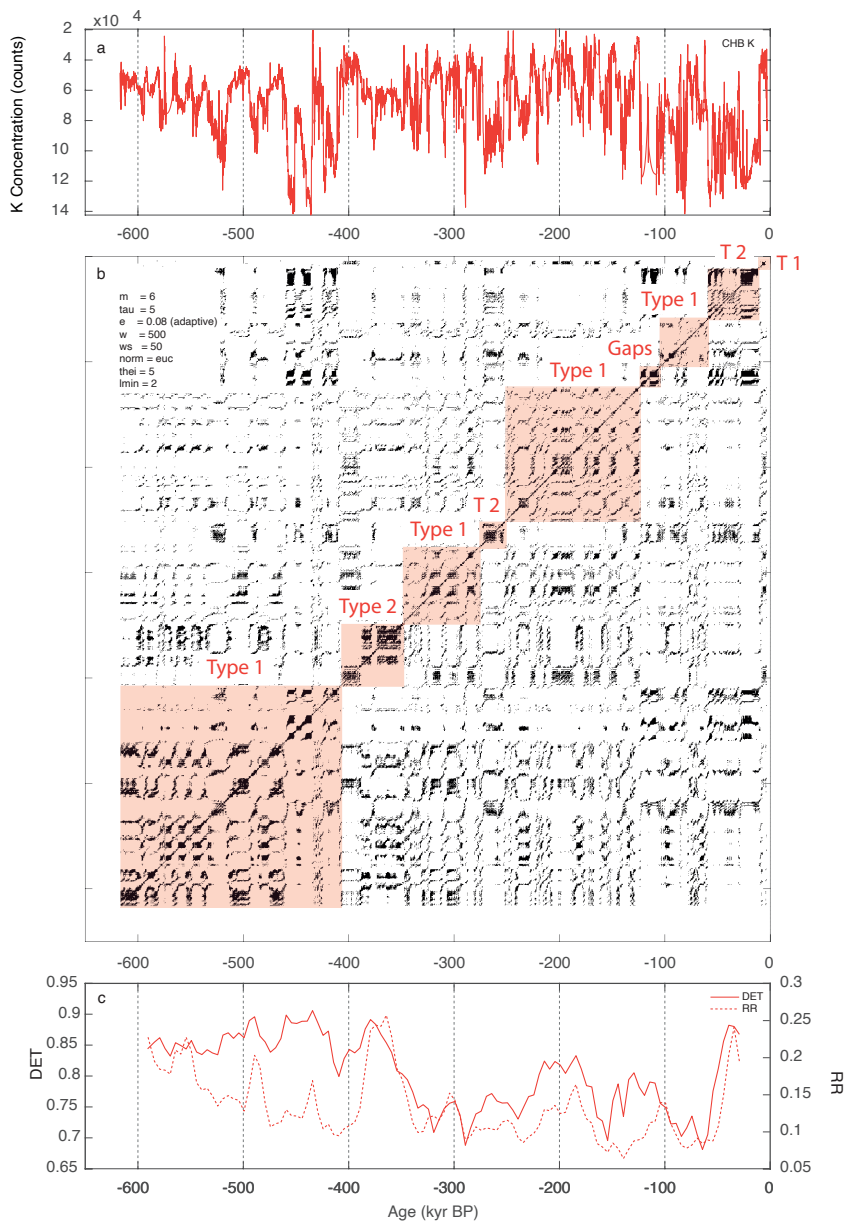

Figure 2
Recurrence plot (RP) and recurrence quantification analysis (RQA) measures of the potassium (K) concentrations of the sediment in Chew Bahir, southern Ethiopia: the time series according to age model (3) (upper panel), the recurrence plot (middle panel) and the RQA measures of moving windows (lower panel). Embedding parameters m=embedding dimension, tau=time delay, e=threshold, w=window size, ws=window moving steps, norm=vector norm, thei=size of Theiler window, lmin=minimum line length, RQA measures RR=recurrence rate and DET=determinism. See the methods section for a detailed description of the embedding parameters and RQA measures.

RESULTS

Recurrence plots (RPs), together with a recurrence quantification analysis (RQA), were used to describe different types of environmental variability and transitions in the Chew Bahir (Fig. 2 and Suppl. Fig. 1–6). From the available RQA measures we have selected RR and DET because they describe important properties of the dynamic Chew Bahir system but are very descriptive compared to other RQA measures (Marwan et al., 2007; Trauth et al., 2019). We compare the RPs and RQA measures of the Chew Bahir record with those of the wetness index for the wider northeastern Saharan/North African record from ODP 967 (Grant et al., 2017) (Fig. 3).

We have used K as a proxy for aridity, as the dominant process linking climate with K concentrations is the authigenic illitization of smectites during episodes of higher alkalinity and salinity in the closed-basin lake resulting from a drier climate (Foerster et al., 2018). For the analysis of the ~620 kyr record the K record was embedded in a phase space with a dimension of m=6 and temporal distances of τ=5, equivalent to 5×0.1 kyr=0.5 kyr, where 0.1 kyr is the resolution of the time series following a piecewise cubic Hermite interpolating polynomial (Frisch and Carlson, 1980). We use the window size w=500 and the step size ws=50 data points of the moving window to calculate the RQA measures (Fig. 2). The size w of the window corresponds to 500x0.1 kyr=50 kyr and the step size is 50x0.1 kyr=5 kyr. To compare the RP/RQA based dynamics in the Chew Bahir record of aridity with the wetness index of ODP 967, we interpolated the marine record to the same time axis, used an embedding dimension of m=2 and temporal distances of τ=2 to create the RPs and the same window size to calculate the RQA measures (Fig. 3). We use a slightly lower embedding dimension m and $τ$ because the signal-to-noise ratio of the ODP 967 moisture index seems to be lower than that of the K record of Chew Bahir, as experiments with different values for m and $τ$ showed. Similarities in the texture of the recurrence plots of both proxy records show that the embedding provides comparable results with these values. However, even identical embedding parameters would not lead to significantly different results.
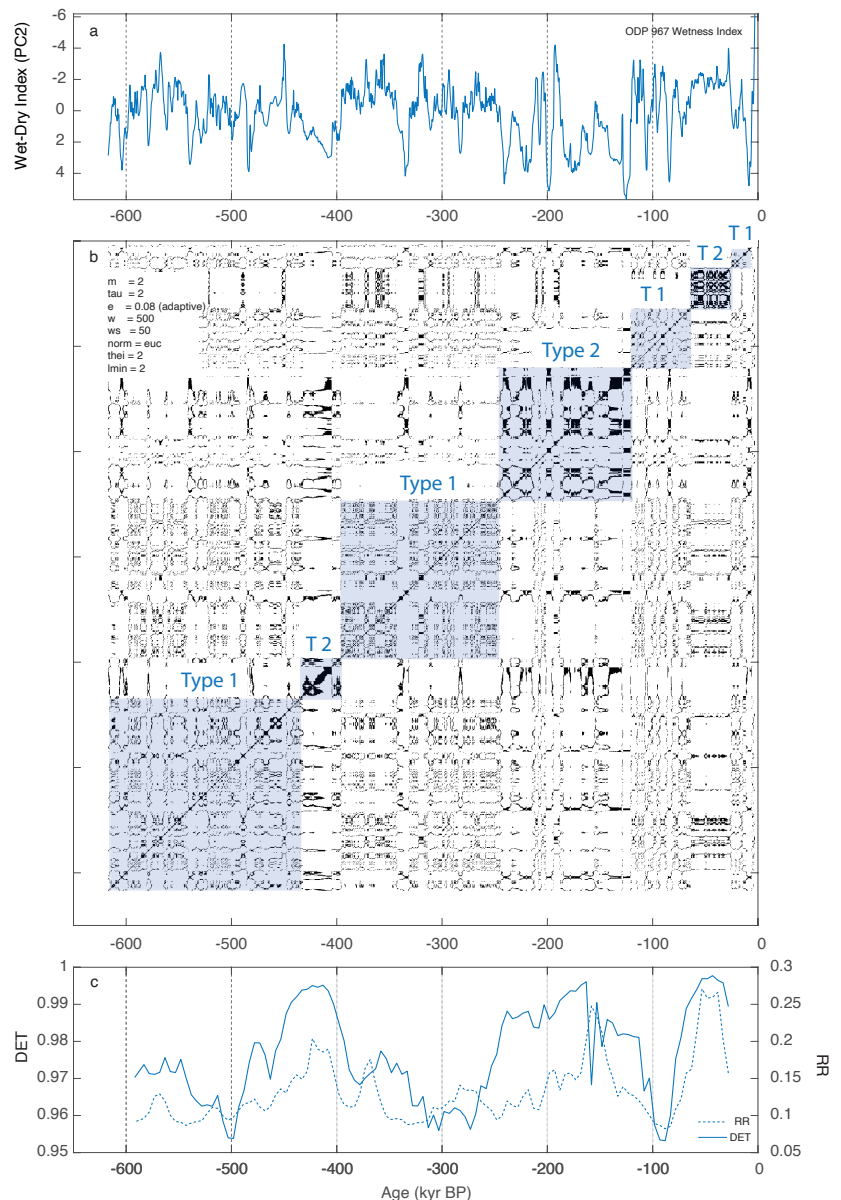

Figure 3
Recurrence plot (RP) and recurrence quantification analysis (RQA) measures of the high resolution (0.015 kyr) potassium (K) concentrations of the sediment in Chew Bahir in southern Ethiopia between 348 and 272 kyr BP: the time series according to age model (3) (upper panel), the recurrence plot (middle panel) and the RQA measures (a) RR and (b) DET of moving windows (lower panel). For abbreviations, see caption of Supplementary Figure 1. See the methods section for a detailed description of the embedding parameters and RQA measures.

The first series of four clusters of recurrence points occurs between **620 and 410 kyr BP** in the Chew Bahir record, with the largest cluster between 620 and 462 kyr BP, then three smaller clusters at 456–435, 435–425, and 425–410 kyr BP (Fig. 2). These clusters are characterized by a series of *s*-shaped diagonal lines, overlain by blocks with high recurrence rates, which mark 1–2 kyr long episodes of relative stability. The diagonal lines are interrupted by white vertical lines, reflecting a series of wet-dry episodes recurring with approximately half-precession cyclicity, initiated and terminated by relatively abrupt transitions. As the result of the cyclic recurrence of wet and dry conditions, the DET values are relatively high (~0.85), whereas RR has moderate, but declining values (0.2–0.1). Two extremely dry episodes centered at ~455 and ~438 kyr BP are reflected in two clusters of recurrence points and high DET values (~0.9) within the 458–436 kyr BP interval, separated by white vertical lines and slightly lower DET values. Zooming into the interval between 620 and 410 kyr BP with higher (0.025 kyr) resolution the diagonal lines become blurred and the RP is dominated by many small (<10 kyr) blocks that are connected by black horizontal and vertical lines (Suppl. Fig. 1). This suggests that, at time scales of <10 kyr, the system oscillates between shorter stable states, each 1–5 kyr long, with rapid transitions between them. Within the blocks, we observe diagonal lines indicating high-frequency (<1 kyr) cyclicities. In the ODP 967 wetness index we find a similar type of variability in the time before 435 kyr, although in comparison diagonal structures are much less pronounced or even absent (Fig. 3). The RR values are at similar values to those in the Chew Bahir, except for a significant anticorrelation at ~420 kyr (Fig. 4). The DET values are generally lower but increase after ~500 kyr BP up to similar values as in the Chew Bahir record.

This interval ends with a rapid transition at ~410 kyr BP from dry to wet conditions. This transition is followed by two dense clusters of recurrence points between **410 and 348 kyr BP**, indicating episodes of a stable wet climate with extreme RR and DET values, interrupted by short dry episode at ~375 kyr BP (Fig. 2). The two clusters reflect relatively stable humid conditions, with the humidity level in the first cluster being higher than in the second cluster and hence the two clusters are separated by a transition towards a slightly less wet climate at around 390 kyr BP. The second cluster is interrupted by a distinctive dry event at around 376 kyr BP. Interestingly, both clusters show an irregular pattern of diagonal lines, partly slightly curved, suggesting recurrent dry events, but with slightly variable cyclicity. Zooming into the interval between 410 and 348 kyr BP with higher (0.025 kyr) resolution we observe blurred diagonal lines with 1–2 kyr distances, indicating a weak cyclicity on millennium time scales even within the otherwise quite stable wet episodes (Suppl. Fig. 2). The interval between 410 and 348 kyr BP is terminated by gradual (~10 kyr) transition towards slightly more humid conditions after ~348 kyr BP. The ODP 967 wetness index indicates similar wet conditions during this episode, but with almost no form of variability (Fig. 3). As a consequence, the RR values are relatively high (~0.2) whereas the DET values are also at high level but relatively low compared to before and after the event (~0.97).

The next cluster of recurrence points between **348 and 272 kyr BP** is marked by a series of blocks with weak internal structure and separated by white vertical lines (Fig. 2). This structure reflects a series of relatively stable wet conditions, interrupted by several thousand-year long dry episodes, some of which are bounded by relatively rapid transitions from wet to dry and back. The occasional appearance of diagonal lines, though rarely parallel to the main diagonal, indicates weak cyclic behavior. Within this interval the RR values are constantly low (~0.1–0.15), whereas the DET values start at high values (~0.97) and decline until about 320 kyr BP before they remain at low values (~0.7). Zooming into the interval between 348 and 272 kyr BP with higher (0.025 kyr) resolution confirms the observation of small blocks connected with black horizontal and vertical lines in the RP, as a result of a rapid change between relatively stable dry and wet conditions, with the exception of the block between 330 and 327 kyr BP. This block is merely the result of a gap that was closed by interpolation (Suppl. Fig. 3). The blocks themselves have little internal structure, with the exception of very weak diagonal lines with a spacing of <1 kyr. The interval between 348 and 272 kyr BP is terminated by a very rapid transition from wet to dry conditions at ~272 kyr. The ODP 967 wetness index shows a similar variability type during this episode, with DET values declining parallel to those of the Chew Bahir (Fig. 3).

Between **272 and 252 kyr BP**, we observe another dense cluster of recurrence points (Fig. 2). The internal structure of this block is reminiscent of similar structures of the clusters at ~400 and ~360 kyr BP, whereas the system state based on the difference in the DET values does not support this conclusion. The interval again shows diagonal lines, this time very clearly curved, with slight convergence with respect to the main diagonal. As a result of the distinct cyclicity, the RR and DET values are at moderate levels, with DET at a local maximum. This pattern suggests that the

climate was relatively stable, but fluctuations between humid and dry occur in cycles. These changes occur more and more frequently over time, until the climate finally quickly changes to generally humid conditions at around 228 kyr BP. Zooming into the interval between 272 and 252 kyr BP with higher (0.025 kyr) resolution reveals that the curved diagonal lines are rather a sequence of short, laterally offset diagonal pieces. In the younger section of the block, the diagonal lines disappear (Suppl. Fig. 4). Considering the course of the time series it can be seen that the diagonals reflect increasingly shorter wet phases, and until after about 236 kyr quite stable, relatively dry conditions prevail in the Chew Bahir. The ODP 967 wetness index shows similar climate fluctuations during this episode, but these are too unclear to be described with a different type of variability (Fig. 3). The RR values are low, similar to those in the Chew Bahir, whereas the DET values are possibly at a local maximum, again similar to Chew Bahir.

The RPs of the following episode between **252 and 122 kyr BP** show a blocky pattern with complex internal structure and many white vertical lines (Fig. 2). Again, we observe short diagonal lines, causing slightly higher DET values. This episode mirrors the earlier ones between 620 and 410 kyr BP and between 348 and 272 kyr BP, whereby in the second interval also the state of the environmental system also recurs. The episode is unfortunately followed by two gaps due to core loss between **~122 and 107 kyr BP**, which are filled by the interpolation with curves, so we get a high RR at this point that we cannot interpret (Fig. 2). Zooming into the interval between 252 and 122 kyr BP
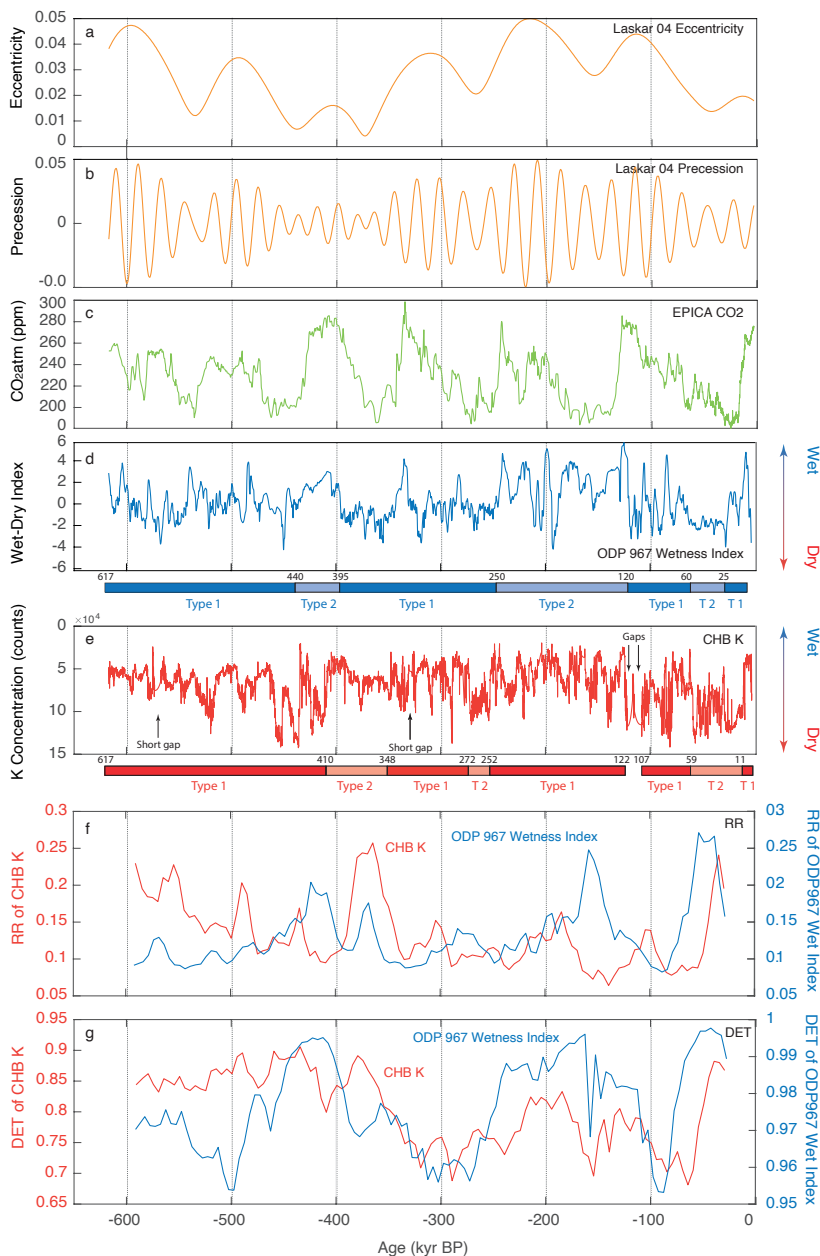

Figure 4

Recurrence plot (RP) and recurrence quantification analysis (RQA) measures of the high resolution (0.015 kyr) potassium (K) concentrations of the sediment in Chew Bahir in southern Ethiopia between 272 and 252 kyr BP: the time series according to age model (3) (upper panel), the recurrence plot (middle panel) and the RQA measures (a) RR and (b) DET of moving windows (lower panel). For abbreviations, see caption of Supplementary Figure 1. See the methods section for a detailed description of the embedding parameters and RQA measures.

with higher (0.025 kyr) resolution reveals many small blocks surrounded by *s*-shaped curved structures rather than continuous diagonal lines which mark short (<5 kyr) wet phases which begin and end gradually (Suppl. Fig. 5). Besides that, we observe longer (5–10 kyr) wet episodes with rapid onset and termination, internally structured by converging diagonals, structurally similar to the ones in the interval between 272 and 252 kyr BP, but with a different system state based on the RR and DET values. This interval is terminated by ~5 kyr long gaps after 122 kyr BP. During this episode, the ODP 967 wetness index shows a type of variability that is more similar to the episode of *435 and 370 kyr BP*, rather than the one after *370 kyr BP* (Fig. 3). The course of the RR values is similar to the one of Chew Bahir in the first half of the interval, but seems to be anticorrelated in the second half. The DET values show a very similar pattern to those of the Chew Bahir, although at lower levels (~0.98–0.99 at ODP 967, ~0.75–0.8 at Chew Bahir). The increasing DET values at the beginning of the interval are about 20 kyr later for ODP 967, then they vary in a very similar way even including a minimum at about 160 kyr, and then decline at the end of this interval (Fig. 4).

Between **107 and 59 kyr BP**, we find a very complex phase with fast changes between stable humid, very variable humid and very dry conditions, each separated by fast transitions (Fig. 2 and Suppl. Fig. 6). After a very dramatic transition we observe very regular climate fluctuations between **~59 kyr BP and about 11 kyr BP**, when it became relatively stable dry. This interval is again characterized by a cluster of dense recurrence points, slightly converging diagonal lines which indicate increasing recurrence rates (i.e. shorter wet-dry cycles), before we see a black block of recurrence points as the result of very stable dry conditions. The **last ~11 kyr** are characterized by very wet conditions, interrupted with a short, about ~1 kyr long dry intervals and terminated by a transition towards a dry climate. The distinct cyclic alternation of wet and dry conditions, each of which are ~5 kyr long, results in high RR and DET values. The last ~47 kyr BP are preserved at higher resolution in the short cores from the same basin, also examined with the method of RP/RQA (Trauth et al., 2019). Here we found very similar patterns as on the long time scale, with alternating appearances of blocky structures and diagonal lines, with different transitions between episodes. The ODP 967 wetness index here shows a similar variability with long-periodic, high amplitude fluctuations between wet and dry between **~120 and 60 kyr BP**, followed by an episode without such variations (Fig. 3). The time interval between **60 and 25 kyr BP** is relatively stable, as compared with the high-frequency variability observed in the Chew Bahir, before we observe two long wet cycles, out of which the second one is also seen in the Chew Bahir record.

DISCUSSION

We applied a detailed analysis of the RPs together with a RQA to distinguish between different types of climate variability, and transitions in the Chew Bahir basin (Trauth et al. 2018) (Fig. 4). Here, climate is inferred from our key proxy, the potassium concentration of the sediment representing the relative aridity in the Chew Bahir Basin (Foerster et al., 2018). Our statistical analyses herein are a contribution to an accurate picture of environmental change in eastern Africa during the last ~620 kyr and thereby provide a quantitative, high resolution climatic component useful for investigating human-climate interactions. The fossil and archaeological record of eastern Africa is still too limited to draw definitive conclusions with respect to current hypotheses on the relationship between climate and evolutionary patterns in humans and other animals. However, our results do allow for some initial comparisons and hypotheses (e.g. Stringer and Galway-Witham, 2017; Scerri et al., 2018; Galyway-Witham et al., 2019).

Our analysis clearly shows a number of different types of variability in the K record that overlay a long-term trend towards greater aridity and variability (Figs. 2 and 4). These types of variability are separated by transitions, which are of varying types of durations and structures. Many of these types, both variability and transitions, occur multiple times during the last ~620 kyr, so it is interesting to investigate them more closely to see if they are characteristic of the Chew Bahir Basin or possibly occur even beyond the region. In addition, it is important to examine whether these types are linked to certain regional or global boundary conditions (e.g. global ice volume, atmospheric CO_2 levels, ocean sea-surface temperatures) (Fig. 4).

We observe two basic types of variability that do not mix, but each form a series of variants. The first type of variability, occurring at 620–410 kyr BP, 348–272 kyr BP, 252–122 kyr BP, and (after a period with no data) 107–59 kyr BP, are slow variations with cycles of ~20 kyr and subharmonics of this cycle, as indicated by the occurrence of diagonal lines with 20 kyr, 10 kyr, and 5 kyr spacing (Figs. 2 and 3). In addition to these cyclical wet-dry fluctuations in the area, extreme events often occur, i.e. short wet or dry episodes, lasting for several centuries or even millennia, and rapid transitions between wet and dry episodes. This type of variability probably reflects the influence of precessional forcing in the lower latitudes at times of increased eccentricity, with a tendency towards extreme events. This also shows in comparatively low RR and DET values, suggesting a lower predictability of climate variations for this type of variability. This type of variability correlates with maximum values of the long (400 kyr) eccentricity cycle, and hence maximum variability in the precession frequency band. There is no systematic correlation with atmospheric CO_2 concentration.

The second type of variability, occurring at 410–348 kyr BP, 272–252 kyr BP, and 59–11 kyr BP, is characterized by relatively low variation on orbital time scales. Instead, we observe significant century-millennium-scale variations with increasing frequency in the course of an episode with Type 2 variability, as the curved diagonal lines in RP suggest (Figs. 2 and 3). The very prominent cycles in the frequency band lead to very high DET and partly high RR values, which indicate a high predictability of climate change, much higher than at times of Type 1. Within this type of variability there are extremely fast transitions between dry and wet within a few decades or years, in contrast to those within Type 1 with transitions that last several hundreds of years. Type 2 variability seems to be linked with minimum values of the long (400 kyr) eccentricity cycle, and again there does not seem to be a link with atmospheric CO_2 levels. The first episode with Type 2 variability occurs in an interval with maximum eccentricity in the 100 kyr frequency band when the atmospheric CO_2 was quite high. The other two episodes occur during minimal eccentricity in this frequency band, with low CO_2 levels at the same time.

The ODP 967 wetness index shows a very similar type of variability, with RR values that highly resemble the variations in the Chew Bahir record, except for the prominent anticorrelation at ~420 and ~150 kyr BP (Fig. 4). The DET values fluctuating in a smaller range (0.95–1.00) compared to those of the Chew Bahir (0.65–0.95), but the temporal variations of DET show obvious similarities at both sites, in particular during the last ~350 kyr. Since the age models of both sites have large uncertainties, it is not possible at this point to judge conclusively whether time shifts in the DET curves are the result of poor age control or actual differences in climate dynamics recorded in the two locations. Comparing the temporal occurrence of the different types of variability in both localities, the ODP 967 wetness index shows a Type 2 variability approximately during the first and third episode of Type 2 variability in the Chew Bahir record, but not during the second episode of Type 2 variability in the Chew Bahir. Instead we find a Type 2 variability between ~245 and 120 kyr BP in the ODP 967 wetness index, all with high DET and RR values. The different types of variability, very obvious in the RPs, but differing slightly in the RQA measures, could also indicate actual differences in dynamics, but also the influence of the spline interpolation on the temporal autocorrelation.

Overall, the K curve shows a clear trend towards a drier and more variable climate, most prominently during the last 200 kyr, which is also reflected in the reducing DET and RR values (Fig. 4). The three episodes with Type 2 variability are about the same length (45–60 kyr) but have (according to the long-term trend) decreasing average humidity levels. The first episode is characterized by a very humid climate, while the two later episodes were rather dry. In particular, the DET values show several stepwise declines over the entire time series, which are not compensated by corresponding increases. The most striking declines are centered at approximately 515 kyr BP, 375 kyr BP, 410 kyr BP, 252 kyr BP and 80 kyr BP. The most dramatic increases in DET are centered at approximately 418 kyr BP, 345 kyr BP, 167 kyr BP and 100 kyr BP. The variability also increased, especially if a few larger fluctuations between 460-410 kyr, at ~335 kyr BP and at ~245 kyr BP are disregarded. In addition, the frequency of rapid transitions from dry to wet and back increases over time. The ODP 967 record shows similar trends on long time scales, whereas there are large differences on shorter time scales, especially in the degree of variability.

The different types of variability and the transitions between these types have important implications for our understanding of the availability of water. Different modes of variability would have transformed eastern Africa's environment considerably, including its vegetation and fauna, and would have shaped the habitat of hominins, inclu-

ding archaic and modern *H. sapiens*, in that part of the continent. The central question, however, is to what extent the different types of fluctuations observed in the environmental record of the Chew Bahir have actually had an impact on living conditions of hominins. Overall, long-term changes (>1 kyrs) would have formed the living environment of hominins on a time-scale that responds to human evolution and corresponds to a time window that is long enough to facilitate large-scale dispersal. The short-term fluctuations (<1 kyrs) may have had dramatic consequences for populations including differential mortality/fertility of *H. sapiens* down to the level of individuals, and thus short-term changes in behavior, including evasive movements to more favorable habitats (e.g. Foerster et al., 2015).

To assess the impact of climate variability on people, it is worth using a well-studied younger analogue of hydro-climatic transformation in eastern Africa. The most recent example of a wet-to-dry transition within Type 1 was the time-progressive termination of the African Humid Period (AHP, 15–5 kyr BP), which lasted several hundred years in most areas (Shanahan et al., 2015; Trauth et al., 2018). At this time, a previously green, then yellow Sahara was largely depopulated, but this happened quite slowly and due to the time-transgressive termination rather in the form of people slowly following favorable living conditions (Kuper and Kröpelin, 2006; Kröpelin et al., 2008; Shanahan et al., 2015). During this gradual transition, climate deterioration could have fostered an important socio-economic transition, including the transition from hunter-gatherer to pastoralism (Garcin et al., 2012; Foerster et al., 2015).

In contrast, the most recent example of a wet-to-dry transition within Type 2 is the onset of pronounced arid conditions during the Younger Dryas chronozone (YD, ~12.8–11.6 kyr BP) that occurred within ~45 yr at Chew Bahir (Trauth et al., 2018). Most importantly, millennial-scale transitions such as the YD happened everywhere at the same time, unlike the orbital-controlled slow changes (Shanahan et al., 2015; Trauth et al., 2018). It is implausible that such relatively rapid transitions triggered a fundamental societal transformation, similar to the one during the termination of the AHP. Instead, climate shifts of this rapidity would allow response patterns that are implementable within (less than) a life-time span, such as short-term migration towards proximal more favorable living conditions. Examples of this are movements from hot dry low-lands into still vegetation-rich high altitudes, or even the complete disappearance of entire local human populations due to scarcity of resources (Foerster et al., 2015, 2016). The possible alternative response to environmental extremes and too fast transformation is extinction/extirpation, because living conditions deteriorated so quickly that neither physical nor cultural adaptation was possible. However, short-term and short-distance mobility depends (a) on a number of socio-cultural conditions (= how flexible, how adaptable are groups, how are they organized?) and (b) mode of climatic change (= pulsed, rapid, parallel with other areas).

CONCLUSIONS

We find two types of variability in the Chew Bahir record, (1) Type 1 probably reflecting the influence of a precessional forcing in the lower latitudes at times of increased eccentricity, with the tendency towards extreme events, and (2) Type 2 with significant century-millennium-scale variations with increasing frequency. Within Type 2 of variability there are extremely fast transitions between dry and wet within a few decades or years that would have exerted a high level of climatic stress on the biosphere including humans, in contrast to those within Type 1 with transitions within several hundreds of years. As the body of archaeological evidence, including fossils and diagnostic tools, continues to increase in the future, it will be exciting to compare potential response patterns to our prosed Type 2 phases of high climatic stress and see whether changes in settlement activities, cultural innovation, or even the emergence or disappearance of populations/occupancy can be correlated with the climatic dimension of the complex framework in human-climate interactions.

ACKNOWLEDGEMENTS

REFERENCES

Amante C, Eakins BW (2009). ETOPO1 1 Arc-Minute Global Relief Model: Procedures, Data Sources and Analysis. NOAA Technical Memorandum NESDIS NGDC-24.

Ambrose, S.H. (1998). Late Pleistocene human population bottlenecks, volcanic winter, and the differentiation of modern humans, Journal of Human Evolution 35, 115–118.

Bereiter, B., Eggleston, S., Schmitt, J., Nehrbass-Ahles, C., Stocker, T.F., Fischer, H., Kipfstuhl, S., Chappellaz, J. (2015). Revision of the EPICA Dome C CO_2 record from 800 to 600 kyr before present. Geophysical Research Letters. . doi: 10.1002/2014GL061957

Bonnefille, R. (2010) Cenozoic vegetation, climate changes and hominid evolution in tropical Africa. Global and Planetary Change, 72, 390-411.

Brandt, S.A. and E.A. Hildebrand (2005). Southwest Ethiopia as an Upper Pleistocene Refugium. Paper presented at the Workshop on the Middle Stone Age of Eastern Africa. Nairobi, Kenya and Addis Ababa, Ethiopia, July 2005.

Brovkin, V., Claussen, M., (2008). Comment on "Climate-Driven Ecosystem Succession in the Sahara: The Past 6000 Yr". Science, 322, 1326b-c.

Campisano CJ, Cohen AS, Arrowsmith JR, Asrat A, Behrensmeyer AK, Brown ET, Deino AL, Deocampo DM, Feibel CS, Kingston JD, Lamb HF, Lowenstein TK, Noren A, Olago DO, Owen RB, Pelletier JD, Potts R, Reed KE, Renaut RW, Russell JM, Russell JL, Schäbitz F, Stone JR, Trauth MH, Wynn JG (2017). The Hominin Sites and Paleolakes Drilling Project: high-resolution paleoclimate records from the East African Rift System and their implications for understanding the environmental context of hominin evolution. PaleoAnthropology 2017:1-43. https://doi.org/10.4207/PA.2017.ART104

Cane, M.A., Molnar, P. (2001). Closing of the Indonesian seaway as a precursor to east African aridification around 3–4 million years ago. Nature, 411, 157-162.

Cohen A, Campisano C, Arrowsmith R, Asrat A, Behrensmeyer AK, Deino A, Feibel C, Hill A, Johnson R, Kingson J, Lamb H, Lowenstein T, Noren A, Olago D, Owen RB, Potts R, Reed K, Renaut R, Schäbitz F, Tiercelin JJ, Trauth MH, Wynn J, Ivory S, Brady K, O'Grady R, Rodysill J, Githiri J, Russell J, Foerster V, Dommain R, Rucina S, Deocampo D, Russell J, Billingsley A, Beck C, Dorenbeck G, Dullo L, Feary D, Garello D, Gromig R, Johnson T, Junginger A, Karanja M, Kimburi E, Mbuthia A, McCartney T, McNulty E, Muiruri V, Nambiro E, Negash EW, Njagi D, Wilson JN, Rabideaux N, Raub T, Sier MJ, Smith P, Urban J, Warren M, Yadeta M, Yost C, Zinaye B (2016). The Hominin Sites and Paleolakes Drilling Project: Inferring the Environmental Context of Human Evolution from Eastern African Rift Lake Deposits. Scientific Drilling 21:1-16. https://doi.org/10.5194/sd-21-1-2016.

Clarke, J., Brooks, N., Banning, E.B., Bar-Matthews, M., Campbell, S., Clare, L., Cremaschi, M., di Lernia, S., Drake, N., Gallinaro, M., Manning, S., Nicoll, K., Philip, G., Rosen, S., Schoop, U.D., Tafuri, M.A., Weninger, B., Zerboni, A. (2016). Climatic changes and social transformations in the Near East and North Africa during the 'long' 4th millennium BC: A comparative study of environmental and archaeological evidence. Quaternary Science Reviews, 136, 96–121. https://doi.org/10.1016/j.quascirev.2015.10.003.

Davidson A (1983). The Omo River project: reconnaissance geology and geochemistry of parts of Ilubabor, Kefa, Gemu Gofa and Sidamo. Ethiopian Institute of Geological Surveys Bulletin 2:1-89.

deMenocal, P. (1995). Plio-Pleistocene African Climate. Science 270, 53-59.

deMenocal P, Ortiz J, Guilderson T, Adkins J, Sarnthein M, Baker L, Yarusinsky M (2000). Abrupt onset and termination of the African

Humid Period: rapid climate responses to gradual insolation forcing. *Quaternary Science Reviews* 19:347-361. https://doi.org/10.1016/S0277-3791(99)00081-5

deMenocal, P.B. (2004). *African climate change and faunal evolution during the Pliocene-Pleistocene. Earth and Planetary Science Letters* 220, 3-24.

Ditlevsen PD, Johnsen SJ (2010). *Tipping points: Early warning and wishful thinking. Geophysical Research Letters* 37:L19703. https://doi.org/10.1029/2010GL044486

Eckmann JP, Kamphorst SO, Ruelle D (1987). *Recurrence Plots of Dynamical Systems. Europhysics Letters,* 5, 973-977. https://doi.org/10.1209/0295-5075/4/9/004

Flohr, P., Fleitmann, D., Matthews, R., Matthews W., Black, S. 2016. *Evidence of resilience to past climate change in Southwest Asia: Early farming communities and the 9.2 and 8.2 ka events. Quaternary Science Reviews,* 136, 23–39. https://doi.org/10.1016/j.quascirev.2015.06.022.

Foerster V, Junginger A, Langkamp O, Gebru T, Asrat A, Umer M, Lamb H, Wennrich V, Rethemeyer J, Nowaczyk N, Trauth MH, Schäbitz F (2012). *Climatic change recorded in the sediments of the Chew Bahir basin, southern Ethiopia, during the last 45,000 yr. Quaternary International* 274:25-37. https://doi.org/10.1016/j.quaint.2012.06.028

Foerster V, Vogelsang R, Junginger A, Asrat A, Lamb HF, Schaebitz F, Trauth MH (2015). *Environmental Change and Human Occupation of Southern Ethiopia and Northern Kenya during the last 20,000 yr. Quaternary Science Reviews* 129:333-340. https://doi.org/10.1016/j.quascirev.2015.10.026

Foerster V, Deocampo DM, Asrat A, Günter C, Junginger A, Kraemer H, Stroncik NA, Trauth MH (2018). *Towards an understanding of climate proxy formation in the Chew Bahir basin, southern Ethiopian Rift. Palaeogeography, Palaeoclimatology, Palaeoecology* 501:111-123. https://doi.org/10.1016/j.palaeo.2018.04.009

Foerster et al. (submitted) *650 Thousand Years of Climate Change from Chew Bahir, S Ethiopia, and human evolution, migration and innovation. Nature, submitted.*

Fritsch, F.N., Carlson, R.E. (1980). *Monotone Piecewise Cubic Interpolation. SIAM Journal on Numerical Analysis,* 17, 238–246. Galway-Witham, J., Cole, J., Stringer, C. (2019) *Aspects of human physical and behavioural evolution during the last 1 million years. Journal of Quaternary Science,* 34, 355–378. https://doi.org/10.1002/jqs.3137.

Garcin, Y., Melnick, D., Strecker, M.R., Olago, D., Tiercelin, J.-J. (2012). *East African mid-Holocene wet–dry transition recorded in palaeo-shorelines of Lake Turkana, northern Kenya Rift. Earth and Planetary Science Letters,* 331-332, 322–334.

Gatto, M.C., Zerboni, A. (2015). *Holocene Supra-Regional Environmental Changes as Trigger for Major Socio-Cultural Processes in Northeastern Africa and the Sahara. African Archaeological Review,* 32, 301–333. https://doi.org/10.1007/s10437-015-9191-x.

Grant, K.M., Rohling, E.J., Westerhold, H., Zabel, M., Heslop, D., Konijnendijk, T., Lourens, L. (2017). *A 3 million year index for North African humidity/aridity and the implication of potential pan-African Humid periods. Quaternary Science Reviews,* 171, 100–118, doi: 10.1016/j.quascirev.2017.07.005.

Hays, J.D., Imbrie, J., Shackleton, N.J. (1976). *Variations in the Earth's orbit: pacemaker of the ice ages. Science,* 194, 1121-1132, doi: 10.1126/science.194.4270.1121.

Iwanski J, Bradley E (1998). Recurrence plot analysis: To embed or not to embed? Chaos 8:861-871. https://doi.org/10.1063/1.166372.

Junginger, A., Trauth, M.H. (2013). Hydrological constraints of paleo-Lake Suguta in the Northern Kenya Rift during the African Humid Period (15 - 5 ka BP). Global and Planetary Change, 111, 174–188.

Kröpelin, S., Verschuren, D., Lézine, A.-M., Eggermont, H., Cocquyt, C., Francus,P., Cazet, J.-P., Fagot, M., Rumes, B., Russell, J.M., Darius, F., Conley, D.J., Schuster, M., von Suchodoletz, H., Engstrom, D.R. (2008a). Climate-Driven Ecosystem Succession in the Sahara: The Past 6000 Yr. Science 320, 765-768.

Kröpelin, S., Verschuren, D., Lézine, A.-M. (2008b). Response to Comment by Brovkin and Claussen on "Climate-Driven Ecosystem Succession in the Sahara: The Past 6000 Yr". Science, 322, 1326.

Kuper, R., Kröpelin, S. (2006). Climate-Controlled Holocene Occupation in the Sahara: Motor of Africa's Evolution. Science, 313, 803-307.

Lahr, M. (2016). The shaping of human diversity: filters, boundaries and transitions. Philosophical Transactions of the Royal Society B, 371: 20150241. https://10.1098/rstb.2015.0241.

Laskar, J., Gastineau, M., Joutel, F., Robutel, P., Levrard, B., Correia, A. (2004). A long term numerical solution for the insolation quantities of Earth. Astronomy and Astrophysics, 428, 261–285.

Lenton TM, Held H, Kriegler E, Hall JW, Lucht W, Rahmstorf S, Schellnhuber HJ (2008). Tipping elements in the Earth's climate system. Proceedings of the National Academy of Sciences 105:1786-1796. https://doi.org/10.1073/pnas.0705414105

Marwan N, Romano MC, Thiel M, Kurths J (2007). Recurrence Plots for the Analysis of Complex Systems. Physics Reports 438:237-329. https://doi.org/10.1016/j.physrep.2006.11.001

Marwan N (2008). A Historical Review of Recurrence Plots. European Physical Journal, Special Topics 164:3-12. https://doi.org/10.1140/epjst/e2008-00829-1

Marwan N (2011). How to avoid potential pitfalls in recurrence plot based data analysis. Journal of Biofurcation and Chaos 21:1003-1017. https://doi.org/10.1142/S0218127411029008

Maslin, M.A., Trauth, M.H. (2009). Plio-Pleistocene Eastern African Pulsed Climate Variability and its influence on early human evolution. In: Grine, F.E., Leakey, R.E., Fleagle, J.G. (Eds.), The First Humans–Origins of the Genus Homo. Springer Verlag, Vertebrate Paleobiology and Paleoanthropology Series, pp. 151-158.

McDougall, I., Brown, F.H., Fleagle, J.G. (2005). Stratigraphic placement and age of modern humans from Kibish, Ethiopia. Nature 433, 733–736.

Moore JM, Davidson A (1978). Rift structure in southern Ethiopia. Tectonophysics 46:159-173. https://doi.org/10.1016/0040-1951(78)90111-7.

Nicholson SE (2017). Climate and climatic variability of rainfall over eastern Africa. Reviews of Geophysics 55:590-635. https://doi.org/10.1002/2016RG000544.

Ossendorf et al. (2019). Middle Stone Age foragers resided in high elevations of the glaciated Bale Mountains, Ethiopia. Science 365, 583–587. https://doi.org/10.1126/science.aaw8942.

Packard NH, Crutchfield JP, Farmer JD, Shaw RS (1980). Geometry from a time series. Physical Review Letters 45:712-716. https://doi.org/10.1103/PhysRevLett.45.712

Potts, R. (1996). Evolution and Climate Variability. Science, 273, 922-923.

Potts, R. (2013). Hominin evolution in settings of strong environmental variability. Quaternary Science Reviews, 73, 1-13. https://doi.org/10.1016/j.quascirev.2013.04.003.

Scerri, E.M.L., et al. (2018). Did Our Species Evolve in Subdivided Populations across Africa, and Why Does It Matter? Trends in Ecology & Evolution, 33, 592–594, 10.1016/j.tree.2018.05.005.

Stringer, C., Galway-Witham, J. (2017) .On the origin of our species. Nature, 546, 212–214. https://doi.org/10.1038/546212a.

Takens F (1981). Detecting strange attractors in turbulence. Lecture Notes in Mathematics 898, Springer, Berlin Heidelberg New York, pp. 366-381. https://doi.org/10.1007/BFb0091924

Roberts et al. (submitted). Using multiple chronometers to establish a long, directly-dated lacustrine record: constraining >600,000 years of environmental change at Chew Bahir, Ethiopia. QSR, submitted

Shanahan, T.M., McKay, N.P., Hughen, K.A., Overpeck, J.T., Otto-Bliesner, B., Heil, C.W., King, J., Scholz, C.A., Peck, J. (2015). The time-transgressive termination of the African Humid Period. Nature Geoscience, 8, 140-144.

Schäbitz et al. (submitted). Two modes of humidity fluctuations in the last 200 kyr of the Chew Bahir record: their meaning for migration, vertical mobility and dispersal pathways of Homo sapiens. Geology, submitted.

Stringer, C., Galway-Witham, J. (2017). On the origin of our species. Nature, 546, 212–213, doi:10.1038/546212a.

Takens F (1981). Detecting strange attractors in turbulence. Lecture Notes in Mathematics 898, Springer, Berlin Heidelberg New York, pp. 366-381. https://doi.org/10.1007/BFb0091924

Tierney JE, deMenocal PB (2013). Abrupt shifts in Horn of Africa hydroclimate since the last glacial maximum. Science 342:843-846. https://doi.org/10.1126/science.1240411

Trauth, M.H., Maslin, M.A., Deino, A., Strecker, M.R. (2005). Late Cenozoic Moisture History of Eastern Africa. Science, 309, 2051-2053.

Trauth, M.H., Larrasoaña, J.C., Mudelsee, M. (2009). Trends, rhythms and events in Plio-Pleistocene African climate. Quaternary Science Reviews, 28, 399-411.

Trauth, M.H., Maslin, M.A., Deino, A., Junginger, A., Lesoloyia, M., Odada, E., Olago, D.O., Olaka, L., Strecker, M.R., Tiedemann, R. (2010). Human Evolution in a Variable Environment: The Amplifier Lakes of East Africa. Quaternary Science Reviews, 29. 2981-2988.

Trauth MH, Bergner AGN, Foerster V, Junginger A, Maslin MA, Schaebitz F (2015). Episodes of environmental stability and instability in late Cenozoic lake records of Eastern Africa. Journal of Human Evolution 87:21-31. https://doi.org/10.1016/j.jhevol.2015.03.011

Trauth MH, Foerster V, Junginger A, Asrat A, Lamb HF, Schaebitz F (2018). Abrupt or gradual? Change point analysis of the late Pleistocene-Holocene climate record from Chew Bahir, southern Ethiopia. Quaternary Research 90:321-330. https://doi.org/10.1017/qua.2018.30

Trauth, M.H., Asrat, A., Duesing, W., Foerster, V., Kraemer, K.H., Marwan, N., Maslin, M.A., Schaebitz, F. (2019). *Classifying past climate change in the Chew Bahir basin, southern Ethiopia, using recurrence quantification analysis. Climate Dynamics, available online, https://doi.org/10.1007/s00382-019-04641-3.*

Viste, E., Sorteberg, A. (2013). *The effect of moisture transport variability on Ethiopian summer precipitation. International Journal of Climatology, 33, 3107-312. https://doi.org/10.1002/joc.3566.*

Vogelsang, R., Bubenzer, O., Kehl, M., Meyer, S., Richter, J., Zinaya, B. (2018) *When Hominins Conquered Highlands—an Acheulean Site at 3000 m a.s.l. on Mount Dendi/Ethiopia. Journal of Paleolithic Archaeology 1, 302–313. https://doi.org/10.1007/s41982-018-0015-9.*

Vrba, E.S. (1985). *Environment and evolution: Alternative causes of the temporal distribution of evolutionary events. South African Journal of Sciences 81, 229–236.*

Vrba, E.S., (1993). *The pulse that produced us: two major global coolings may have prodded antelopes and humans to evolve : How did humans get that way? Natural History 102 (5), 47-51.*

Webber CL, Zbilut JP (2005). *Recurrence Quantification Analysis of Nonlinear Dynamical Systems, in: from: Riley, M.A, Van Orden, G.C, Tutorials in contemporary nonlinear methods for the behavioral sciences, https://doi.org/10.1007/978-3-319-07155-8*

Wessel P, Smith WHF (1996). *A Global Self-consistent, Hierarchical, High-resolution Shoreline Database. Journal of Geophysical Research 101 B4: 8741-8743.*

Zbilut JP, Webber Jr CL (1992). *Embeddings and delays as derived from quantification of recurrence plots. Physics Letters A 171:199-203. https://doi.org/10.1016/0375-9601(92)90426-M*
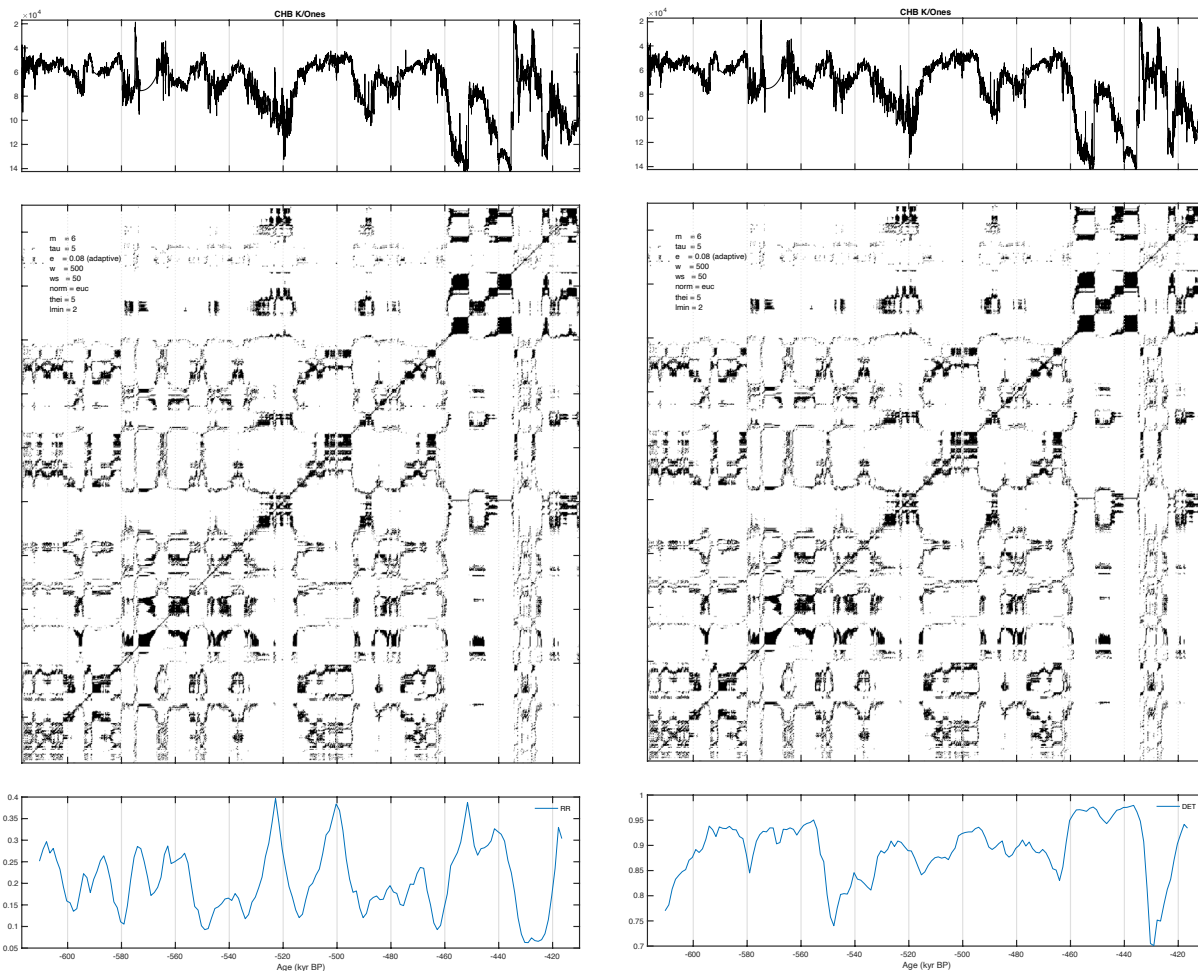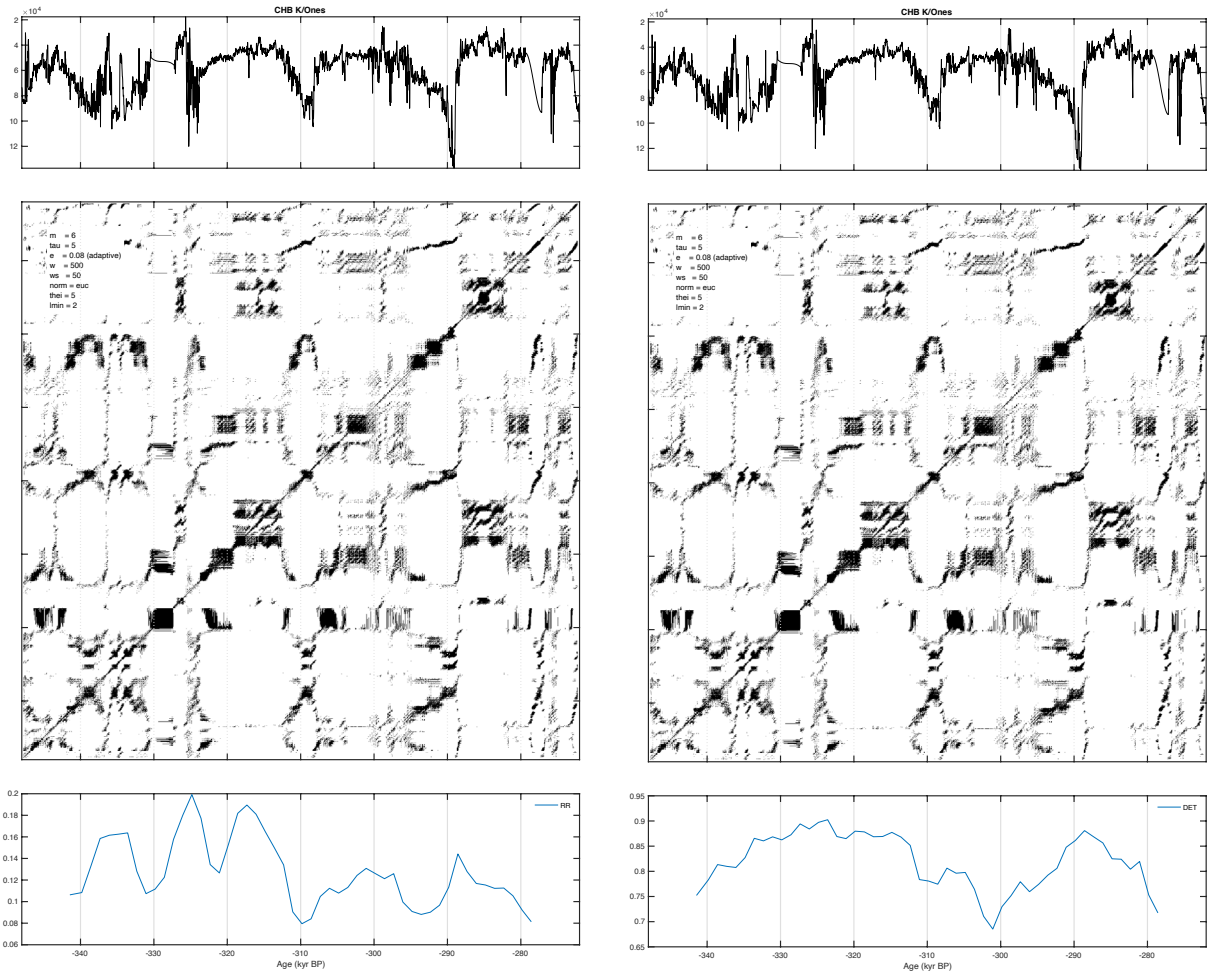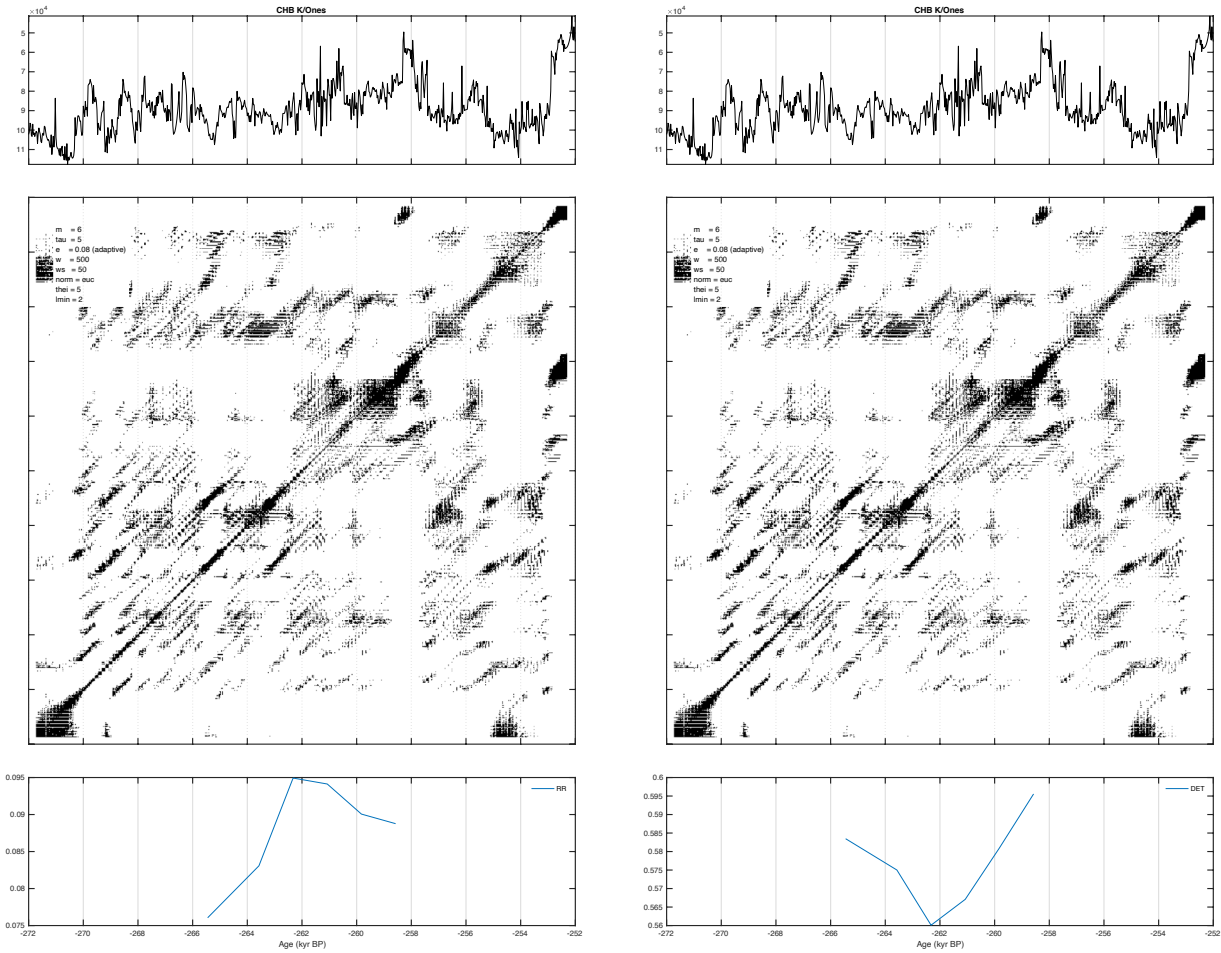
Supplementary Figure 1
Recurrence plot (RP) and recurrence quantification analysis (RQA) measures of the high resolution (0.015 kyr) potassium (K) concentrations of the sediment in Chew Bahir in southern Ethiopia between 620 and 410 kyr BP: the time series according to age model (3) (upper panel), the recurrence plot (middle panel) and the RQA measures (a) RR and (b) DET of moving windows (lower panel). Embedding parameters m=embedding dimension, tau=time delay, e=threshold, w=window size, ws=window moving steps, norm=vector norm, thei=size of Theiler window, lmin=minimum line length, RQA measures RR=recurrence rate and DET=determinism. See the methods section for a detailed description of the embedding parameters and RQA measures.
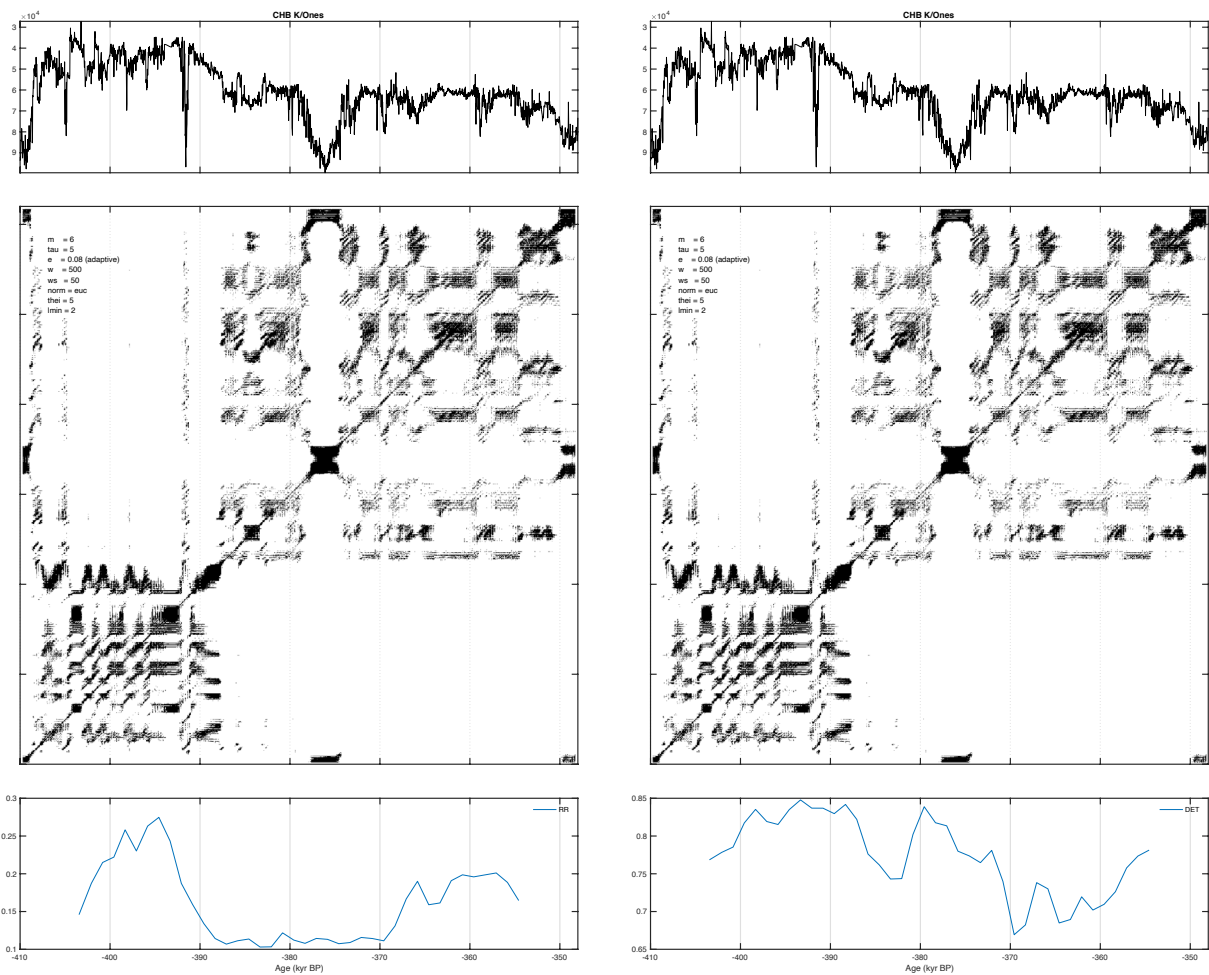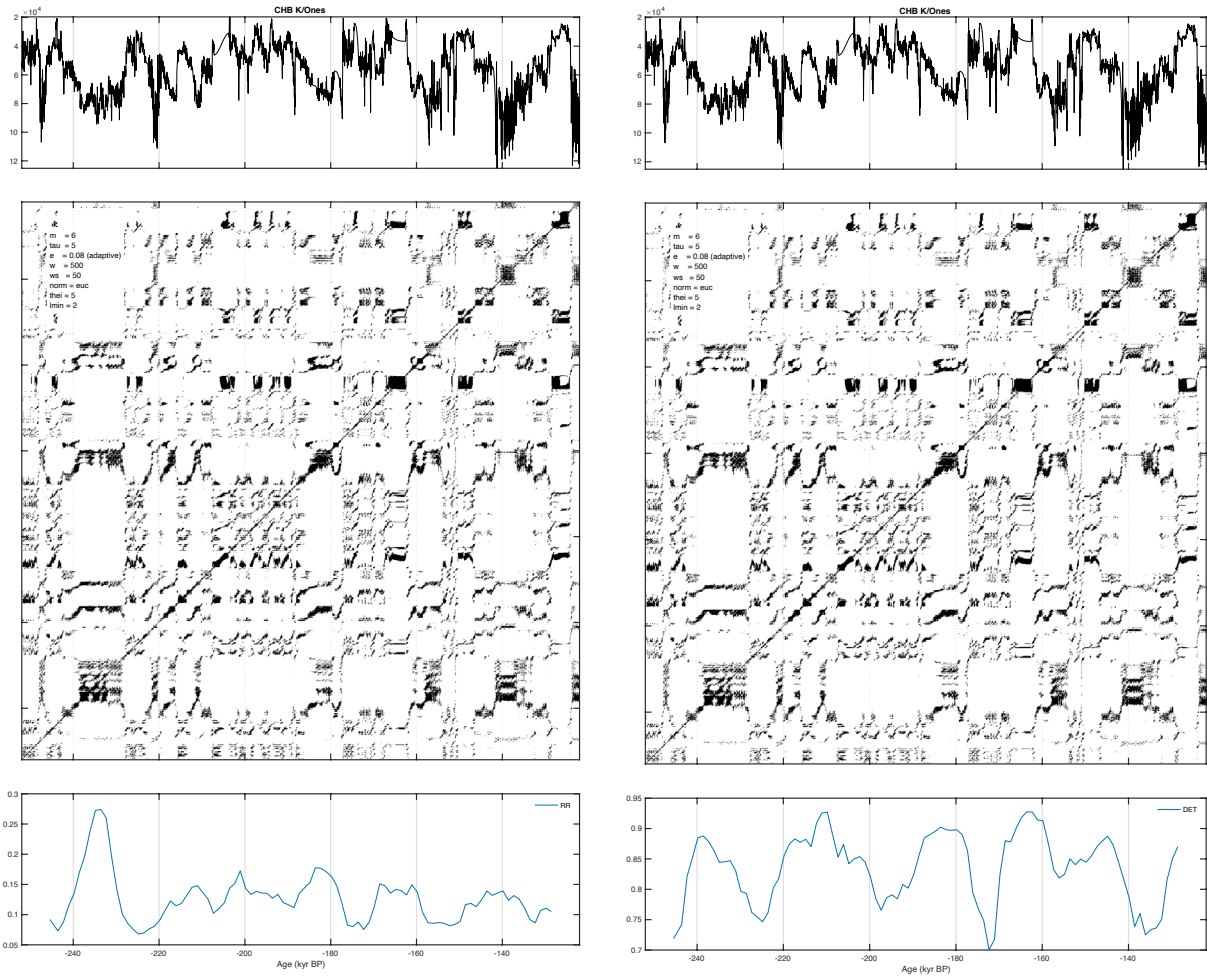
Supplementary Figure 2
Recurrence plot (RP) and recurrence quantification analysis (RQA) measures of the high resolution (0.015 kyr) potassium (K) concentrations of the sediment in Chew Bahir in southern Ethiopia between 410 and 348 kyr BP: the time series according to age model (3) (upper panel), the recurrence plot (middle panel) and the RQA measures (a) RR and (b) DET of moving windows (lower panel). For abbreviations, see caption of Supplementary Figure 1. See the methods section for a detailed description of the embedding parameters and RQA measures.
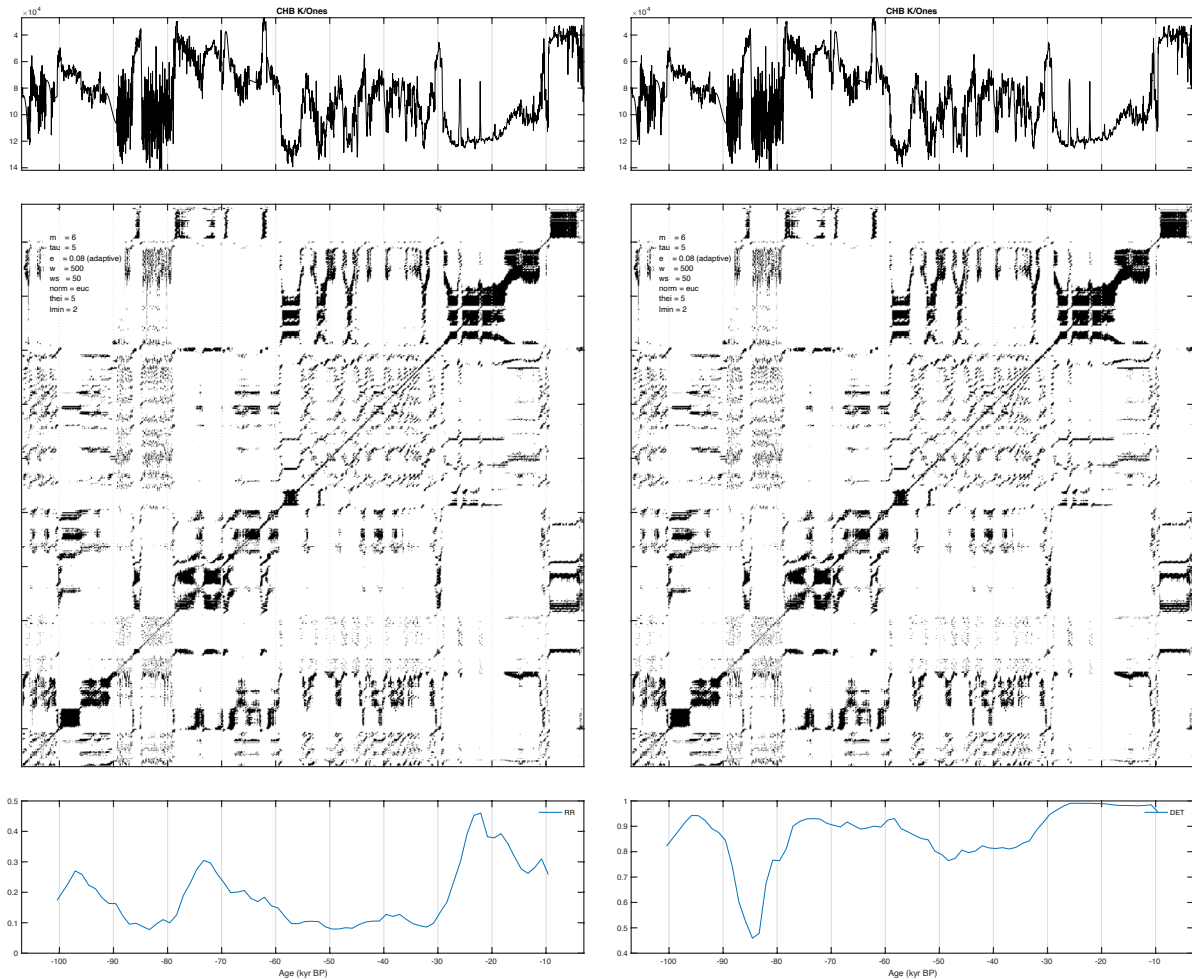
Supplementary Figure 3
Recurrence plot (RP) and recurrence quantification analysis (RQA) measures of the high resolution (0.015 kyr) potassium (K) concentrations of the sediment in Chew Bahir in southern Ethiopia between 348 and 272 kyr BP: the time series according to age model (3) (upper panel), the recurrence plot (middle panel) and the RQA measures (a) RR and (b) DET of moving windows (lower panel). For abbreviations, see caption of Supplementary Figure 1. See the methods section for a detailed description of the embedding parameters and RQA measures.

Supplementary Figure 4
Recurrence plot (RP) and recurrence quantification analysis (RQA) measures of the high resolution (0.015 kyr) potassium (K) concentrations of the sediment in Chew Bahir in southern Ethiopia between 272 and 252 kyr BP: the time series according to age model (3) (upper panel), the recurrence plot (middle panel) and the RQA measures (a) RR and (b) DET of moving windows (lower panel). For abbreviations, see caption of Supplementary Figure 1. See the methods section for a detailed description of the embedding parameters and RQA measures.

Supplementary Figure 5
Recurrence plot (RP) and recurrence quantification analysis (RQA) measures of the high resolution (0.015 kyr) potassium (K) concentrations of the sediment in Chew Bahir in southern Ethiopia between 252 and 122 kyr BP: the time series according to age model (3) (upper panel), the recurrence plot (middle panel) and the RQA measures (a) RR and (b) DET of moving windows (lower panel). For abbreviations, see caption of Supplementary Figure 1. See the methods section for a detailed description of the embedding parameters and RQA measures.

Supplementary Figure 6
Recurrence plot (RP) and recurrence quantification analysis (RQA) measures of the high resolution (0.015 kyr) potassium (K) concentrations of the sediment in Chew Bahir in southern Ethiopia between 107 and 3 kyr BP: the time series according to age model (3) (upper panel), the recurrence plot (middle panel) and the RQA measures (a) RR and (b) DET of moving windows (lower panel). For abbreviations, see caption of Supplementary Figure 1. See the methods section for a detailed description of the embedding parameters and RQA measures.

Acknowledgement